JOURNAL OF PETROLOGY | VOLUME 53 | NUMBER 1 | PAGES 177–233 | 2012 | doi:10.1093/petrology/egr061

Temperature, Pressure, and Composition of the Mantle Source Region of Late Cenozoic Basalts in Hainan Island, SE Asia: a Consequence of a Young Thermal Mantle Plume close to Subduction Zones?

XUAN-CE WANG[1,2,3]*, ZHENG-XIANG LI[1], XIAN-HUA LI[2], JIE LI[4], YING LIU[4], WEN-GUO LONG[5], JIN-BO ZHOU[5] AND FEI WANG[2]

[1]THE INSTITUTE FOR GEOSCIENCE RESEARCH (TIGER) AND ARC CENTRE OF EXCELLENCE FOR CORE TO CRUST FLUID SYSTEMS (CCFS), DEPARTMENT OF APPLIED GEOLOGY, CURTIN UNIVERSITY, GPO BOX U1987, PERTH, WA 6845, AUSTRALIA

[2]STATE KEY LABORATORY OF LITHOSPHERIC EVOLUTION, INSTITUTE OF GEOLOGY AND GEOPHYSICS, CHINESE ACADEMY OF SCIENCES, PO BOX 9825, BEIJING 100029, CHINA

[3]SCHOOL OF EARTH AND ENVIRONMENT, THE UNIVERSITY OF WESTERN AUSTRALIA, CRAWLEY, WA 6009, AUSTRALIA

[4]STATE KEY LABORATORY OF ISOTOPE GEOCHEMISTRY, GUANGZHOU INSTITUTE OF GEOCHEMISTRY, CHINESE ACADEMY OF SCIENCES, GUANGZHOU 510640, CHINA

[5]HAINAN INSTITUTE OF GEOLOGICAL SURVEY, HAIKOU 570226, CHINA

RECEIVED DECEMBER 1, 2010; ACCEPTED NOVEMBER 1, 2011
ADVANCE ACCESS PUBLICATION DECEMBER 13, 2011

Basaltic lavas from Hainan Island near the northern edge of the South China Sea have an age range of between late Miocene (about 13 Ma) and Holocene, with a peak age of late Pliocene to middle Pleistocene. The basaltic province is dominated by tholeiites with subordinate alkali basalts. Most analysed samples display light rare earth element (LREE) enriched REE patterns and ocean island basalt (OIB)-like incompatible element distributions. The basalts contain abundant undeformed high-Mg olivine phenocrysts (up to $Fo_{90\cdot7}$) that are high in CaO and MnO, indicating high-magnesian parental magmas. Independent barometers indicate that clinopyroxenes in the basalts crystallized over a wide range of pressures of 2–25 kbar (dominantly at 10–15 kbar) and that the melt cooled from about 1350°C to 1100°C during their crystallization. The compositional characteristics of the basalts indicate that their generation most probably involved both low-silica and high-silica melts, as represented by the alkali basalts and tholeiites, respectively. Our results show that the source region for the Hainan basalts is highly heterogeneous. The source for the tholeiites is mainly composed of peridotite and recycled oceanic crust, whereas the source for the bulk of the low-Th alkali basalts consists predominantly of peridotite and low-silica eclogite (garnet pyroxenite). Some high-Th ($\geq$ 4 ppm) alkali basalts may have been produced by partial melting of low-silica garnet pyroxenite (eclogite). We estimated the primary melt compositions for the Hainan basalts using the most forsteritic olivine ($Fo_{90\cdot7}$) composition and the most primitive bulk-rock samples ($MgO > 9\cdot0$ wt % and $CaO > 8\cdot0$ wt %), assuming a constant Fe–Mg exchange partition coefficient of $K_D = 0\cdot31$ and $Fe^{3+}/Fe^{T} = 0\cdot1$. The effective melting pressure (P_f) and melting temperature (T) of the primary melts are $P_f = 18$–32 kbar (weighted average $= 23\cdot8 \pm 1\cdot8$ kbar) and T = 1420–1520°C for

*Corresponding author. Present address: Department of Applied Geology, Curtin University, GPO Box U1987, Perth, WA 6845, Australia. Telephone: +61 8 9266 2453. Fax: +61 8 9266 3153. E-mail: X.Wang3@curtin.edu.au

the tholeiites, and $P_f = 25$–32 (weighted average $= 28{\cdot}3 \pm 1{\cdot}4$ kbar) and $T = 1480$–$1530^\circ C$ for the alkali basalts. The P_f–T data form an array that plots systematically above the dry lherzolite solidus but below the base of the lithosphere (~55 km) and intersects the dry peridotite solidus at a pressure of about 50 kbar. The mantle potential temperature beneath Hainan Island, based on the estimate primary melt compositions, varies from about 1500 to 1580°C with a weighted average of $1541 \pm 10^\circ C$. The high-magnesian olivine phenocrysts, high mantle potential temperature, and the presence of recycled oceanic crust in the source region provide independent support for the Hainan plume model that has previously been proposed largely based on geophysical observations. The Hainan plume thus provides a rare example of a young mantle plume associated with deep slab subduction.

KEY WORDS: *Hainan Island; South China Sea; basalts; plume; Cenozoic; geochemistry*

INTRODUCTION

Southeast Asia (including southeastern China, the South China Sea, and the Indochina Block) has one of the most cryptic tectonic settings (Taylor & Hayes, 1980; Chung *et al.*, 1997; Yin & Harrison, 2000; Sun *et al.*, 2009; Fig. 1a). Extensive and voluminous late Cenozoic basalts are a prominent feature in this region (e.g. Zhu & Wang, 1989; Flower *et al.*, 1992; Zhou & Mukasa, 1997; Hoang & Flower, 1998; Ho *et al.*, 2000; Fedorov & Koloskov, 2005; Zou & Fan, 2010). These basalts are widespread inside the South China Sea Basin (e.g. Yan *et al.*, 2008), in Hainan Island–Leizhou Peninsula (e.g. Tu *et al.*, 1991; Flower *et al.*, 1992; Ho *et al.*, 2000; Zou & Fan, 2010), and in the Indochina Peninsula (e.g. Zhou & Mukasa, 1997; Hoang & Flower, 1998). These basalts comprise an oceanic island basalt (OIB)-like suite dominated by quartz and olivine tholeiites with subsidiary alkali basalts (e.g. Flower *et al.*, 1992; Hoang & Flower, 1998; Ho *et al.*, 2000). The basalts are younger than the South China Sea sea-floor extension (between *c.* 30 and 16 Ma; Sun *et al.*, 2009, and references therein) and have a peak age <9 Ma (e.g. Hoang & Flower, 1998; Ho *et al.*, 2000, 2003; Fan *et al.*, 2004; Yan *et al.*, 2008). They are characterized by OIB-type incompatible element distributions, an intriguing Dupal-like Pb isotopic signature, and depleted Sr–Nd isotopic compositions (e.g. Tu *et al.*, 1991; Flower *et al.*, 1992; Hoang & Flower, 1998; Yan *et al.*, 2008). Such a widespread intraplate basaltic magmatism has variously been attributed to lithosphere extension (e.g. Zhu & Wang, 1989; Tu *et al.*, 1991; Flower *et al.*, 1992), mantle escape from under Asia in response to lithospheric thickening in the Indo-Eurasian collision zone (e.g. Hoang & Flower, 1998), and mantle plumes or hotspots (e.g. Yan *et al.*, 2008; Lei *et al.*, 2009; Zou & Fan, 2010).

Up to now, the most compelling evidence for the plume or hotspot model comes from seismic tomography that defines a plume-like mantle low-velocity structure beneath the north Hainan Island–Leizhou Peninsula basalt province (e.g. Lebedev & Nolet, 2003; Montelli *et al.*, 2004, 2006; Zhao, 2004, 2007; Huang & Zhao, 2006; Lei *et al.*, 2009). High-resolution tomographic images of the upper mantle show a clear geometry of a SE-plunging, low-velocity column with a diameter of about 80 km continuous from the surface down to about 250 km (Lei *et al.*, 2009). On a global scale, the hypothesized Hainan plume extends down to about 1900 km depth (e.g. Ritsema *et al.*, 1999; Montelli *et al.*, 2006) or to the lowermost mantle (e.g. Zhao, 2004, 2007; Lei & Zhao, 2006).

The hypothesized Hainan plume is provocative because so far plumes, with the exception of the Yellowstone plume in western North America, that appear to have existed in the past 150 Myr are located above either the Pacific superplume or the African superplume, where broad low-velocity zones of >6000 km in dimension exist in the lower mantle (e.g. Ritsema *et al.*, 1999; Friederich, 2003; Thorne *et al.*, 2004; Zhao, 2004; Montelli *et al.*, 2006; Schmerr *et al.*, 2010). However, like the Yellowstone plume, the proposed Hainan plume is located at the fringe of the Asian downwelling zone away from both Pacific and African superplumes, making it more intriguing as to whether it is a mantle plume and, if it is, why it is there. The current Hainan plume model was developed largely from geophysical observations that are still subject to debate. Questions remain regarding the geological manifestations of such a mantle plume. For instance, what are the petrological–geochemical manifestations of the Hainan plume? What is the thermochemical structure of the plume? Is it indeed hotter than the ambient asthenospheric mantle? Were the Hainan basalts derived from high-temperature primary melts involving recycled components, similar to typical plume-originated oceanic hotspot basalts such as Hawaiian OIB?

In this study, we present a comprehensive set of whole-rock and mineral chemical and $^{40}Ar/^{39}Ar$ geochronological data, with the aim of evaluating the mantle sources, residual phases and mantle thermal state of the Hainan basalts. We estimate the primary melt compositions by combining the most forsteritic olivine phenocryst compositions ($Fo_{90{\cdot}7}$) with whole-rock geochemical data. Mantle potential temperature, melting conditions and T–P for the crystallization of clinopyroxene phenocrysts are estimated, and the geodynamic significance of these findings will be discussed.

GEOLOGICAL BACKGROUND

Hainan Island is located near the southeastern margin of the Eurasian plate, and has been affected by the motions of, and interactions between, the Indian and Philippine

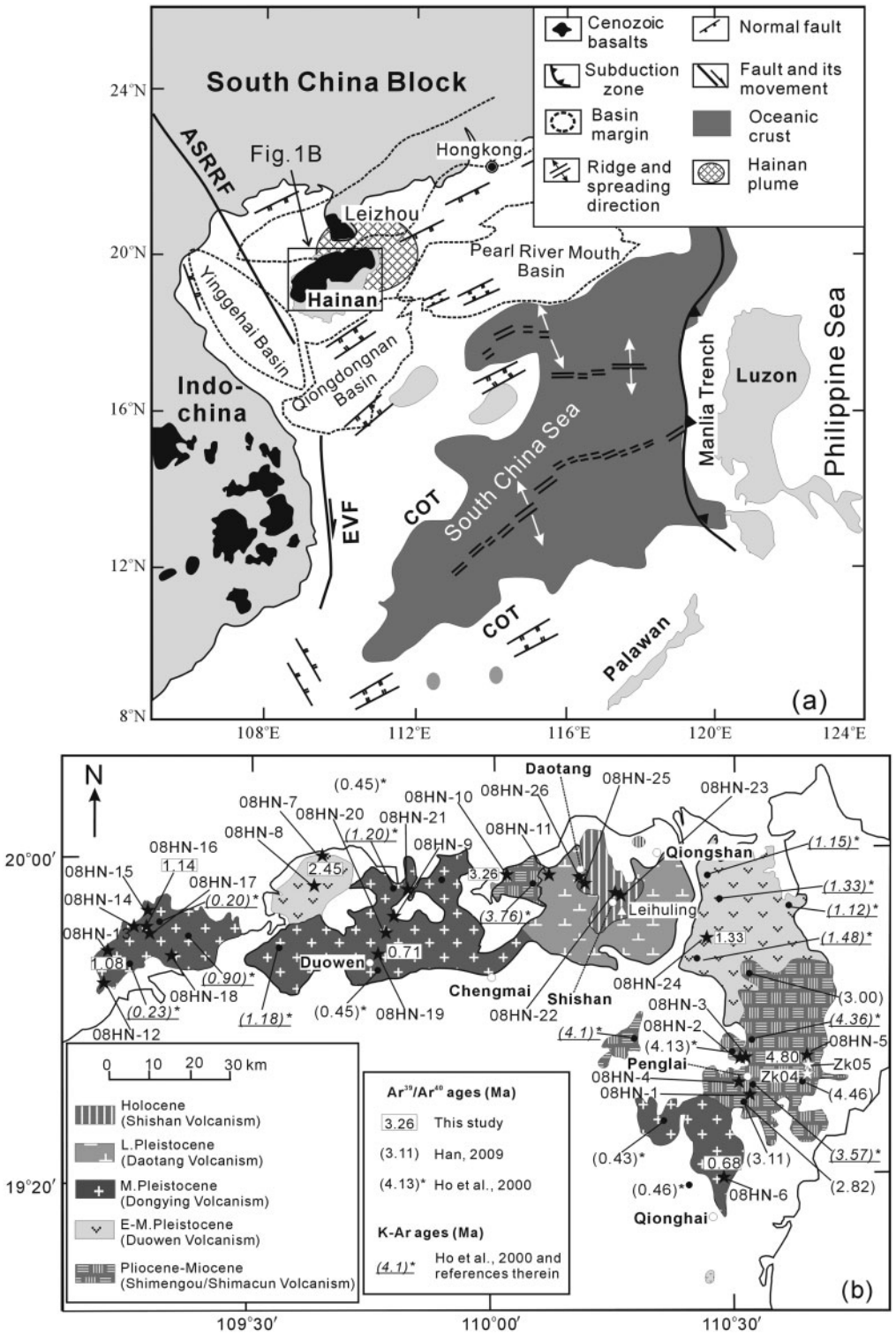

Fig. 1. (a) Simplified geological map of the Indochina Block, Leizhou Peninsula–Hainan Island, South China Sea and surrounding areas showing the distribution of late Cenozoic basaltic volcanism and major continental rift basins (Hoang & Flower, 1998; Ho *et al.*, 2000; Fan *et al.*, 2004; Sun *et al.*, 2009). ASRRF, Ailaoshan–Red River Fault; EVF, Eastern Vietnam Fault; COT, continental–oceanic transition. (b) Index map showing the sampling locations and $^{40}Ar/^{39}Ar$ and K–Ar ages of late Cenozoic basalts from Hainan Island. Distribution and eruptive episodes of basaltic rocks are from Ho *et al.* (2000), Fan *et al.* (2004), Long *et al.* (2006*a*, 2006*b*) and Han (2009).

Sea plates and by the extension of the South China Sea Basin (Fig. 1a). This region records a diverse array of tectonic processes with rifting, subduction, terrane collision and large-scale continental strike-slip faulting occurring in spatially and temporally complex relations (e.g. Cullen *et al.*, 2010).

Late Cenozoic basaltic flows occur in northern Hainan Island and the adjacent Leizhou Peninsula, located at the northern edge of the South China Sea Basin (Fig. 1a). The basaltic plateau in Hainan Island has elevations up to >100 m, with a maximum thickness of ~1000 m and covering a total of ~4160 km^2 (e.g. Flower *et al.*, 1992; Ho *et al.*, 2000; Fan *et al.*, 2004; Long *et al.*, 2006*a*, 2006*b*). Two eruptive styles have been recognized: massive eruptions from extensional fissures, and thinner, more sporadic eruptions from central volcanoes (e.g. Flower *et al.*, 1992; Ho *et al.*, 2000). Fissure eruptive rocks account for the bulk of the sequence and consist almost entirely of quartz- or olivine-normative tholeiite (e.g. Flower *et al.*, 1992). The central volcanoes have produced alkali olivine basalts and basanites, some of which contain spinel-lherzolite and harzburgite mantle xenoliths and megacrysts of clinopyroxene, sapphire (corundum), zircon and anorthoclase. Ho *et al.* (2000) reviewed all published K–Ar and $^{40}Ar/^{39}Ar$ data for the Cenozoic basalts in Hainan Island and the Leizhou Peninsula, and concluded that incipient volcanism took place in late Oligocene times; the intensity of volcanism gradually increased during the Miocene and Pliocene Epochs; volcanism peaked in the Pleistocene and terminated in the Holocene.

Volcanic rocks exposed in northern Hainan Island have been subdivided into five eruptive episodes; these are, from old to young in the order of their eruptive ages (Ho *et al.*, 2000, 2003; Fan *et al.*, 2004; Long *et al.*, 2006*a*, 2006*b*; Fig. 1b): (1) the Pliocene–Miocene episode as represented by the Shimengou and Shimacun volcanism; (2) the early to middle Pleistocene as represented by the Duowen volcanism; (3) the middle Pleistocene episode as represented by the Dongying volcanism; (4) the late Pleistocene episode as represented by the Daotang volcanism; (5) the Holocene episode as represented by the Shishan volcanism. The Duowen volcanism is the largest basaltic outcrop in this region and can be divided into lower and upper sections (e.g. Long *et al.*, 2006*a*, 2006*b*). The lower section lasted from early to middle Pleistocene, and the upper section was formed during the middle Pleistocene (e.g. Long *et al.*, 2006*a*, 2006*b*). It is dominated by quartz and olivine tholeiites with minor volcaniclastic rocks. The late facies of the Duowen volcanism comprise minor alkali olivine basalts. The total thicknesses of the lava sheets vary from 5 to 250 m (Long *et al.*, 2006*b*). The Dongying volcanism is dominated by dispersed quartz and olivine tholeiites, and its thickness varies between 4 and 200 m (Fan *et al.*, 2004). The Daotang volcanism can be divided into lower, middle, and upper sections (Long *et al.*, 2006*a*). The upper and lower sections are dominated by basaltic pyroclastic rocks. The middle section comprises mainly vesicular olivine tholeiites. The Daotang volcanism covers about 600 km^2 with a thickness of up to 330 m (Long *et al.*, 2006*a*). The Shishan volcanism is the youngest volcanic unit in the region (e.g. Huang & Cai, 1994; Ho *et al.*, 2000; Fan *et al.*, 2004). This volcanism is dominated by olivine basalts and olivine tholeiites, and has a total thickness of >95 m. Sandstone xenoliths have been identified in the lavas (e.g. Fan *et al.*, 2004).

PETROGRAPHY

Olivine tholeiites are generally moderately phyric (<15% phenocrysts). The phenocrysts are typically euhedral to subhedral and in the size range of 0·1–2·5 mm, although occasionally they reach 4 mm. Most olivine tholeiites contain olivine as the only phenocryst phase, but some also contain small amounts of plagioclase (0·5–2 mm in length), sometimes accompanied by clinopyroxene in the size range of 0·3–0·8 mm. The groundmass comprises plagioclase (40–75%), pyroxene (15–30%), microphenocryst olivine (0–5%), Fe–Ti oxides (2–5%) and glass (0–10%). Olivine tholeiites are the dominant lithology within the Hainan basalts. Quartz tholeiites are generally aphyric (<3% phenocrysts) to moderately phyric (<10% phenocrysts) with plagioclase, olivine and augite phenocrysts. Alkalic basalts are phyric (5–15% phenocrysts). Olivine occurs dominantly as phenocrysts in alkali basalts, and is euhedral to subhedral. It occasionally occurs in glomeroporphyritic aggregates. The assemblage of olivine + augite (i.e. without plagioclase) has also been noted. Alkali olivine basalts occur in the Leihuling, Qiongshan, and Penglai areas. The alkali and transitional basalts usually occur in the late phase of each volcanic episode and are abundant in the Holocene volcanism.

SAMPLE PREPARATION AND ANALYTICAL TECHNIQUES

Samples were sawn into slabs and the central parts (>200 g) were used for bulk-rock analysis. The rocks were crushed into small fragments (<0·5 cm in diameter) before being further cleaned and powdered in a corundum mill. Bulk-rock geochemical analyses were carried out at the Guangzhou Institute of Geochemistry, Chinese Academy of Sciences. Bulk-rock major element oxides were analyzed by X-ray fluorescence (XRF) with analytical uncertainties better than 3% for SiO_2, Al_2O_3, Fe_2O_3, MgO, CaO, Na_2O and K_2O, and better than 5% for TiO_2, MnO and P_2O_5. Trace elements were analyzed by inductively coupled plasma-mass spectrometry (ICP-MS). Repeated runs give <3% RSD (relative standard deviation) for most trace elements analyzed. Fe/Mn ratios

were also measured by inductively coupled plasma atomic emission spectrometry (ICP-AES). Precision for Fe/Mn ratios is generally better than 2%. Detailed analytical methods have been described by Liu *et al.* (1996) and Li *et al.* (2002, 2005).

Twelve groundmass samples were dated using the step-heating $^{40}Ar/^{39}Ar$ method. $^{40}Ar/^{39}Ar$ measurements were performed at the Institute of Geology and Geophysics of the Chinese Science Academy (IGGCAS), Beijing. To constrain the eruption age and avoid excess argon, groundmass grains in the size range of 0·2–0·3 mm were picked carefully under a binocular microscope to remove the visible phenocrysts and xenocrysts. The samples were cleaned with acetone followed by further cleaning with deionized water in an ultrasonic bath for three times, each for 40 min. The cleaned samples were then dried at ~100°C for 20 min. Groundmass wafers weighing 3–16 mg, and multiple samples of the 18·6 ± 0·4 Ma neutron fluence monitor mineral Brione muscovite, were irradiated *in vacuo* within a cadmium-coated quartz vial for 5 h in position H8 of the Beijing Atomic Energy Research Institute reactor (49-2). The argon isotopes were analysed using a MM5400 mass spectrometer. Further details about the step-heating $^{40}Ar/^{39}Ar$ method have been given by Wang *et al.* (2006).

Major element analyses of minerals were carried out using a JEOL JXA-8100 Superprobe at the IGGCAS. The operating conditions are: 15 kV accelerating voltage, 20 nA beam current, 3 μm beam diameter, and 10 s peak counting time for most elements (30 s for Ca and Ni in olivine, 7 s for Na and 8 s for K). The data reduction was carried out using ZAF correction.

Table 1: $^{40}Ar/^{39}Ar$ dating of the Hainan basalts

Sample	Eruptive episode	Position	Plateau age (Ma)	$^{40}Ar/^{39}Ar$ (initial)
08HN-5D	Shimacun	19°34′44″E 110°38′38·7″N	4·80 ± 0·30	295·8 ± 1·7
08HN-6D	Duowen (upper)	19°24′6″E 110°34′49·5″N	0·68 ± 0·44	296·1 ± 2·9
08HN-7A	Shimengou	19°59′48″E 109°38′53·7″N	2·45 ± 1·09	295·6 ± 3·8
08HN-10A	Shimengou	19°57′10·6″E 110°01′02·0″N	3·26 ± 0·60	295·4 ± 1·5
08HN-13A	Duowen (lower)	19°48′28·7″E 109°13′48·7″N	1·08 ± 0·19	297·1 ± 5·5
08HN-16C	Duowen (lower)	19°51′25·3″E 109°17′12″N	1·14 ± 0·11	297·0 ± 1·8
08HN-19A	Duowen (upper)	19°47′30″E 109°45′43·7″N	0·71 ± 0·12	295·4 ± 2·6
08HN-24B	Duowen (lower)	19°48′33·2″E 110°26′45·6″N	1·33 ± 0·15	296·2 ± 1·5
ZK05-20.1	Drill core at 20·1 m	19°33′30·8″E 110°39′10·1″N	4·63 ± 0·18	296·1 ± 5·3
ZK04-10.5	Drill core at 10·5 m	19°32′0·9″E 110°38′57·8″N	5·86 ± 0·35	296·9 ± 1·9
ZK04-26.8	Drill core at 26·8 m	110°38′57·8″N 110°38′57·8″N	12·89 ± 1·15	295·9 ± 1·5

RESULTS

$^{40}Ar/^{39}Ar$ age data

The age results from the step-heating experiments are presented in Table 1 and Figs 1b and 2. The $^{40}Ar/^{36}Ar$ initial ratios (Table 1) of all samples show no significant deviation from atmospheric values (295·5), suggesting that there is no excess argon component in the trapped argon from the samples and that the plateau ages are reliable. The plateau ages of all samples were obtained from at least three contiguous steps, comprising more than 70% cumulative ^{39}Ar released (Fig. 2). Samples 08HN-13A, 08HN-16C, and 08HN-24B from the lower section of the Duowen volcanism gave plateau ages of 1·08 ± 0·19 Ma, 1·14 ± 0·11 Ma, and 1·33 ± 0·15 Ma, respectively (Table 1, Fig. 2). Samples 08HN-6D and 08HN-19A are from the upper section of the Duowen volcanism and yielded plateau ages of 0·68 ± 0·44 Ma and 0·71 ± 0·12 Ma, respectively. These plateau ages define an age range of *c.* 1·3–0·6 Ma for the Duowen volcanism. Sample 08HN-7A is from the Shimengou volcanism and gave a plateau age of 2·49 ± 1·09 Ma, but this age is not regarded as reliable because of its poor plateau shape. Sample 08HN-10A from the upper section of the Shimengou volcanism gave a plateau age of 3·26 ± 0·60 Ma. Four samples (three drilling core samples ZK04-10·5, ZK04-26·8 and ZK05-20.1, and one surface sample 08HN-5D) were collected from the Penglai area (Fig. 2). Sample 08HN-5D is from the Shimengou volcanism and gave a plateau age of 4·80 ± 0·30 Ma. Drilling core samples ZK04-10.5 and ZK04-26.8 were collected at depths of 10·5 m and 26·8 m, respectively, from drilling core ZK04, which penetrated two layers of basalts. The lower layer occurs at depths between 32 and 21·9 m and is separated from the upper layer by about 9 m of sediments. The upper layer occurs at depths of between 13 and 8·2 m. Samples ZK04-10.5 and ZK04-26.8 gave plateau ages of 5·86 ± 0·35 Ma and 12·89 ± 1·15 Ma, respectively. Sample ZK05-20.1 gave a plateau age of 4·63 ± 0·18 Ma. These data indicate that eruption of the outcropping basalts in the Penglai area (the Shimengou–Shimacun volcanism) may have lasted from *c.* 6·0 to 3·0 Ma and incipient volcanism may have taken place in the late Miocene (about 13 Ma). Four samples (08HN-4D, 08HN-7A, 08HN-10A and ZK04-26.8) produced large errors in their plateau ages. This may be

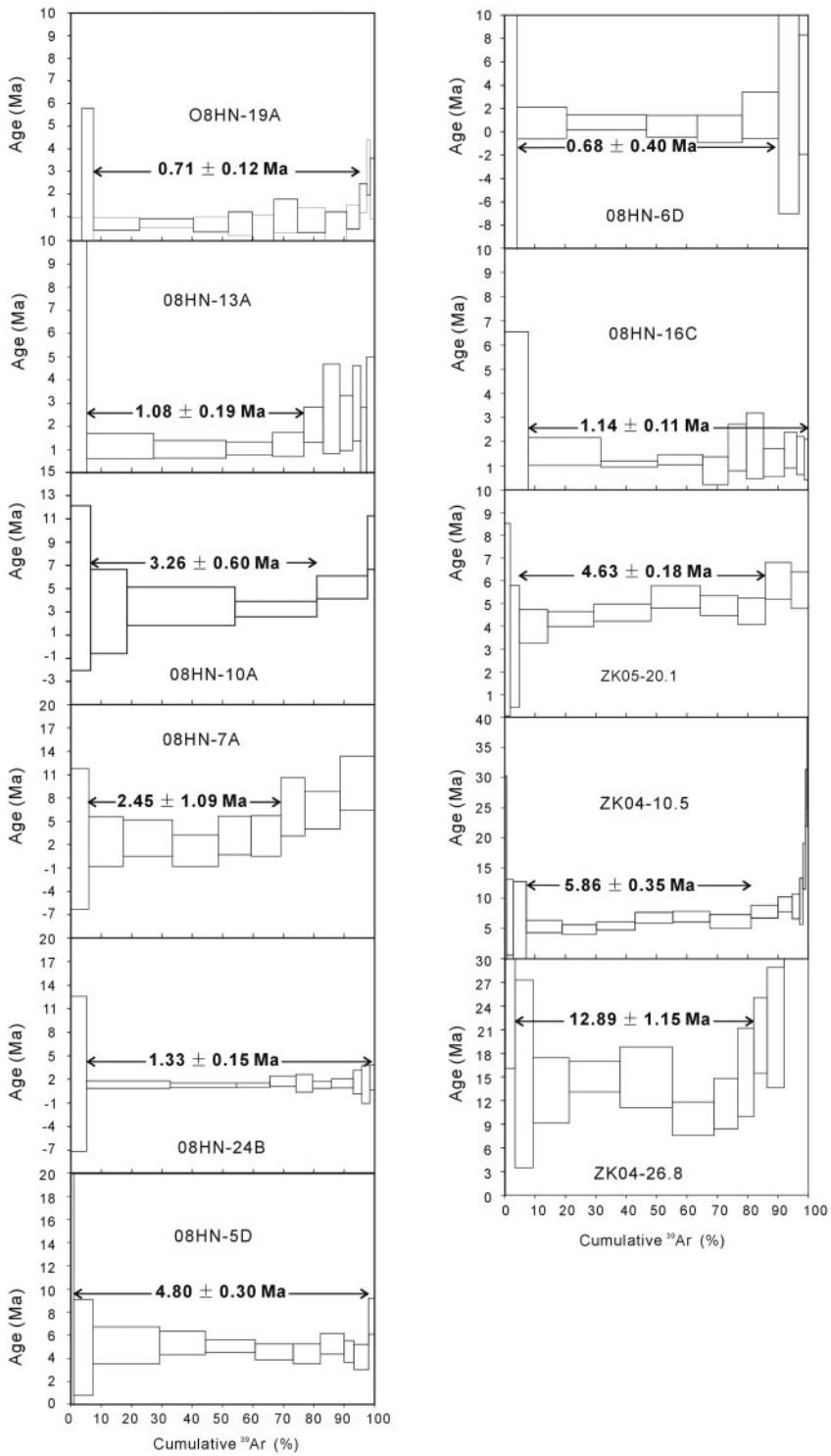

Fig. 2. Age spectra, integrated and plateau ages for the 11 samples studied.

attributed to the depletion of radiogenic ^{40}Ar because of the low K contents in the matrix of the rocks (K_2O ranging from 0·5 to 0·8 wt %; Table 2), and the effect of alteration on drilling core sample ZK04-26.8 [loss on ignition (LOI) = 4·2 wt %; Table 2]. All available ^{40}Ar/^{39}Ar data (including those obtained in this study), and some high-quality K–Ar data for the basalts are given in parentheses in Fig. 1b.

Table 2: Major element concentrations (in wt %) and normative mineral compositions (%) of the Hainan basalts

Sample:	08HN-1A	08HN-2A	08HN-2B	08HN-3	08HN-4A	08HN-4B	08HN-4C	08HN-4D	08HN-4G	08HN-5A	08HN-5B	08HN-5C	08HN-5D	08HN-5E	08HN-5F	08HN-5G	08HN-5H
Rock:	Olivine tholeiite	Alkali basalt	Alkali basalt	Olivine tholeiite	Quartz tholeiite	Quartz tholeiite	Quartz tholeiite	Olivine tholeiite	Olivine tholeiite	Olivine tholeiite	Olivine tholeiite	Olivine tholeiite	Olivine tholeiite	Olivine tholeiite	Quartz tholeiite	Olivine tholeiite	Olivine tholeiite
Episode:	1	1	1	1	1	1	1	1	1	1	1	1	1	1	1	1	1
Alteration:	Fresh	Fresh	Fresh	Fresh	Fresh	Fresh	Fresh	Fresh	Fresh	Slight	Fresh	Fresh	Fresh	Fresh	Fresh	Fresh	Slight
SiO_2	48·1	47·5	47·8	47·3	52·1	52	52	50·5	52	51·2	51·1	51	50·9	51·1	52·1	51·2	51
TiO_2	2·42	2·98	2·85	2·7	1·98	1·91	2·12	1·83	2·02	1·91	1·99	1·96	1·99	1·98	1·93	2	1·97
Al_2O_3	12·6	13	13·2	12·7	13·8	13·6	14	12·9	13·9	13·7	13·9	14	13·9	13·9	13·9	13·9	14
CaO	8·17	7·89	8	8·22	8·6	8·47	8·79	8·58	8·49	8·92	8·56	8·63	8·6	8·76	8·63	8·63	8·55
$Fe_2O_3^T$	12·5	13·2	13	13·5	11·6	11·8	11·6	12	11·6	12·3	11·9	11·9	12	11·8	11·8	11·8	11·9
K_2O	1·91	1·52	1·64	1·59	0·808	0·816	0·845	0·643	0·948	0·727	1·11	1·01	1·11	1·07	0·796	1·11	1·1
MgO	10·6	9·68	9·29	10·6	7·79	8·13	7·25	10·4	7·47	7·85	7·75	7·99	7·83	7·76	7·36	7·61	7·81
MnO	0·135	0·139	0·14	0·143	0·122	0·125	0·125	0·149	0·129	0·131	0·137	0·135	0·137	0·135	0·135	0·136	0·132
Na_2O	2·96	3·4	3·32	2·69	2·94	2·89	2·96	2·7	3·09	2·91	3·15	3·08	3·16	3·16	3·03	3·2	3·15
P_2O_5	0·635	0·671	0·688	0·489	0·238	0·225	0·32	0·278	0·281	0·298	0·356	0·346	0·363	0·364	0·275	0·367	0·357
Total	100	100	100	100	100	100	100	100	100	100	100	100	100	100	100	100	100
LOI	0·982	0·733	0·718	0·849	0·598	0·761	0·891	0·682	0·204	1·29	0·705	0·921	0·68	0·67	0·984	0·708	1·02
Mg#	65·1	61·7	61·1	63·3	59·7	60·2	57·8	65·6	58·5	58·4	58·9	59·6	59	59·1	57·8	58·7	59
Quartz	0	0	0	0	0·703	0·354	1·08	0	0	0	0	0	0	0	0·789	0	0
Orthoclase	11·6	9·13	9·79	9·51	4·83	4·88	5·05	3·85	5·67	4·35	6·64	6·05	6·63	6·39	4·76	6·64	6·6
Plagioclase	41·5	41·9	43	41·3	47·5	46·8	47·9	44·6	48·1	47·4	47·8	47·9	47·8	47·9	48·1	48	47·9
Nepheline	0	1·75	1·11	0	0	0	0	0	0	0	0	0	0	0	0	0	0
Diopside	12·4	15·6	15·5	16·1	15·7	15·5	15·9	16	15·6	16·6	16·2	15·9	16·4	16·9	15·8	16·6	16
Hypersthene	3·9	0	0	0·866	25·2	26·6	23·5	21·8	24·3	24	16·6	17·5	15·4	15·8	24·5	16·2	16·3
Olivine	22·5	22·3	21·6	23·9	0	0	0	7·78	0·066	1·49	6·35	6·22	7·4	6·56	0	6·14	6·8
Magnetite	1·86	1·94	1·91	1·99	1·7	1·73	1·71	1·76	1·71	1·8	1·75	1·75	1·76	1·73	1·74	1·73	1·75
Ilmenite	4·71	5·74	5·48	5·2	3·8	3·67	4·08	3·51	3·88	3·68	3·82	3·77	3·82	3·8	3·72	3·84	3·8
Apatite	1·51	1·58	1·62	1·15	0·558	0·528	0·751	0·651	0·658	0·7	0·834	0·811	0·85	0·853	0·644	0·86	0·836

(continued)

Table 2: Continued

Sample:	08HN-5I	08HN-5J	08HN-5K	08HN-6A	08HN-6B	08HN-6C	08HN-6D	08HN-6F	08HN-7A	08HN-7B	08HN-7D	08HN-7E	08HN-8A	08HN-8B	08HN-9A	08HN-9B
Rock:	Quartz tholeiite	Olivine tholeiite	Olivine tholeiite	Quartz tholeiite	Quartz tholeiite	Quartz tholeiite	Quartz tholeiite	Quartz tholeiite	Quartz tholeiite	Quartz tholeiite	Quartz tholeiite	Quartz tholeiite	Olivine tholeiite	Alkali basalt	Quartz tholeiite	Quartz tholeiite
Episode:	1	1	1	3	3	3	3	3	2	2	2	2	2	2	3	3
Alteration:	Fresh	Fresh	Fresh	Fresh	Fresh	Fresh	Fresh	Fresh	Fresh	Fresh	Fresh	Fresh	Fresh	Fresh	Fresh	Fresh
SiO_2	51·5	51	51·1	53·2	52·9	52·9	53·3	52·9	52·8	53·1	53·3	53·2	49·6	49·9	52·5	52·9
TiO_2	1·96	1·89	2·22	1·81	1·78	1·8	1·84	1·78	1·77	1·66	1·64	1·66	2·25	2·36	1·71	1·74
Al_2O_3	13·9	13·9	13·9	14·4	14·3	14·4	14·5	14·2	14·5	14·5	14·5	14·5	12·8	13·4	14·3	14·5
CaO	8·77	8·44	8·4	8·36	8·63	8·62	8·24	8·43	8·53	8·71	8·69	8·36	8·31	8·61	8·66	8·38
$Fe_2O_3^T$	12·1	12	12·7	12·3	12·4	12·3	12	12·7	12·6	12	11·9	12·1	12·7	12·3	13·2	12·7
K_2O	0·751	0·856	1·09	0·685	0·832	0·814	0·715	0·67	0·507	0·457	0·528	0·52	1·5	1·71	0·453	0·5
MgO	7·56	8·63	6·86	5·91	5·84	5·94	5·93	5·94	5·86	6·26	6·18	6·43	8·96	7·61	5·97	6·05
MnO	0·138	0·145	0·133	0·119	0·139	0·135	0·117	0·126	0·132	0·127	0·13	0·127	0·172	0·13	0·131	0·133
Na_2O	2·96	2·88	3·19	3·06	2·88	2·87	3·04	3	3·17	2·96	2·94	2·9	3·24	3·47	2·91	2·89
P_2O_5	0·305	0·333	0·353	0·231	0·224	0·223	0·234	0·227	0·188	0·158	0·158	0·168	0·442	0·48	0·174	0·176
Total	100	100	100	100	100	100	100	100	100	100	100	100	100	100	100	100
LOI	0·736	2·03	0·0101	0·53	0·789	0·672	0·801	0·71	0·49	0·168	0·0128	0·208	−0·181	0·176	0·273	0·233
Mg#	57·9	61·4	54·3	51·4	50·8	51·5	52·1	50·7	50·6	53·4	53·3	53·8	60·8	57·6	49·8	51·1
Quartz	0·023	0	0	3·76	3·65	3·54	4·14	3·5	2·92	3·83	4·1	4·09	0	0	3·44	4·14
Orthoclase	4·49	5·12	6·54	4·1	4·98	4·87	4·28	4·01	3·03	2·74	3·16	3·11	8·98	10·2	2·71	2·99
Plagioclase	48·1	47·4	48	50	48·7	49	50·2	49·4	51·3	50·7	50·4	50·3	43·9	45·6	49·8	50·3
Nepheline	0	0	0	0	0	0	0	0	0	0	0	0	0	0·186	0	0
Diopside	15·8	14·2	15·7	13·7	14·7	14·5	12·9	14·2	14·5	14·3	14·4	12·7	18·5	19·5	14·6	12·7
Hypersthene	25·3	22·7	19·3	22·6	22·2	22·4	22·6	23·1	22·6	23·1	22·7	24·4	3·56	0	23·9	24·2
Olivine	0	4·36	3·48	0	0	0	0	0	0	0	0	0	17·8	17	0	0
Magnetite	1·78	1·75	1·87	1·8	1·82	1·81	1·76	1·87	1·85	1·77	1·75	1·78	1·86	1·81	1·95	1·87
Ilmenite	3·76	3·63	4·28	3·48	3·42	3·45	3·53	3·42	3·41	3·18	3·16	3·2	4·33	4·53	3·28	3·34
Apatite	0·716	0·781	0·829	0·542	0·526	0·524	0·549	0·533	0·44	0·371	0·371	0·394	1·04	1·13	0·408	0·412

(continued)

Table 2: Continued

Sample:	08HN-9C	08HN-10A	08HN-10B	08HN-10C	08HN-11A	08HN-11B	08HN-12A	08HN-12B	08HN-13A	08HN-13B	08HN-14A	08HN-14B	08HN-15A	08HN-15B	08HN-16A
Rock:	Quartz tholeiite	Quartz tholeiite	Quartz tholeiite	Quartz tholeiite	Quartz tholeiite	Quartz tholeiite	Olivine tholeiite	Olivine tholeiite	Olivine tholeiite	Olivine tholeiite	Olivine tholeiite	Olivine tholeiite	Quartz tholeiite	Quartz tholeiite	Alkali basalt
Episode:	3	1	1	1	4	4	3	3	3	3	3	3	3	3	3
Alteration:	Fresh	Fresh	Fresh	Fresh	Fresh	Fresh	Slight	Fresh	Fresh	Fresh	Fresh	Fresh	Fresh	Fresh	Fresh
SiO_2	52·9	52·2	52·8	52·8	52·7	52·8	51·1	51·1	51·6	51·7	53·9	53·8	52·8	52·9	51·4
TiO_2	1·75	1·92	1·91	1·96	1·98	1·99	1·9	1·96	1·67	1·67	1·71	1·71	1·65	1·59	2·06
Al_2O_3	14·5	13·5	13·7	13·9	13·8	13·9	14	13·9	14·4	14·4	14·8	14·6	14·3	14·3	14·2
CaO	8·73	9·27	8·26	8·4	9·04	8·97	8·88	7·79	8·19	8·1	6·01	6·2	8·43	8·5	6·86
$Fe_2O_3^T$	11·8	11·7	11·8	11·4	11·4	11·2	11·3	11·9	11·7	11·8	10·4	10·4	12·3	12·3	11·3
K_2O	0·58	0·708	0·912	0·969	1·1	1·11	1·63	1·68	1·36	1·35	2·65	2·59	0·584	0·582	2·62
MgO	6	7·05	7·19	7·15	6·77	6·78	7·09	7·32	7·09	6·98	5·54	5·83	6·66	6·64	6·69
MnO	0·126	0·123	0·128	0·13	0·13	0·124	0·1	0·121	0·121	0·13	0·101	0·0992	0·134	0·134	0·11
Na_2O	3·41	2·97	3	3·08	2·88	2·9	3·56	3·73	3·56	3·56	4·52	4·45	3·01	2·99	4·3
P_2O_5	0·176	0·26	0·258	0·264	0·272	0·269	0·391	0·391	0·294	0·293	0·439	0·427	0·172	0·163	0·479
Total	100	100	100	100	100	100	100	100	100	100	100	100	100	100	100
LOI	0·195	0·871	0·0156	−0·163	0·533	0·343	1·61	−0·622	−0·17	−0·0149	−0·284	−0·472	−0·324	−0·412	−0·462
Mg#	52·7	57	57·3	58	56·7	57·2	58	57·4	57·2	56·5	54	55·3	54·4	54·4	56·7
Quartz	1·61	0·819	1·89	1·46	1·89	2·1	0	0	0	0	0	0	2·59	2·67	0
Orthoclase	3·47	5·43	5·46	5·79	6·55	6·6	9·73	10·1	8·13	8·08	15·8	15·5	3·49	3·48	15·6
Plagioclase	52·1	46·6	47·2	47·8	46·4	46·6	48·2	48·4	50	50·1	51	50·3	49·8	49·7	42·7
Nepheline	0	0	0	0	0	0	0	0	0	0	0	0	0	0	3·3
Diopside	16·3	19·4	15	15·5	17·9	17·6	19·8	16·4	16·1	15·7	12·2	13·2	14·2	14·5	15·8
Hypersthene	21	21·7	24·4	23·4	21·2	21	2·39	3·78	10	11·2	2·25	2·12	24·5	24·5	0
Olivine	0	0	0	0	0	0	13·6	14·9	10·1	9·32	12·9	13·2	0	0	15·8
Magnetite	1·74	1·72	1·73	1·67	1·67	1·64	1·66	1·75	1·72	1·73	1·52	1·52	1·8	1·8	1·65
Ilmenite	3·36	3·69	3·68	3·76	3·81	3·82	3·66	3·77	3·21	3·21	3·28	3·27	3·17	3·05	3·96
Apatite	0·412	0·609	0·605	0·619	0·637	0·63	0·915	0·917	0·688	0·686	1·03	0·999	0·403	0·382	1·12

(continued)

Table 2: Continued

Sample:	08HN-16B	08HN-16C	08HN-17A	08HN-17B	08HN-18A	08HN-18B	08HN-18C	08HN-18D	08HN-19A	08HN-19B	08HN-19C	08HN-19D	08HN-20A	08HN-20B	08HN-21A
Rock:	Alkali basalt	Alkali basalt	Olivine tholeiite	Alkali basalt	Quartz tholeiite	Quartz tholeiite	Quartz tholeiite	Quartz tholeiite	Alkali basalt	Alkali basalt	Alkali basalt	Alkali basalt	Olivine tholeiite	Olivine tholeiite	Olivine tholeiite
Episode:	3	3	3	3	3	3	3	3	3	3	3	3	3	3	3
Alteration:	Fresh	Fresh	Fresh	Fresh	Fresh	Fresh	Fresh	Fresh	Fresh	Fresh	Fresh	Fresh	Fresh	Fresh	Fresh
SiO_2	51·3	51·4	55·7	55·5	52·8	52·8	52·9	52·8	48·1	48·1	48·4	48·4	51	51·1	52·1
TiO_2	2·09	2·04	1·54	1·53	1·63	1·59	1·61	1·62	3·19	3·15	3·16	3·19	2·41	2·43	1·92
Al_2O_3	14·2	14·1	15	14·9	14·2	14·3	14·2	14·3	13·1	13	13	13·3	13·6	13·6	14·3
CaO	7·03	6·94	4·9	4·86	8·48	8·47	8·4	8·46	8·6	8·63	8·68	8·52	8·13	8·06	8·11
$Fe_2O_3^T$	11·4	11·3	9·1	9·04	12·5	12·4	12·5	12·4	12·9	12·8	12·8	12·8	12·2	12·2	11·8
K_2O	2·55	2·59	3·46	3·46	0·563	0·524	0·563	0·513	1·91	1·89	1·89	1·95	1·35	1·36	1·22
MgO	6·8	6·79	4·89	4·96	6·56	6·71	6·62	6·66	8·22	8·22	8·04	7·82	7·46	7·37	6·9
MnO	0·114	0·113	0·0856	0·0904	0·134	0·126	0·127	0·131	0·159	0·137	0·14	0·155	0·134	0·123	0·127
Na_2O	4·1	4·28	4·89	5·11	2·96	2·95	2·95	2·96	3·19	3·34	3·27	3·3	3·37	3·31	3·27
P_2O_5	0·481	0·474	0·494	0·474	0·176	0·166	0·174	0·171	0·661	0·651	0·646	0·677	0·405	0·409	0·315
Total	100	100	100	100	100	100	100	100	100	100	100	100	100	100	100
LOI	−0·261	−0·541	0·197	−0·00763	0·524	0·361	0·327	0·405	−0·389	−0·513	−0·407	−0·413	−0·401	−0·219	−0·298
Mg#	56·8	57·1	54·2	54·7	53·6	54·4	53·9	54·2	58·4	58·5	58·1	57·4	57·4	57·1	56·3
Quartz	0	0	0	0	2·9	2·9	3·1	2·99	0	0	0	0	0	0	0
Orthoclase	15·2	15·5	20·6	20·6	3·37	3·13	3·37	3·07	11·4	11·3	11·3	11·7	8·06	8·14	7·29
Plagioclase	43·8	42·4	50·4	48·9	49·5	49·7	49·4	49·8	41·2	40	41·2	41·9	47	46·8	48·9
Nepheline	2·28	3·28	0	1·29	0	0	0	0	1·14	2·08	1·17	1·17	0	0	0
Diopside	15·7	16·3	10·3	11·1	14·3	14	14	13·9	18·7	19·4	19·6	18·4	16·4	15·8	14·5
Hypersthene	0	0	1·07	0	24·6	25	24·9	24·9	0	0	0	0	13·2	15·4	21·1
Olivine	16·2	15·9	12·1	12·7	0	0	0	0	18	17·7	17·2	17·2	7·99	6·4	2·06
Magnetite	1·67	1·65	1·33	1·32	1·83	1·82	1·83	1·82	1·89	1·89	1·88	1·88	1·79	1·79	1·73
Ilmenite	4·01	3·92	2·94	2·94	3·14	3·06	3·09	3·12	6·14	6·05	6·09	6·14	4·64	4·68	3·69
Apatite	1·13	1·11	1·15	1·11	0·412	0·389	0·408	0·401	1·55	1·53	1·52	1·59	0·95	0·959	0·739

(continued)

Table 2: Continued

Sample:	08HN-21B	08HN-21C	08HN-21D	08HN-21E	08HN-22A	08HN-22B	08HN-22C	08HN-22D	08HN-23A	08HN-23B	08HN-24A	08HN-24B	08HN-24C	08HN-24D	08HN-25A
Rock:	Olivine tholeiite	Olivine tholeiite	Olivine tholeiite	Quartz tholeiite	Olivine tholeiite	Alkali basalt	Alkali basalt	Alkali basalt	Alkali basalt	Olivine tholeiite	Alkali basalt	Alkali basalt	Olivine tholeiite	Alkali basalt	Olivine tholeiite
Episode:	3	3	3	3	5	5	5	5	5	5	2	2	2	2	5
Alteration:	Fresh	Fresh	Fresh	Fresh	Fresh	Fresh	Fresh	Fresh	Fresh	Fresh	Fresh	Fresh	Fresh	Fresh	Fresh
SiO_2	51·9	52·2	52·2	53·1	49·3	49·3	49·5	46·6	49·4	49·2	48	47·8	50·6	48	49·8
TiO_2	1·85	1·95	1·96	2·1	2·51	2·5	2·58	2·64	2·6	2·55	2·43	2·41	2·05	2·33	2·1
Al_2O_3	14·2	14·2	14·2	14·1	13·4	13·3	13·5	12·9	13·5	13·3	13	13·1	14·2	13·2	13·7
CaO	8·08	8·02	8·02	8·13	9·03	9·05	9·15	9·85	8·99	9·05	9·5	9·37	8·57	9·47	8·92
$Fe_2O_3^T$	12	12	12	11·5	12	11·9	11·8	13·2	12	12	12·3	12·6	12	12·3	12·4
K_2O	1·18	1·22	1·17	1·23	1·92	1·91	1·99	1·67	1·92	1·96	1·59	1·55	1·26	1·51	1·43
MgO	7·05	6·61	6·67	5·92	8·28	8·25	7·52	9·25	7·8	8·31	9·55	9·78	7·85	9·8	8·18
MnO	0·126	0·127	0·132	0·119	0·137	0·136	0·133	0·161	0·142	0·138	0·144	0·147	0·129	0·145	0·149
Na_2O	3·3	3·34	3·32	3·42	3·01	3·15	3·27	3·05	3·18	2·94	2·98	2·85	2·86	2·73	3
P_2O_5	0·312	0·333	0·333	0·358	0·493	0·493	0·506	0·625	0·519	0·511	0·473	0·443	0·356	0·441	0·354
Total	100	100	100	100	100	100	100	100	100	100	100	100	100	100	100
LOI	−0·537	−0·262	−0·264	0·65	−0·389	−0·559	−0·607	−0·617	−0·52	−0·183	−0·623	−0·393	0·122	−0·155	−0·21
Mg#	56·5	54·8	55·1	53·1	60·4	60·5	58·3	60·6	59	60·4	63	63·1	59	63·7	59·2
Quartz	0	0	0	1·43	0	0	0	0	0	0	0	0	0	0	0
Orthoclase	7·03	7·29	6·99	7·36	11·5	11·4	11·9	10	11·5	11·7	9·53	9·26	7·56	9·04	8·56
Plagioclase	49·1	48·9	49	49·1	43·3	42·4	42·3	34·2	43·6	42·7	39·3	40·2	47	42·1	45·6
Nepheline	0	0	0	0	0	0·745	1·23	4·8	0·308	0	2·12	1·48	0	0·467	0
Diopside	14·5	14·6	14·4	15·4	20	20·6	21·3	23·2	20·2	20	21·8	20·8	14·8	20·4	18·4
Hypersthene	20	21·9	22·8	20·2	0·094	0	0	0	0	0·748	0	0	18·1	0	7·02
Olivine	3·4	1·06	0·587	0	17·4	17·1	15·4	19·3	16·4	17	19·6	20·7	5·98	20·7	13·7
Magnetite	1·75	1·76	1·76	1·69	1·76	1·74	1·74	1·94	1·75	1·76	1·81	1·85	1·77	1·81	1·82
Ilmenite	3·56	3·74	3·76	4·03	4·83	4·81	4·96	5·08	5	4·91	4·67	4·64	3·93	4·49	4·04
Apatite	0·732	0·781	0·781	0·839	1·16	1·16	1·19	1·47	1·22	1·2	1·11	1·04	0·834	1·03	0·829

(continued)

Table 2: Continued

Sample:	08HN-25B	08HN-25C	08HN-26A	08HN-26B	08HN-26C	08HN-26D	ZK03-18.1	ZK03-20.1	ZK03-24.4	ZK03-25	ZK03-27	ZK03-27·5	ZK03-29.1	ZK03-30	ZK03-31
Rock:	Olivine tholeiite	Olivine tholeiite	Olivine tholeiite	Olivine tholeiite	Olivine tholeiite	Olivine tholeiite	Quartz tholeiite	Quartz tholeiite	Basanite	Basanite	Basanite	Alkali basalt	Alkali basalt	Olivine tholeiite	Basanite
Episode:	5	5	4	4	4	4	1	1	1	1	1	1	1	1	1
Alteration:	Fresh	Fresh	Fresh	Fresh	Fresh	Fresh	Slight	Slight	Slight	Slight	Slight	Slight	Slight	Slight	Moderate
SiO_2	50	50·3	51·2	51·2	51·4	51·4	52·4	52·4	46·1	46·1	46·8	46·7	46·2	46·7	45·9
TiO_2	2·11	2·06	2·13	2·28	2·15	2·18	1·86	1·95	2·51	2·56	2·72	2·62	2·68	2·75	2·66
Al_2O_3	13·8	13·9	14·1	14	14·2	14·1	14·1	13·9	13·2	13·1	13·9	13·4	13·4	13·7	13·1
CaO	8·61	8·52	8·95	8·8	8·93	8·91	8·88	8·7	9·88	10·1	10·3	10·3	10·4	10·5	10·1
$Fe_2O_3^T$	12·6	12·5	11·6	11·8	11·5	11·6	12·4	11·7	13·7	13·6	14·7	13·7	13·6	14·8	14·1
K_2O	1·28	1·2	1·34	1·37	1·35	1·37	0·511	0·877	2·01	1·93	1·46	1·48	1·83	2·14	2·16
MgO	8·12	8·11	7·08	6·81	6·88	6·85	6·68	7·03	7·57	7·91	6·62	7·32	7·38	5·54	7
MnO	0·135	0·138	0·129	0·132	0·129	0·13	0·101	0·147	0·192	0·194	0·18	0·217	0·18	0·176	0·271
Na_2O	3·05	3	3·2	3·25	3·2	3·22	2·81	3·06	3·74	3·27	2·02	2·93	3·02	2·2	3·46
P_2O_5	0·356	0·345	0·349	0·362	0·351	0·359	0·259	0·285	1·21	1·22	1·3	1·23	1·34	1·39	1·32
Total	100	100	100	100	100	100	100	100	100	100	100	100	100	100	100
LOI	−0·155	−0·256	−0·421	−0·613	−0·4	−0·513	2·17	1·22	1·29	2·34	2·15	2·88	2·64	2·93	4·68
Mg#	58·7	58·8	57·4	56·1	56·9	56·6	54·3	57	55	56·2	49·8	54	54·5	45·1	52·3
Quartz	0	0	0	0	0	0	3·21	1·14	0	0	0	0	0	0	0
Orthoclase	7·65	7·17	7·99	8·22	8·05	8·17	3·06	5·24	12	11·6	8·76	8·84	11	12·9	12·9
Plagioclase	46·5	46·8	47·7	47·7	47·9	47·7	48·8	48	29·5	32·8	42·2	42·5	36·9	40·4	30·1
Nepheline	0	0	0	0	0	0	0	0	8·63	5·9	0	1·07	3·66	0	7·44
Diopside	16·8	15·8	18·3	17·9	18	18·2	15	16·3	23·2	22·2	15·1	20·1	21·1	18·5	22·8
Hypersthene	10·4	14	12·9	13·4	14·3	13·9	23·9	23·1	0	0	17·1	0	0	6·28	0
Olivine	11·9	9·56	6·5	5·78	5·12	5·34	0	0	16·9	17·7	6·36	17·5	17·1	11·2	16·4
Magnetite	1·85	1·83	1·7	1·72	1·68	1·7	1·82	1·71	2·01	1·99	2·16	2·02	2	2·18	2·07
Ilmenite	4·06	3·96	4·1	4·38	4·14	4·2	3·58	3·75	4·83	4·92	5·25	5·05	5·17	5·31	5·12
Apatite	0·834	0·809	0·818	0·848	0·822	0·841	0·607	0·667	2·85	2·87	3·06	2·88	3·14	3·27	3·11

(continued)

Table 2: Continued

Sample:	ZK04-10.5	ZK04-26.8	ZK04-30.7	ZK04-9.2	ZK05-20.1	ZK05-22.3	ZK05-25.4	ZK05-28.1	ZK05-32.1	ZK05-33.6	ZK05-36.5
Rock:	Quartz tholeiite	Quartz tholeiite	Quartz tholeiite	Quartz tholeiite	Quartz tholeiite	Quartz tholeiite	Quartz tholeiite	Quartz tholeiite	Quartz tholeiite	Olivine tholeiite	Quartz tholeiite
Episode:	1	1	1	1	1	1	1	1	1	1	1
Alteration:	Slight	Moderate	Moderate	Slight	Slight	Slight	Slight	Slight	Slight	Slight	Severe
SiO_2	52·8	52·9	54·2	52·7	51·8	52	51·6	51·6	50·9	49·4	47·5
TiO_2	1·93	1·91	2·73	1·88	1·81	1·97	1·92	1·89	1·96	1·99	2·14
Al_2O_3	13·9	14·3	19·8	13·9	14·1	14	13·8	14·1	14·4	14·6	15·4
CaO	9·05	11·5	8·29	8·97	9·06	9·01	8·95	9·18	8·75	8·41	10·344
$Fe_2O_3^T$	12·1	11·4	8·63	11·8	11·8	11·8	12·1	11·6	12·3	13·7	14·1
K_2O	0·767	0·833	0·388	0·731	0·434	0·618	0·397	0·314	0·451	0·416	0·302
MgO	5·97	4·83	1·86	6·53	7·77	7·13	8·09	8·07	8·07	8·56	7·4
MnO	0·156	0·187	0·134	0·135	0·12	0·124	0·125	0·134	0·129	0·133	0·360
Na_2O	3·14	2·96	3·5	3·09	2·81	2·98	2·73	2·76	2·74	2·54	2·24
P_2O_5	0·25	0·262	0·465	0·237	0·276	0·3	0·311	0·307	0·311	0·292	0·36
Total	100	100	100	100	100	100	100	100	100	100	100
LOI	2·43	4·21	3·66	1·63	1·52	1·57	1·05	1·95	2·59	2·79	8·64
Mg#	52·1	50·6	32·2	54·8	59·2	57	59·6	60·4	59	57·8	53·7
Quartz	2·36	3·06	9·87	1·99	1·36	1·4	1·43	1·43	0·254	0	0
Orthoclase	4·59	4·98	2·31	4·37	2·59	3·69	2·38	1·88	2·7	2·49	1·97
Plagioclase	48·6	48·8	67·4	48·6	49	48·9	47·9	49·1	49·4	49·2	50·5
Nepheline	0	0	0	0	0	0	0	0	0	0	0
Diopside	18·2	26·7	0·755	17·5	15·3	16·3	15	15·2	13·1	10·6	15·1
Hypersthene	20·1	10·6	12·1	21·6	25·9	23·5	27·1	26·4	28·2	27·1	17·9
Olivine	0	0	0	0	0	0	0	0	0	4·05	7·38
Magnetite	1·78	1·52	1·26	1·74	1·73	1·73	1·77	1·71	1·81	2·02	2·07
Ilmenite	3·71	3·67	5·23	3·61	3·48	3·8	3·7	3·63	3·77	3·82	4·13
Apatite	0·586	0·614	1·09	0·556	0·646	0·704	0·73	0·721	0·73	0·686	0·843

$Mg\# = Mg/(Mg + Fe^{2+})$, assuming $Fe^{3+}/Fe_{total} = 0{\cdot}10$, cation ratio. $Fe_2O_3^T$, total iron as Fe_2O_3. Episodes: 1, Pliocene–Miocene (Shimengou and Shimacun volcanism); 2, early to middle Pleistocene (Duowen volcanism); 3, middle Pleistocene (Dongying volcanism); 4, late Pleistocene (Daotang volcanism); 5, Holocene (Shishan volcanism). The distribution of the episodic volcanism is shown in Fig. 1b.

Bulk-rock major and trace element compositions

Most studied samples have low LOI values (<1·0 wt %) and insignificant secondary minerals, indicating that these samples are fresh. Only four drilling core samples (ZK03-31, ZK04-30.7, ZK04-10.5, and ZK05-36.5) have LOI values >3 wt %. Bulk-rock chemical compositions of the Hainan basalts are listed in Tables 2 and 3. All the samples have <56 wt % SiO_2. A distinctive compositional feature of the Hainan basalts is the broad scatter in SiO_2, FeO^T, CaO, TiO_2, and K_2O. The total alkali contents ($Na_2O + K_2O$) of the basalts are higher than 2·6 wt % and the Na_2O/K_2O ratios of all basalts studied are more than unity (mostly >2), indicating their alkali-enriched and high-sodium nature. Most of the studied samples are silica-saturated with SiO_2 >50 wt %. Forty-one samples contain normative quartz (Table 2). CIPW-normative compositions of the studied samples span the range from quartz tholeiite (QT) (quartz-normative), olivine tholeiite (OT) (olivine + hypersthene) to alkali basalt (AB) (nepheline <5%), with tholeiite being the dominant rock type and alkali basalts subordinate (Fig. 3a; Table 2). Only three samples (ZK03-25, ZK03-31 and ZK03-24-4) contain >5% nepheline and were classified as basanite (e.g. Flower *et al.*, 1992). On a total alkalis–silica (TAS) diagram (Fig. 3b), the samples plot predominantly within the sub-alkaline field, with the alkaline series field being subordinate. For the alkaline series, the total alkalis increase with increasing SiO_2, and two samples with high SiO_2 (55·6–55·7%) and $Na_2O + K_2O$ (8·3–8·6%) plot into the trachyandesite field (Fig. 3b).

The MgO contents of the bulk-rocks range from 2 to 11 wt %, with 86 of 105 samples having >6 wt % MgO and 25 samples having MgO >8 wt % (Table 2). Figure 4 shows that the Ni and Cr contents in all analysed samples correlate positively with Mg#, whereas the other elements show complex behaviors. The SiO_2 and Al_2O_3 contents in tholeiites increase with falling Mg# and reach their maximum values at Mg# ≈ 55–60, whereas at lower Mg# values (<55), SiO_2 contents decrease slightly with falling Mg# (Fig. 4a and b). The tholeiites mostly fall within a narrow range of CaO contents (8–9 wt %; highlighted by the grey band in Fig. 4c), FeO^T (11·5–10 wt %; Fig. 4d), and CaO/Al_2O_3 values (0·55–0·65; Fig. 4i). The tholeiites have nearly constant Zn/Fe ratios ($Zn/Fe \times 10^4 = 10–13$; Fig. 4h). The alkali basalts show scattered SiO_2 and nearly constant Al_2O_3 contents (Fig. 4a and b) whereas the CaO and FeO^T contents display more complex behavior. CaO contents increase with falling Mg# at Mg# > 64 and reach maximum values at Mg# = 64–65 (Fig. 4c). With further decrease in Mg#, CaO contents quickly decrease from >11 wt % to about 9 wt % at Mg# ~60 and then flatten out (Fig. 4c). FeO^T contents in the alkali basalts first increase from about 10 wt % to 12 wt % with falling Mg# at Mg# ≥ 63, then decrease quickly from >12 wt % to about 8 wt % with decreasing Mg# from 63 to 55, and finally increase again when Mg# falls to <55 (Fig. 4d). At high Mg# >61, the alkali basalts also have nearly constant Zn/Fe ratios, but the ratio correlates negatively with Mg# at Mg# <60–61 (Fig. 4h). Na_2O contents in both the tholeiites and alkali basalts increase with falling Mg# and reach their maximum values at Mg# = 54 and 58, respectively. The Sc contents in the tholeiites and alkali basalts correlate negatively with Mg# at Mg# > 64, reach their maximum value at Mg# = 61–64 (Fig. 4j), and then decrease from about 25 to 15 ppm at Mg# < 61 (Fig. 4j).

The fundamental differences between the tholeiites and the alkali basalts are in their SiO_2, Al_2O_3, FeO^T, TiO_2, and K_2O contents. As shown in Fig. 4 and Table 2, the tholeiites are characterized by higher SiO_2 (mostly ≥51 wt %) and Al_2O_3 (mostly >14·5 wt %) and lower FeO^T (mostly ≤11 wt %), TiO_2 (mostly <2·3 wt %), and K_2O (mostly <1·5 wt %), whereas the alkali basalts have relatively low SiO_2 (mostly ≤49 wt %) and Al_2O_3 (mostly <14·5 wt %), but higher FeO^T (mostly >11 wt %), TiO_2 (mostly >2·3 wt %), and K_2O (mostly >1·5 wt %).

The Fe/Mn ratio an important indicator of the source of basaltic rocks (Liu *et al.*, 2008, and references therein). In this study, Fe/Mn ratios can be directly measured by ICP-AES or be calculated according to Fe (by XRF) and Mn (by XRF or ICP-MS) contents. Fe/Mn ratios determined in the three different ways display no systematic differences (Fig. 5).

Both tholeiites and alkali basalts are characterized by high Fe/Mn ratios with an average of 74 (mostly >70, Figs 5 and 6), which is significantly higher than the average of mid-ocean ridge basalt (MORB; 57, $n = 875$, RidgePeDB), continental flood basalts (63·7, $n = 4780$, GEOROC), Hawaiian OIB (about 66–67; Humayun *et al.* 2004) and Mesozoic to Cenozoic basalts in eastern China (60–70; Liu *et al.* 2008). All but two samples plot within or above the field of primitive upper mantle (PUM; highlighted by the grey band in Fig. 6). Samples with LOI >1·5 wt % display negative and positive correlations of Fe/Mn–LOI and MnO–LOI, respectively (Fig. 6a and b). This indicates that the Fe/Mn ratios in the few relatively high LOI samples were affected by alteration processes, resulting in reductions in the Fe/Mn ratio (e.g. samples ZK04-26.8 and ZK05-36.5). Considering the effect of any undetected alteration on the Hainan basalts, their primary Fe/Mn ratios could be even higher.

The Fe/Mn ratios of the studied samples correlate negatively with heavy rare earth element (HREE) abundances (e.g. Yb; correlation coefficient $r = -0·53$; Fig. 6c), Lu ($r = -0·52$; not shown) and CaO ($r = -0·51$; Fig. 6e), but not with Mg# and FeO^T (Fig. 6d and f). This suggests that magmatic differentiation had little effect on the

Table 3: Trace element concentrations (in ppm) of the Hainan basalts

Sample:	08HN-1A	08HN-2A	08HN-2B	08HN-3	08HN-4B	08HN-4C	08HN-4D	08HN-5C	08HN-5D
Sc	16·7	17·9	16·8	20	20·4	21·4	21	20·8	20·1
Ti	13542	16400	14780	14480	10824	12572	10830	11080	10824
V	135	156	144	159	142	154	142	150	154
Cr	373	284	248	314	273	207	386	214	196
Mn	1107	1197	1118	1161	1028	1048	1190	1094	1120
Co	48·7	50·5	47	55·9	43·7	40·5	49·5	41·6	43·3
Ni	315	268	248	307	191	168	310	156	162
Cu	37·7	47·8	41·2	51·4	60·6	66·4	53·3	56·6	57·7
Zn	130	140	125	120	113	114	104	105	109
Ga	20·6	21·6	20·3	19·5	18·5	19·8	17·2	18·5	18·8
Ge	1·57	1·46	1·48	1·58	1·66	1·52	1·48	1·52	1·46
Rb	33·8	50	50·1	26·4	15·8	13·4	6·44	15·9	21·9
Sr	602	764	906	587	318	382	388	391	429
Y	22·8	23	23·2	20·3	17·1	19·9	16·6	19	20·5
Zr	255	264	260	189	106	138	115	126	138
Nb	55·6	61·2	58·8	41·7	18·1	27	23·9	29·6	31·2
Ba	497	626	870	424	185	221	231	284	339
La	38·1	39·7	40·3	26·7	12·4	18	17·4	21	22·7
Ce	78·4	81·8	82	55·1	25·6	36·3	34·6	41·6	45·2
Pr	9·64	10·2	10·2	7·11	3·27	4·5	4·22	5	5·43
Nd	37·6	41	41·2	29·7	14·2	19·1	17·2	20·2	22·1
Sm	7·87	8·76	8·62	6·72	3·86	4·71	4·08	4·8	5·12
Eu	2·52	2·87	2·85	2·26	1·44	1·75	1·52	1·7	1·78
Gd	7·01	7·94	7·57	6·35	4·25	5·13	4·33	5·15	5·29
Tb	1·06	1·1	1·05	0·895	0·687	0·767	0·678	0·826	0·823
Dy	5·07	5·52	5·4	4·49	3·83	4·11	3·68	4·38	4·44
Ho	0·885	0·933	0·898	0·779	0·693	0·735	0·653	0·76	0·816
Er	2·07	2·22	2·12	1·86	1·78	1·86	1·58	1·96	2·01
Tm	0·267	0·269	0·266	0·244	0·224	0·237	0·207	0·255	0·257
Yb	1·46	1·53	1·56	1·42	1·31	1·39	1·23	1·49	1·51
Lu	0·2	0·207	0·218	0·209	0·192	0·199	0·181	0·214	0·222
Hf	5·85	6·23	6·25	4·55	2·76	3·41	2·96	3·25	3·34
Ta	3·6	4·18	3·98	2·81	1·13	1·57	1·5	1·74	1·84
Pb	5·14	2·69	2·4	1·88	5·45	1·34	1·57	4·43	1·61
Th	5·03	5·2	5·2	3·65	1·85	2·8	2·61	3·04	3·51
U	1·2	1·26	1·28	0·895	0·426	0·594	0·572	0·647	0·74
Sr*	0·815	0·97	1·15	1·07	1·22	1·07	1·17	0·99	0·998
Fe/Mn^1	79	76·5	80·7	80·7	79·6	76·8	69·9	75·4	74·3
Fe/Mn^2	79	77·3	81·5	81·6	80·4	77·7	70·6	76·3	74·9
Fe/Mn^3	83·6	85·7	83·8	85·2	85·2	83·8	72·6	79·5	79
Zr/Hf	43·6	42·3	41·6	41·6	38·3	40·4	39	38·6	41·3
Nb/Ta	15·4	14·6	14·8	14·9	16	17·3	15·9	17·1	17
Lu/Hf	0·034	0·033	0·035	0·046	0·07	0·058	0·061	0·066	0·067
Sm/Nd	0·209	0·214	0·209	0·226	0·272	0·246	0·237	0·237	0·232

(continued)

Table 3: Continued

Sample:	08HN-5E	08HN-5F	08HN-5I	08HN-5J	08HN-5K	08HN-6A	08HN-6C	08HN-6D	08HN-7B	08HN-7E
Sc	20·9	20·9	22·3	20·5	22	20·3	21·4	20·2	22·2	21·3
Ti	11010	11072	11648	10355	12152	10547	10554	10180	9699	9375
V	175	146	152	140	161	141	144	136	142	133
Cr	209	200	196	214	171	138	150	154	167	170
Mn	1102	1078	1152	1235	1082	960	1153	940	1028	1079
Co	43·2	41·9	40·2	45	41·5	38·9	41	39·4	41·6	43·2
Ni	162	152	145	176	134	95·2	98·9	96·5	99·5	102
Cu	58·4	64·3	60·6	59·6	65	53·4	55·6	40·4	51·9	51
Zn	108	109	109	108	123	111	112	116	109	107
Ga	18·7	19·2	19·2	18·7	19·8	19·6	19·9	20·5	19·8	19·3
Ge	1·47	1·52	1·49	1·58	1·57	1·47	1·46	1·62	1·65	1·42
Rb	17·7	12·1	14·3	11·6	23·5	8·98	12·4	9·92	6·44	7·07
Sr	431	350	387	380	367	310	327	325	268	209
Y	20·2	19·7	20·3	19·4	22·1	17	16·6	17·3	17·4	16·4
Zr	135	116	124	125	146	111	110	117	90·6	90·4
Nb	31	20·7	25	28·5	28·6	14·6	14·6	15·7	9·69	10·1
Ba	335	205	228	292	239	145	136	151	81·8	93·9
La	22·6	15·7	18	20·4	20·1	11·3	11·3	11·7	8·19	8·44
Ce	45	31·8	36·4	40·8	40·8	24·2	24·7	25·7	17·6	18·5
Pr	5·49	3·98	4·59	4·98	5·12	3·23	3·3	3·36	2·56	2·71
Nd	21·7	16·9	18·4	20·3	21·3	14·4	14·5	14·6	12·2	12·7
Sm	4·96	4·46	4·57	4·77	5·07	3·97	3·97	4·04	3·56	3·71
Eu	1·7	1·57	1·68	1·64	1·7	1·46	1·48	1·53	1·36	1·44
Gd	5·25	4·81	5·05	4·87	5·49	4·32	4·27	4·43	4·1	4·15
Tb	0·83	0·782	0·8	0·773	0·887	0·716	0·708	0·702	0·678	0·678
Dy	4·46	4·27	4·3	4·16	4·74	3·91	3·79	3·75	3·81	3·72
Ho	0·801	0·779	0·77	0·772	0·874	0·715	0·687	0·672	0·708	0·699
Er	1·97	1·92	1·96	1·9	2·14	1·79	1·73	1·62	1·77	1·72
Tm	0·274	0·263	0·269	0·253	0·283	0·238	0·228	0·228	0·233	0·229
Yb	1·53	1·5	1·54	1·52	1·7	1·39	1·33	1·29	1·38	1·34
Lu	0·22	0·222	0·218	0·225	0·24	0·205	0·188	0·2	0·197	0·2
Hf	3·33	3·21	3·17	3·27	3·82	3·08	2·93	3·04	2·56	2·54
Ta	1·8	1·28	1·5	1·7	1·8	0·957	0·912	0·934	0·609	0·63
Pb	2·43	1·56	1·57	1·54	2·22	1·26	1·51	1·69	1·24	0·891
Th	3·39	2·38	2·78	3·15	3·13	1·55	1·54	1·6	0·983	1·04
U	0·694	0·505	0·57	0·633	0·657	0·351	0·376	0·37	0·225	0·26
Sr*	1·01	1·11	1·1	0·97	0·916	1·22	1·27	1·23	1·35	1
Fe/Mn[1]	74·3	75·9	72·8	66·3	82·1	88·9	74	88·5	81·6	78·4
Fe/Mn[2]	74·9	76·9	73·5	67·7	82·3	89·5	74·6	89·4	81·9	78·7
Fe/Mn[3]	78·9	79·5	79·1	74·4	86·2	93·4	82·2	92·7	85·3	86·1
Zr/Hf	40·6	36	39·2	38·2	38·3	36	37·7	38·6	35·3	35·5
Nb/Ta	17·2	16·1	16·7	16·7	16	15·3	16	16·8	15·9	16·1
Lu/Hf	0·066	0·069	0·069	0·069	0·063	0·067	0·064	0·066	0·077	0·079
Sm/Nd	0·229	0·264	0·248	0·235	0·238	0·276	0·273	0·278	0·293	0·293

(continued)

Table 3: Continued

Sample:	08HN-8A	08HN-9B	08HN-10A	08HN-10B	08HN-11A	08HN-12A	08HN-13A	08HN-14A	08HN-15A	08HN-16A
Sc	22·1	21	20	19·4	19·6	16·6	18·8	12·9	21·7	18·4
Ti	14138	9676	10869	11212	11086	11331	10084	10181	9799	11716
V	170	140	144	151	145	131	128	99·6	143	133
Cr	248	159	206	217	204	202	267	178	190	173
Mn	1487	1074	990	1033	1047	836	1035	881	1145	922
Co	58·7	42·9	42	41·7	41	44·1	46	35·8	45·5	41·5
Ni	165	111	156	156	138	144	166	116	130	144
Cu	47·9	45	55·8	57·2	53·3	54·9	52·6	33·1	62	55·5
Zn	128	111	111	111	106	118	118	140	114	128
Ga	20·6	19·4	19·3	19·1	19·2	20·6	21·5	27·4	20·3	20·7
Ge	1·59	1·6	1·58	1·56	1·53	1·3	1·41	1·32	1·61	1·38
Rb	22	7·23	13·9	13·9	17·2	20·2	20	35·3	8·38	17·4
Sr	558	198	433	348	373	525	532	672	293	416
Y	21·3	44·6	19·5	18·8	19·4	16·3	15·1	14·6	16·1	18·8
Zr	199	94	122	122	128	170	135	291	93·8	148
Nb	37·3	11·3	15·6	15·9	16·6	39·6	31·1	57·8	11·2	26·7
Ba	524	114	146	143	159	443	365	644	106	218
La	25·4	37·3	12·4	12·3	12·6	25·2	19·2	39·6	8·21	17·9
Ce	50·7	82·2	27·5	27	27·6	48·7	38·5	73·8	18·3	37·4
Pr	6·4	10·9	3·66	3·59	3·7	5·9	4·8	9·24	2·5	4·8
Nd	27·1	45·5	16·3	16	16·4	23·7	19·3	36	11·8	20·9
Sm	6·4	11·7	4·55	4·4	4·36	5·48	4·65	7·67	3·54	5·14
Eu	2·26	4·18	1·63	1·59	1·6	2	1·62	2·62	1·34	1·77
Gd	6·35	11·6	4·79	4·74	4·71	5·56	4·45	6·89	3·9	5·14
Tb	0·899	1·93	0·762	0·752	0·775	0·81	0·681	0·923	0·64	0·817
Dy	4·61	9·99	4·23	4·11	4·22	3·89	3·43	4·08	3·45	4·18
Ho	0·8	1·75	0·767	0·765	0·746	0·628	0·565	0·598	0·654	0·756
Er	1·86	4·12	1·88	1·93	1·88	1·46	1·38	1·3	1·66	1·78
Tm	0·234	0·557	0·257	0·255	0·247	0·177	0·173	0·155	0·222	0·234
Yb	1·36	3·12	1·45	1·47	1·48	1·02	0·989	0·794	1·24	1·34
Lu	0·191	0·425	0·212	0·211	0·207	0·141	0·135	0·112	0·186	0·195
Hf	4·98	2·64	3·17	3·32	3·46	4·08	3·51	6·97	2·57	3·7
Ta	2·24	0·714	0·955	1·01	1·04	2·44	1·85	3·77	0·709	1·68
Pb	0·316	1·17	2·08	2·2	2·05	2·09	1·27	3·37	1·26	2·37
Th	3·32	1·06	1·98	2·02	2·21	4·13	2·95	5·88	1·18	2·77
U	0·863	0·324	0·481	0·48	0·53	0·291	0·441	0·661	0·267	0·679
Sr*	1·11	0·238	1·5	1·23	1·29	1·14	1·43	0·959	1·47	1·09
Fe/Mn[1]	59·7		82	79·9	75·5	92·9	79·1	82·6		85·7
Fe/Mn[2]	59·8	83	82·8	80	76	94·6	79·1	82·5	75	85·4
Fe/Mn[3]	66·7	86·2	85·9	83·3	79·1	102	87·3	93	82·9	92·8
Zr/Hf	40·1	35·6	38·4	36·8	37	41·8	38·5	41·7	36·5	39·9
Nb/Ta	16·7	15·8	16·3	15·7	16	16·3	16·8	15·3	15·8	16
Lu/Hf	0·038	0·161	0·067	0·064	0·06	0·035	0·039	0·016	0·072	0·053
Sm/Nd	0·236	0·256	0·279	0·275	0·266	0·232	0·241	0·213	0·302	0·246

(continued)

Table 3: Continued

Sample:	08HN-16C	08HN-17B	08HN-18B	08HN-19A	08HN-19C	08HN-20A	08HN-21A	08HN-21B	08HN-21E	08HN-22A
Sc	14·6	9·48	21·5	19·5	19·1	18·7	18·6	18·5	15·6	19·7
Ti	12230	8998	9581	18937	17854	13910	11441	10999	12925	15235
V	135	86·1	134	194	177	159	152	140	147	200
Cr	171	116	181	229	220	217	197	197	304	277
Mn	941	728	1098	1325	1176	1118	1118	1086	1032	1170
Co	39·5	29·1	44·7	49·3	47·6	44·5	46	43·9	43·4	46·2
Ni	103	84	134	144	138	141	162	156	177	151
Cu	48·6	42·3	76·4	62·9	57	62	53	50·7	64·3	47
Zn	144	152	116	147	139	124	127	117	141	122
Ga	25·8	31·2	19·7	22·3	21·2	21·1	21·8	19·7	26·4	21·6
Ge	1·36	1·31	1·52	1·44	1·37	1·39	1·56	1·42	1·43	1·59
Rb	39·2	56·5	7·37	31·9	30·8	16·9	20·2	19·2	40·6	34·2
Sr	680	742	286	665	626	486	458	434	720	617
Y	16·1	14·1	14·8	26·8	28·5	26·2	18·1	17·8	17	22·3
Zr	275	440	91·5	257	243	172	141	138	293	213
Nb	55·6	79·8	12·1	48	46·2	28·7	25·7	24·6	58	41·9
Ba	533	711	111	636	616	220	215	208	583	492
La	33·5	49·6	8·54	33·3	33·7	18·3	16·5	16·3	36·3	30·8
Ce	66·6	92·6	18·7	69	67·3	37·3	34·4	33·5	71·5	62·3
Pr	7·99	10·6	2·49	8·96	8·84	4·97	4·44	4·27	8·62	7·76
Nd	31·3	38·7	11·2	38·1	37·3	22·1	19	18·1	33·3	30·8
Sm	6·75	7·88	3·26	8·82	8·57	5·76	4·84	4·58	7·26	6·76
Eu	2·28	2·57	1·26	2·8	2·85	2·12	1·68	1·72	2·42	2·22
Gd	5·99	6·78	3·69	8·36	8·56	6·09	4·9	4·76	6·45	6·53
Tb	0·84	0·9	0·597	1·22	1·24	0·935	0·748	0·724	0·914	0·955
Dy	3·98	3·84	3·3	6·01	6·1	4·83	3·98	3·78	4·28	4·8
Ho	0·611	0·545	0·606	1·05	1·02	0·84	0·686	0·658	0·662	0·831
Er	1·39	1·09	1·55	2·32	2·4	2·01	1·7	1·62	1·46	2·04
Tm	0·168	0·12	0·206	0·284	0·286	0·254	0·23	0·215	0·176	0·263
Yb	0·945	0·676	1·18	1·62	1·6	1·32	1·31	1·23	1·01	1·47
Lu	0·129	0·088	0·168	0·219	0·225	0·191	0·185	0·173	0·132	0·203
Hf	6·48	9·69	2·53	6·08	5·62	4·12	3·42	3·33	6·47	4·81
Ta	3·6	5·47	0·78	3·14	2·98	1·76	1·56	1·49	3·74	2·51
Pb	2·91	4·36	3·52	2·08	2·18	1	2·66	1·76	2·72	2·96
Th	5·44	8·63	1·25	4·59	4·34	2·28	2·61	2·42	5·28	4·61
U	1·31	1·53	0·259	1·04	0·974	0·617	0·687	0·635	1·27	0·965
Sr*	1·09	0·911	1·45	0·953	0·918	1·24	1·31	1·29	1·08	1·03
Fe/Mn^1	84		78·3	68·1	76·1		73·8		77·3	
Fe/Mn^2	83·7	86·8	78·8	68	76	76·2	73·7	77	78	71·6
Fe/Mn^3	90·3	90·3	88·9	73·3	82·6	82·2	83·9	86	87·3	79·1
Zr/Hf	42·5	45·4	36·2	42·2	43·2	41·6	41·2	41·4	45·3	44·3
Nb/Ta	15·4	14·6	15·6	15·3	15·5	16·3	16·5	16·4	15·5	16·7
Lu/Hf	0·02	0·009	0·067	0·036	0·04	0·046	0·054	0·052	0·02	0·042
Sm/Nd	0·215	0·204	0·29	0·231	0·23	0·261	0·254	0·254	0·218	0·219

(continued)

Table 3: Continued

Sample:	08HN-22D	08HN-23B	08HN-24A	08HN-24B	08HN-24D	08HN-25A	08HN-25C	08HN-26A	08HN-26C
Sc	24·5	20	25·6	25·5	25·2	18	20·1	21·8	21·5
Ti	16298	14422	15187	14818	14051	11846	12020	13034	13394
V	238	188	218	208	207	156	154	193	190
Cr	222	258	248	259	283	228	250	252	241
Mn	1401	1112	1290	1250	1227	1277	1123	1162	1135
Co	50·3	44·8	51·2	50·9	50·4	44·3	43·3	43·5	40·6
Ni	172	150	205	205	208	164	168	107	93·4
Cu	59·1	55	60·5	59·9	56·6	49·1	59·1	57·9	52·2
Zn	132	115	117	119	112	108	113	126	112
Ga	21·7	20·3	19·6	19·8	19·8	18·8	19·4	22·4	21
Ge	1·58	1·53	1·57	1·68	1·68	1·26	1·47	1·72	1·49
Rb	31·9	33·7	28·5	27·6	25·8	19·5	15·7	22·9	21·9
Sr	699	624	573	577	585	453	461	504	479
Y	25·3	22·4	22·2	21·2	20·9	18·5	19·3	21·1	20·4
Zr	256	212	205	186	179	143	146	170	165
Nb	63·4	43·6	46·5	44·2	42·2	25·8	24·5	26·6	26·9
Ba	505	502	426	407	404	217	223	236	245
La	47·2	31·5	33·5	28·9	28·4	16·8	17	19·5	19·7
Ce	96·5	64	69·2	60·7	58	35·9	36·3	42·1	41·3
Pr	11·5	7·82	8·48	7·48	7·08	4·54	4·67	5·38	5·34
Nd	43·3	31·7	32·8	29·4	28	19·4	19·6	21·9	22·3
Sm	8·1	6·9	6·72	6·03	5·97	4·61	4·82	5·34	5·44
Eu	2·54	2·19	2·04	1·95	1·93	1·58	1·66	1·82	1·91
Gd	7·35	6·31	5·97	5·69	5·46	4·75	4·64	5·26	5·45
Tb	1·03	0·944	0·854	0·844	0·821	0·737	0·709	0·798	0·828
Dy	5·24	4·81	4·52	4·46	4·22	3·89	3·93	4·27	4·32
Ho	0·939	0·829	0·81	0·775	0·769	0·708	0·696	0·764	0·742
Er	2·23	1·94	1·98	1·91	1·9	1·66	1·73	1·94	1·83
Tm	0·304	0·243	0·272	0·254	0·253	0·218	0·222	0·249	0·231
Yb	1·8	1·44	1·57	1·53	1·52	1·25	1·29	1·46	1·37
Lu	0·249	0·211	0·227	0·221	0·22	0·176	0·189	0·197	0·2
Hf	5·76	4·88	4·67	4·29	4·1	3·27	3·38	3·89	3·87
Ta	3·93	2·65	2·77	2·73	2·44	1·49	1·46	1·58	1·67
Pb	4·15	3·55	2·84	2·54	2·21	1·54	1·67	2·14	2·6
Th	5·81	4·65	4·31	3·96	3·67	2·31	2·32	2·82	2·89
U	1·38	1·04	1·01	0·954	0·916	0·549	0·476	0·66	0·689
Sr*	0·795	1·02	0·883	1	1·07	1·26	1·27	1·22	1·16
Fe/Mn^1	66·4		67·2	70·5		67·9	77·8	69·9	70·9
Fe/Mn^2	66·1	75·5	66·9	70·4	70·2	67·9	77·8	69·7	70·7
Fe/Mn^3	74·2	78·5	77·2	77·4	76·6	75·2	81·8	81·2	80·5
Zr/Hf	44·5	43·4	43·9	43·3	43·6	43·7	43·1	43·8	42·7
Nb/Ta	16·1	16·5	16·8	16·2	17·3	17·3	16·8	16·8	16·1
Lu/Hf	0·043	0·043	0·049	0·052	0·054	0·054	0·056	0·051	0·052
Sm/Nd	0·187	0·218	0·205	0·206	0·213	0·238	0·246	0·243	0·244

(continued)

Table 3: Continued

Sample:	ZK03-24.4	ZK03-29.1	ZK04-26.8	ZK05-20.1	ZK05-36.5	ZK05-25.4
Sc	16·2	16·6	21·1	21·6	23·5	20·7
Ti	14936	15734	10905	10579	11723	11276
V	150	152	138	143	154	144
Cr	131	114	214	226	282	199
Mn	1564	1504	1512	974	2324	1032
Co	42·9	44	37·7	44	47	41·4
Ni	129	115	90·3	173	174	160
Cu	51·8	49·7	67·7	61·7	69	65·4
Zn	161	160	120	108	134	110
Ga	22·5	22·4	18·4	18·2	19·5	18·3
Ge	1·68	1·73	1·54	1·56	1·54	1·47
Rb	55·4	35·6	16·5	3·2	4·8	5·32
Sr	1327	1341	439	372	349	397
Y	33·2	34·7	19·5	18	20	19·1
Zr	361	360	117	110	123	121
Nb	122	118	20·2	21·5	25·5	25·4
Ba	858	916	224	202	194	182
La	97·2	100	16·6	16	19	18·5
Ce	175	180	31·9	31·4	37	35·8
Pr	19·7	20·5	3·98	3·83	4·61	4·39
Nd	72·2	77·1	16·8	16·1	18·9	18·1
Sm	13	14·1	4·52	4·05	4·53	4·48
Eu	4·12	4·48	1·63	1·55	1·64	1·62
Gd	11·9	12·3	4·92	4·58	4·98	4·81
Tb	1·54	1·52	0·763	0·721	0·775	0·749
Dy	7·66	7·63	4·2	3·94	4·32	4·34
Ho	1·29	1·28	0·766	0·728	0·785	0·752
Er	3·09	3·03	1·89	1·84	1·93	1·87
Tm	0·389	0·377	0·242	0·234	0·261	0·238
Yb	2·24	2·27	1·54	1·46	1·57	1·49
Lu	0·309	0·311	0·221	0·21	0·225	0·207
Hf	8·55	8·48	3·39	3·18	3·52	3·37
Ta	12·3	12	1·21	1·25	1·54	1·45
Pb	5·73	5·58	1·89	1·64	2·60	2·01
Th	13·4	12·9	2·56	2·46	2·77	2·8
U	2·53	3·01	0·541	0·529	0·461	0·581
Sr*	0·868	0·836	1·39	1·22	0·94	1·15
Fe/Mn^1	59·9	61·4	45·8	83·3	38	80
Fe/Mn^2	61·1	63	47·9	84·8	38	81·8
Fe/Mn^3	64·4	66·8	50	88·8	41	87·4
Zr/Hf	42·2	42·4	34·5	34·6	35·2	36·1
Nb/Ta	9·95	9·84	16·7	17·2	16·5	17·6
Lu/Hf	0·036	0·037	0·065	0·066	0·064	0·062
Sm/Nd	0·18	0·183	0·269	0·251	0·240	0·248

Sr anomaly is given by $Sr^* = Sr_N/(Ce_N \times Nd_N)^{0·5}$, where N denotes primitive mantle-normalized values. Fe/Mn^1 was directly determined by ICP-AES. Fe/Mn^2 was calculated using XRF-determined Fe and ICP-MS-determined Mn contents. Fe/Mn^3 was calculated using XRF-determined Fe and Mn contents.

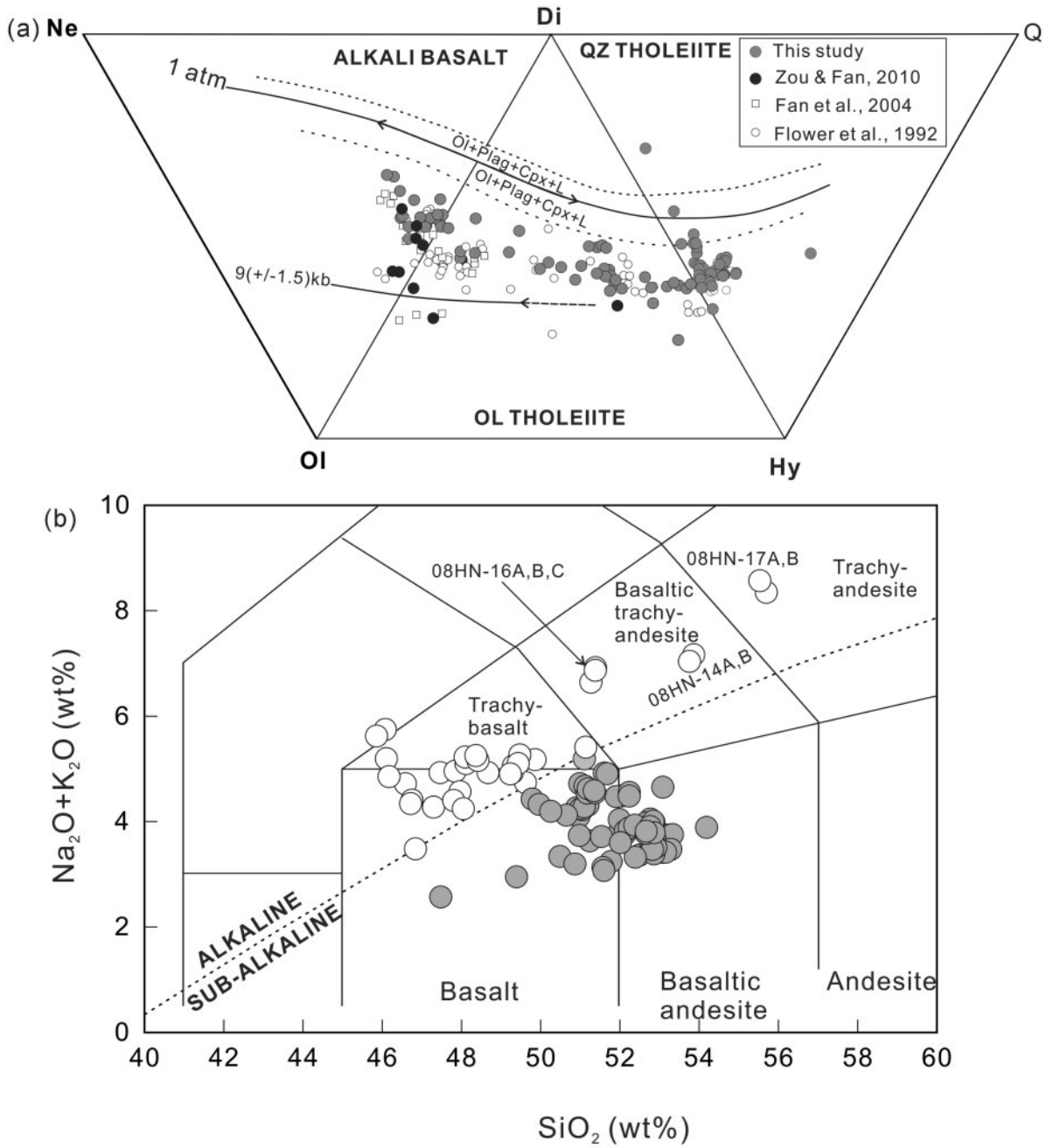

Fig. 3. (a) CIPW normative compositions of the Hainan basalts. Norms were calculated assuming $Fe^{2+}/Fe_{total} = 0{\cdot}9$. The 1 atm and 9 (±1·5) kbar cotectics are from Thompson (1983) and Thompson *et al.* (2001). Arrows point in the direction of decreasing temperature. (b) Total alkalis vs SiO_2 diagram (Middlemost, 1994) for the classification of the Hainan basalts.

Fe/Mn ratios. Therefore, the high Fe/Mn ratios may reflect the effects of melting processes and mantle source heterogeneity.

All the studied samples show typical OIB-like chondrite-normalized rare earth element (REE) patterns with enrichments in light rare earth elements (LREE) over HREE (Fig. 7a and b). The LREE enrichment increases systematically from subalkaline series to alkaline series basalts (Fig. 7a and b). A silica-oversaturated sample (08HN-17B) displays a strong depletion in HREE and Lu with Tb/Yb = 6·0 and Lu/Hf = 0·009. Compared with typical MORB and alkalic OIB (Fig. 7a), all studied samples are strongly depleted in HREE.

In the primitive mantle-normalized multi-element patterns, except for four drill samples (ZK05-25.4, ZK05-36.5, ZK03-24.4, and ZK03-29.1), all samples show

appreciable enrichment in high field strength elements (HFSE), such as Nb and Ta. The most prominent feature of the trace element patterns of studied samples is the small but significant positive Sr anomalies (Fig. 7c and d). The four drill samples (ZK03-24.4, ZK03-29.1, ZK05-36.5, and ZK05-29.1) show strong depletion in K_2O (Fig. 7c and d). The alkalic basalts display negative Ti and Th–U anomalies, whereas the tholeiites show no significant depletion in Ti and Th–U. Such patterns are comparable with those of intra-plate basalts, such as OIB (Sun & McDonough, 1989).

Mineral compositions

Olivine

We analyzed the compositions of 41 olivines with euhedral textures, 41 with subhedral–undeformed textures, and 19 with deformed textures (Table 4). In addition, we analyzed 125 unclassified olivine phenocrysts (data given in Supplementary Data Electronic Appendix Table R1, available for downloading at http://www.petrology.oxfordjournals.org). The olivines have a wide range of Fo contents [Fo = 100 × Mg/(Mg + Fe), cation ratio] varying from 55·2 to 91·9. Phenocrystic olivines have Fo contents of up to 90·7. Their CaO contents are all within the range of phenocrysts precipitated from basalt–picrite magmas, but are much higher than those of mantle xenoliths (CaO <0·1 wt %; Thompson & Gibson, 2000; Ren *et al.*, 2004) (Fig. 8a). MnO contents are negatively correlated with Fo (Fig. 8b). NiO decreases with decreasing Fo content, which differs from the mantle olivine array (e.g. Sato, 1977) (Fig. 8c). The average contents of minor elements in olivines with Fo ≥85 are: CaO = 0·18 wt % (±0·07%, 2σ), NiO = 0·36 wt % (±0·05%, 2σ), MnO = 0·16 wt % (±0·03%, 2σ).

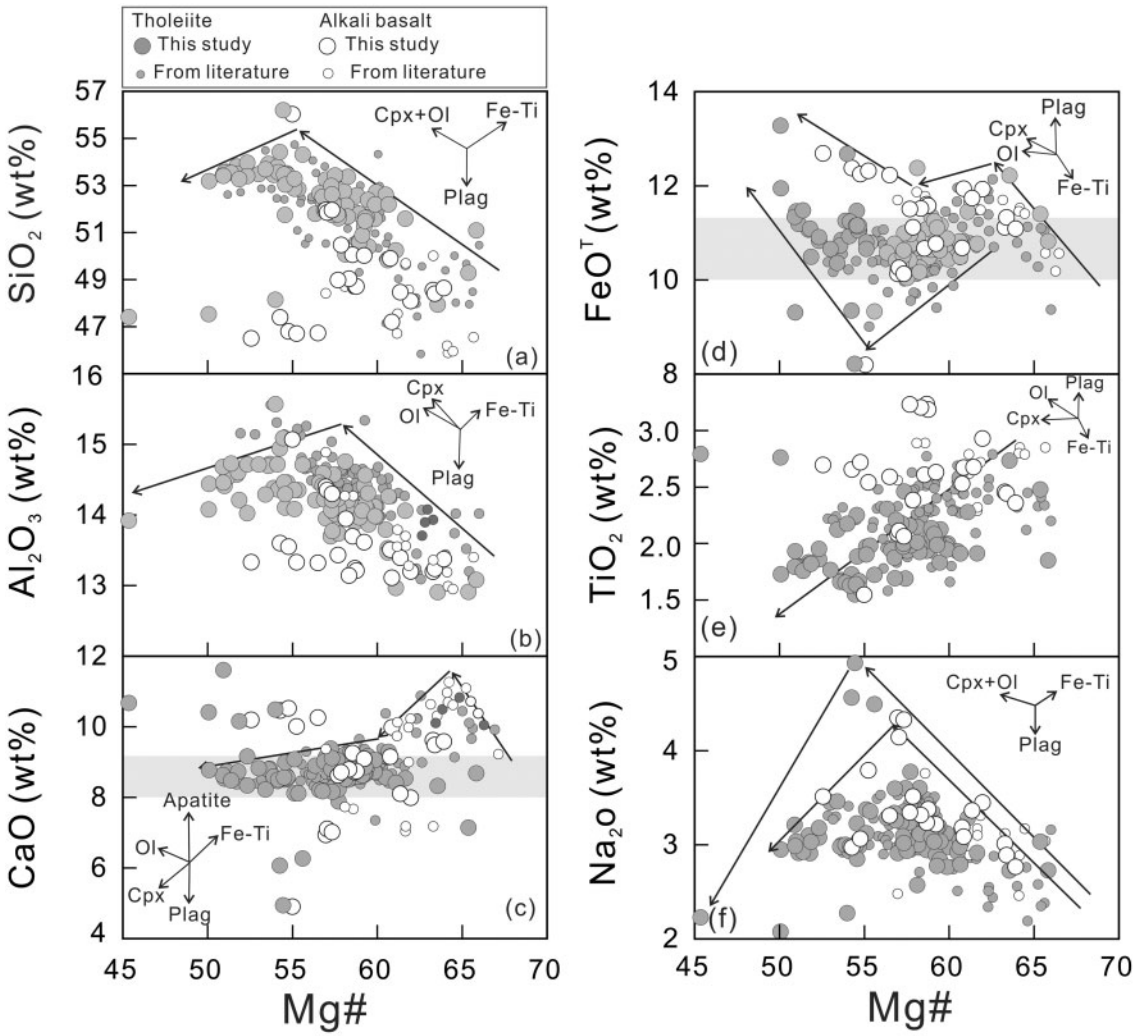

Fig. 4. Variations of selected oxides, trace element and element ratios in the Hainan basalts as functions of Mg#. Mg# = 100 × Mg/(Mg + Fe), $Fe^{2+}/Fe_{total} = 0.90$, cation ratio. Large circles represent data from this study, and small circles are data from the literature (Flower *et al.*, 1992; Fan *et al.*, 2004; Zou & Fan, 2010). The grey bands indicate the range of *y*-axis values for most tholeiites.

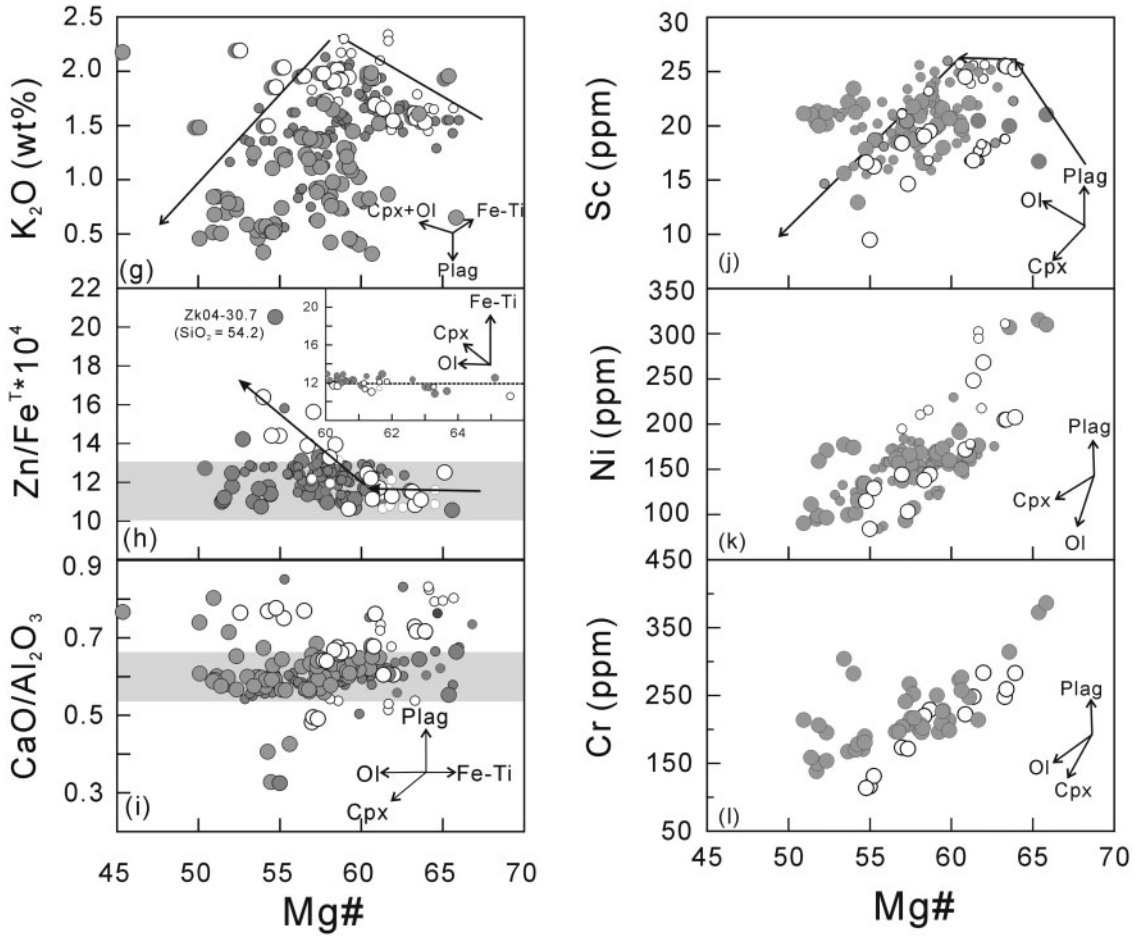

Fig. 4. Continued.

Xenocrystic olivines may be discriminated from phenocrystic olivines by their physical characteristics including deformation banding (e.g. kink bands), resorption, and small grain sizes (<2 mm) (e.g. Garcia, 1996). Kink bands have been identified in samples 08HN-1A and 08HN-4D. This kind of deformed olivine is characterized by low CaO (<0·1 wt %), MnO (<0·14 wt %) and FeO (<10 wt %), and high MgO (>46 wt %), which suggests that they were probably derived from disaggregated peridotite xenoliths.

Figure 9a shows results of the single microprobe analyses as functions of the Mg# of the host basalts. We calculated the whole-rock Mg# with 10% of total Fe as Fe^{3+}. The Fe–Mg exchange partition coefficient between olivine and basaltic liquid is well constrained by experiments, varying from 0·3 at 1 atm in equilibrium with a basaltic melt with about 8 wt % MgO (Roeder & Emslie, 1970) to 0·31–0·34 at 5–15 kbar (Ulmer, 1989). Olivine–melt equilibrium relations of this kind are best shown in a plot of whole-rock Mg# versus the forsterite content of olivine (Fo) (e.g. Garcia, 1996). As shown in Fig. 9a, the bold curves indicate the theoretical range of olivine compositions that would be in equilibrium with a given melt composition. Horizontal arrows in Fig. 9a indicate the effect of crystal accumulation. Only two compositions of olivine cores in samples 08HN-8A and 16A fall within or near the equilibrium field. Olivine core compositions for samples 08HN-14B, 17A, and 19C fall significantly below the equilibrium field, suggesting that the analysed olivines are not equilibrium phenocrysts, but late-crystallizing groundmass grains. The remaining five samples (08HN-1A, 2B, 4D, 24B, and 25A) contain three populations of olivines including an Mg-rich group, an Mg-depleted group, and an equilibrium group, which plot respectively above, within, and below the equilibrium field. The Mg-rich group can be divided into xenocrystic and phenocrystic olivines. All xenocrystic olivines from 08HN-1A, 2B, and 4D, recognized by their physical characteristics, are much more Mg-rich and plot significantly higher in the equilibrium field. The Mg-rich phenocrystic olivines (08HN-1A, 2B,

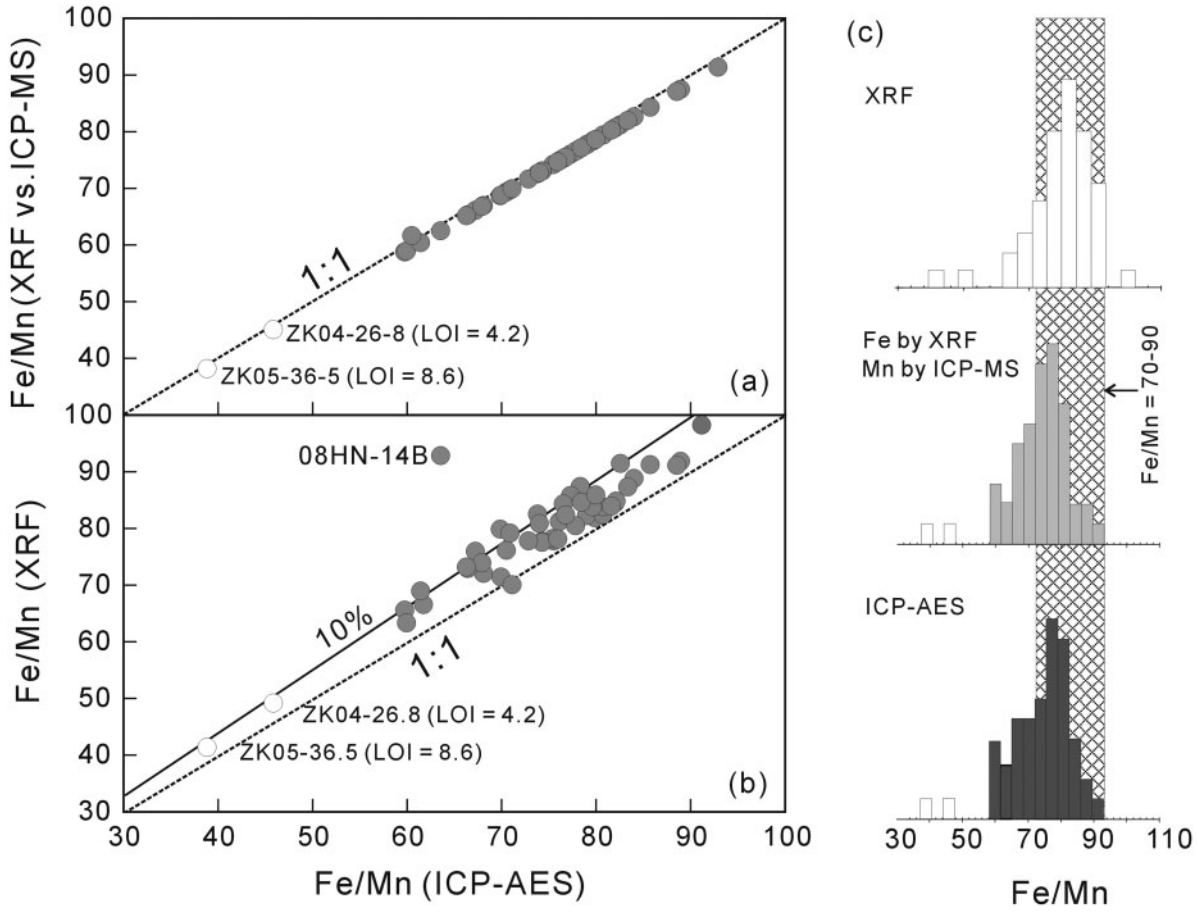

Fig. 5. Comparison of Fe/Mn ratios determined by IPC-AES with (a) Fe/Mn[1] (Fe determined by XRF and Mn by ICP-MS) and (b) Fe/Mn[2] (both Fe and Mn measured by XRF). (c) Fe/Mn histograms showing that there is no systematic difference between datasets acquired using the XRF, ICP-MS and ICP-AES methods.

24B, and 25A) also plot above the equilibrium field. These Mg-rich olivines probably crystallized earlier from hotter, higher-MgO melts and were entrained in the ascending magma. The Mg-rich phenocrystic olivines have Fo contents ranging from 89·6 to 90·7, which suggest Mg# values of 72–75 for the equilibrium melts using a $K_D = 0{\cdot}3$. Such Mg# values indicate that the equilibrium melts should have ~16 wt % MgO based on the correlations of Mg# vs MgO in the Hainan basalts.

Clinopyroxene

The chemical compositions of analyzed clinopyroxenes (Cpx) are presented in Table 5. Cations were calculated on a six-oxygen basis following the procedure of Lindsley (1983) and ferric iron was calculated from charge-balance considerations. Interestingly, although large compositional variations in single samples exist (Table 5), all the analyses in cores and rims fall in the diopside to Mg-augite field in terms of En–Fs–Wo nomenclature with an end-member composition of $En_{24{\cdot}3-47{\cdot}3}Fs_{38{\cdot}3-1{\cdot}6}Wo_{37{\cdot}4-51{\cdot}1}$ (Fig. 10a). All the analyzed clinopyroxenes plot within the Ca–Mg–Fe pyroxene (Quad area) field in the Q–J diagram (Fig. 10b) where $Q = Ca + Mg + Fe^{2+}$, and $J = 2Na$. Some clinopyroxenes contain a high proportion of calculated jadeite (up to 14·4%).

The Fe–Mg exchange partition coefficient between clinopyroxene and basaltic melts is less well constrained than that for olivine–melt, principally because of the presence of ferric iron in clinopyroxene and in the melt (Putirka *et al.*, 2003; Putirka, 2008). The Fe–Mg K_D is slightly dependent on pressure, and probably falls between $0{\cdot}27 \pm 0{\cdot}05$ (Putirka, 1999) and $0{\cdot}23 \pm 0{\cdot}05$ (Toplis & Carroll, 1995). Figure 9b shows the relationship between Cpx Mg# and whole-rock Mg# using an Fe–Mg K_D of 0·23, 0·25, and 0·27. Four samples (e.g. 08HN-2A, 2A, 16A and 17A) contain equilibrium composition clinopyroxenes. However, three samples (08HN-1A, 2A and 2B) contain phenocrysts that are too Mg-rich to be considered as equilibrium compositions. High-Mg clinopyroxenes can

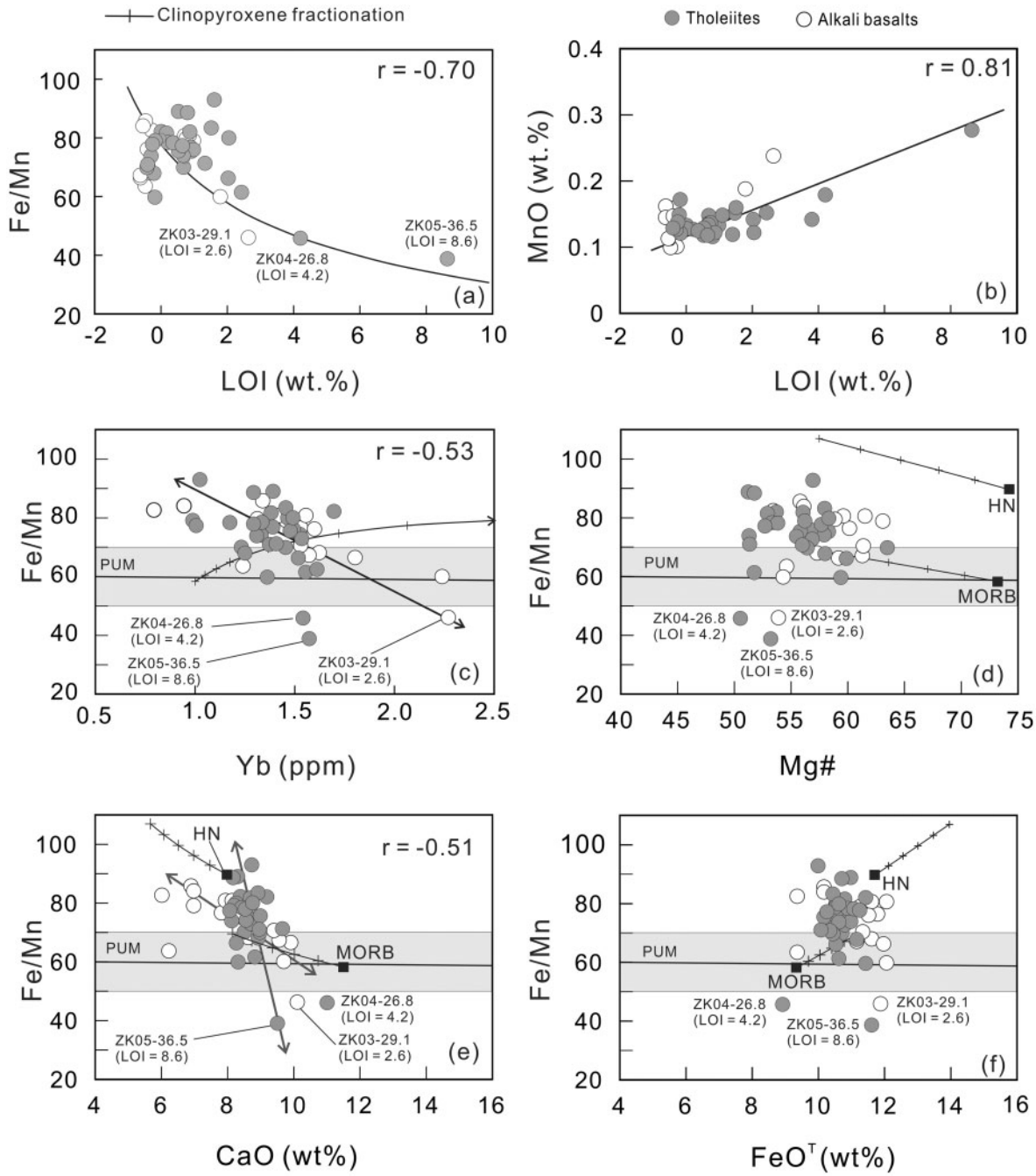

Fig. 6. (a, b) Variation of Fe/Mn ratios and MnO contents with LOI values. (c–f) Variation of Fe/Mn determined by ICP-AES with Yb, Mg#, CaO and FeO^T. Calculated Cpx crystal fractionation trends for a MORB-like basalt (MORB) and the average of the estimated primary melts for the Hainan basalts (HN) are indicated. Because olivine fractionation would decrease the Fe/Mn ratio of the melt, only cpx was taken into account for evaluating the contribution of crystal fractionation to the high Fe/Mn ratios in the basalts. Parameters used in calculations are from Liu *et al.* (2008). A global suite of mantle peridotites (primitive upper mantle, PUM) yielded Fe/Mn = 60 ± 10 (1σ) (McDonough & Sun, 1995) and is highlighted by the horizontal grey bands. Each cross on the model curves represents a 10% increment of fractional crystallization.

crystallize at high pressure from less evolved magmas with high Al/Ti and Na/Ti ratios (e.g. Damasceno *et al.*, 2002). Clinopyroxenes in samples 08HN-4B, 8A and 19C are characterized by low Mg#, all plotting below the equilibrium field. Sample 08HN-1A contains two populations of clinopyroxenes—an Mg-rich group that plots significantly above the equilibrium field and an Mg-depleted group that plots below the equilibrium field.

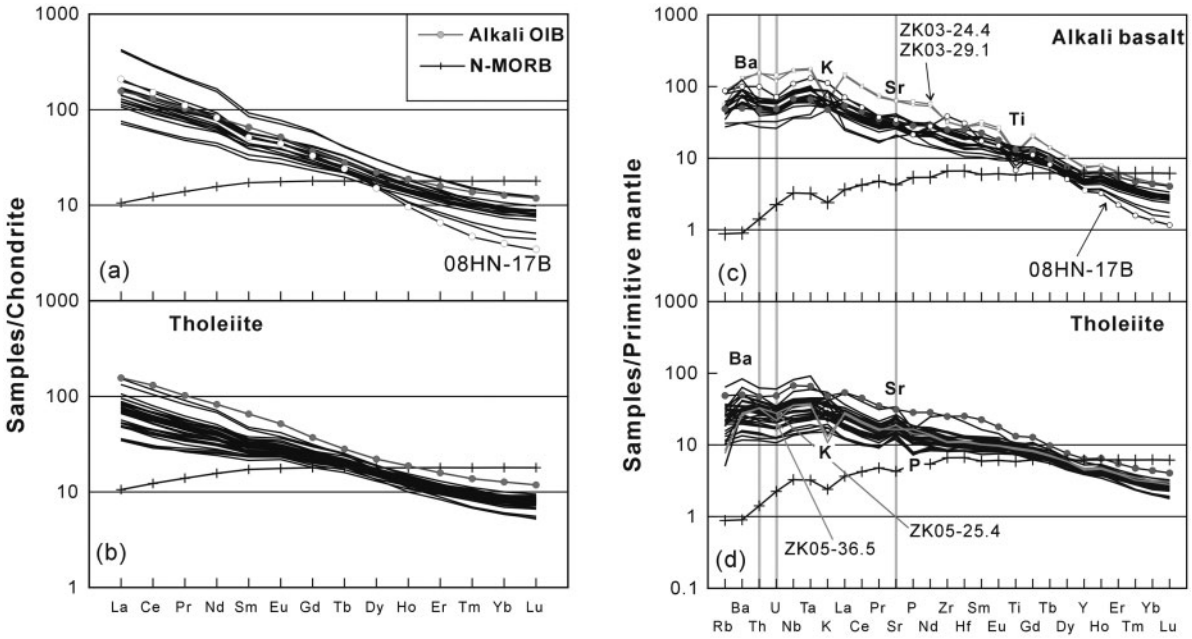

Fig. 7. (a, b) Chondrite-normalized REE patterns for the Hainan basalts: (a) alkali basalts; (b) subalkaline (tholeiitic) basalts. (c, d) Primitive mantle-normalized incompatible trace element patterns: (c) alkali basalts; (d) tholeiites. Normalization values are from Sun & McDonough (1989).

The Mg# values [100Mg/(Mg + Fe^{2+}), cations] vary from 91·3 to 61·2; reverse zoning is never observed. The Mg# values correlate moderately positively with Al_2O_3/TiO_2 ($r = 0{\cdot}51$), Na_2O/TiO_2 ($r = 0{\cdot}48$), and Al^{6+}/Al^{4+} ($r = 0{\cdot}52$), suggesting that the high Mg# clinopyroxenes are the result of high-pressure crystallization (e.g. Damasceno *et al.*, 2002). These clinopyroxenes are characterized by high Al contents (up to 10·7 wt %). The Cr_2O_3 contents in the clinopyroxenes decrease rapidly from ~0·8 at an Mg# of 80 to 0–0·3 wt % at an Mg# of 75 (Fig. 11a). MnO contents correlate negatively with Mg# (Fig. 11d). TiO_2, Na_2O, CaO, and SiO_2 do not systematically correlate with Mg# and show curves or kinks on the trends of Mg#–*X* (Fig. 11).

DISCUSSION

Multiphase and polybaric crystallization and fractionation

At the outset of this discussion, it is necessary to establish what dominant process was responsible for the large range of chemical variations in the studied samples, including the variation of MgO between 2 and 11 wt % and the equally wide ranges of Ni (315–83 ppm) and Cr (387–114 ppm) contents (Table 3). Although both mantle melting and fractional crystallization processes could cause such variations in Mg-rich basalts, the depletions of MgO, Ni and Cr in the basalts requires fractional crystallization from more magnesian parent magmas to be the main factor in their genesis. The strong positive Mg#–Ni–Cr correlations (Fig. 4k and l) also suggest fractional crystallization of olivine from the bulk-rock samples. This is consistent with the correlated Fo–NiO–MnO–CaO variations in olivine phenocryst compositions (Fig. 8). However, the high-Mg olivine phenocrysts (Fo ≥ 89) are not in equilibrium with the whole-rock compositions of the host basalts (Fig. 9a). This implies that the high-Mg olivine phenocrysts may have crystallized from early high-magnesian melts, whereas the low-Mg phenocrysts are probably in equilibrium with the host melt prior to or during eruption.

Except for a few samples, the tholeiites have similar FeO^T, CaO, and CaO/Al_2O_3 contents (highlighted by the grey band in Fig. 4c, d, and i). This implies that clinopyroxene is not a predominant phase in the fractionating mineral assemblage. Clinopyroxene fractionation can significantly increase the Zn/Fe ratios in the remaining melt because $D_{Zn/Fe}$ for olivine/melt is nearly unity, but much less than unity between clinopyroxene and melt (Le Roux *et al.*, 2010). Except for three samples, all the tholeiite samples are characterized by a narrow range of Zn/Fe ratios ($Zn/Fe \times 10^4 = 10–13$; Fig. 4h) over a large range of Mg# (65–50). This implies that the effect of clinopyroxene fractionation on the composition of the tholeiites is insignificant. In contrast, the alkali basalt samples define a highly negative correlation of Zn/Fe with Mg# at Mg# <61, indicating that clinopyroxene fractionation strongly affected the compositions of the alkali basalts at Mg# <61.

Table 4: Microprobe analyses of euhedral, subhedral–undeformed, and deformed olivines from the Hainan basalts

Probe no.	SiO_2	MgO	FeO	MnO	CaO	NiO	Fo	Total
Deformed olivine								
08HN-1A-1	41·57	49·19	8·92	0·14	0·07	0·44	90·8	100·32
08HN-1A-2	40·48	49·04	8·93	0·11	0·07	0·42	90·7	99·05
08HN-1A-3	39·50	46·68	9·98	0·12	0·08	0·40	89·3	96·75
08HN-1A-4	39·61	48·27	9·07	0·16	0·08	0·39	90·5	97·58
08HN-1A-5	41·78	48·77	8·89	0·11	0·05	0·44	90·7	100·05
08HN-4D-1	40·20	50·52	7·92	0·08	0·02	0·24	91·9	98·98
08HN-4D-2	40·52	50·78	8·98	0·08	0·05	0·25	91·0	100·66
08HN-2B-19	40·48	46·97	10·87	0·18	0·09	0·37	88·5	98·95
08HN-2B-20	41·65	48·18	9·42	0·16	0·10	0·42	90·1	99·93
08HN-2B-21	40·71	44·73	14·03	0·24	0·06	0·29	85·0	100·07
08HN-2B-22C	40·23	44·47	14·11	0·22	0·04	0·33	84·9	99·40
08HN-2B-22M	38·74	43·67	15·88	0·26	0·11	0·28	83·1	98·93
08HN-14B-22C	37·85	32·45	28·03	0·35	0·25	0·11	67·4	99·04
08HN-14B-24R	37·10	32·11	29·67	0·37	0·25	0·14	65·9	99·64
08HN-14B-12C	37·84	32·33	29·02	0·37	0·36	0·11	66·5	100·03
08HN-14B-12R	38·24	31·54	29·91	0·33	0·28	0·13	65·3	100·44
08HN-24B-29	39·64	45·20	14·10	0·20	0·22	0·28	85·1	99·65
08HN-24B-30	38·09	41·75	19·10	0·30	0·28	0·23	79·6	99·75
08HN-24B-31	38·46	44·13	16·91	0·22	0·32	0·16	82·3	100·20
08HN-24B-32	36·66	39·76	21·98	0·32	0·28	0·22	76·3	99·21
Subhedral–undeformed olivine								
08HN-1A-6	41·43	47·28	9·72	0·17	0·18	0·40	89·7	99·18
08HN-1A-7	41·47	47·56	9·67	0·12	0·21	0·44	89·8	99·47
08HN-1A-11	41·53	48·90	8·75	0·13	0·18	0·40	90·9	99·89
08HN-1A-12	41·39	48·72	8·76	0·17	0·15	0·38	90·8	99·55
08HN-2B-1	41·72	48·49	9·65	0·12	0·18	0·39	90·0	100·54
08HN-2B-2	41·72	48·52	9·88	0·18	0·18	0·35	89·7	100·83
08HN-2B-3	41·34	47·77	11·27	0·18	0·22	0·32	88·3	101·09
08HN-2B-4	41·50	48·04	9·48	0·14	0·20	0·40	90·0	99·76
08HN-2B-5	40·89	45·91	12·28	0·17	0·23	0·43	87·0	99·91
08HN-2B-6	40·97	46·95	11·65	0·17	0·07	0·38	87·8	100·19
08HN-2B-7	40·97	46·86	11·67	0·16	0·20	0·37	87·7	100·23
08HN-2B-8	41·66	48·09	9·90	0·13	0·08	0·32	89·7	100·17
08HN-2B-9	41·23	48·53	9·94	0·12	0·08	0·39	89·7	100·29
08HN-2B-10	40·69	47·95	9·93	0·14	0·21	0·35	89·6	99·28
08HN-2B-11	41·46	48·38	9·71	0·15	0·10	0·38	89·9	100·17
08HN-2B-12	40·13	49·08	9·70	0·12	0·16	0·37	90·0	99·56
08HN-2B-13	41·64	47·64	9·43	0·11	0·08	0·40	90·0	99·29
08HN-2B-14	39·97	43·56	16·68	0·28	0·21	0·19	82·3	100·89
08HN-2B-15	39·21	39·38	21·33	0·33	0·27	0·19	76·7	100·71
08HN-2B-16	39·12	39·27	21·29	0·35	0·24	0·20	76·7	100·47
08HN-2B-17	41·25	48·67	9·37	0·16	0·13	0·37	90·3	99·95
08HN-2B-18C	41·68	48·27	9·99	0·13	0·19	0·38	89·6	100·64
08HN-2B-18R	40·50	42·44	16·32	0·30	0·14	0·26	82·3	99·96
08HN-14B-1	32·92	37·92	29·28	0·32	0·21	0·10	69·8	100·75
08HN-14B-2	38·67	36·35	24·88	0·38	0·30	0·10	72·3	100·68
08HN-14B-4	32·94	36·80	29·11	0·40	0·38	0·12	69·3	99·73
08HN-14B-5	33·25	35·64	29·20	0·39	0·38	0·11	68·5	98·98
08HN-14B-6	33·41	37·09	29·45	0·38	0·36	0·06	69·2	100·74
08HN-2B-27	41·43	47·93	9·94	0·13	0·20	0·42	89·6	100·05
08HN-2B-28	41·49	48·47	10·04	0·11	0·18	0·33	89·6	100·62
08HN-2B-29	41·38	47·85	9·92	0·14	0·05	0·43	89·6	99·77
08HN-2B-30	40·25	43·26	16·64	0·22	0·15	0·25	82·3	100·77
08HN-2B-31	41·35	47·75	10·39	0·14	0·21	0·35	89·1	100·18
08HN-4D-3	40·35	43·00	14·12	0·22	0·32	0·24	84·4	98·25
08HN-4D-4	40·12	43·76	16·23	0·19	0·15	0·30	82·8	100·75
08HN-24B-34-R	39·46	46·93	13·50	0·18	0·22	0·28	86·1	100·58
08HN-24B-34-M	39·29	46·05	13·03	0·17	0·21	0·27	86·3	99·02
08HN-24B-34-C	39·42	46·97	12·99	0·19	0·27	0·31	86·6	100·16
Euhedral olivine								
08HN-1A-8	40·60	48·26	8·78	0·14	0·15	0·38	90·7	98·31
08HN-1A-9	41·55	47·10	9·76	0·11	0·21	0·38	89·6	99·10
08HN-1A-10	40·19	43·44	15·31	0·12	0·28	0·3	83·5	99·64
08HN-1A-11	39·92	42·36	16·57	0·34	0·23	0·16	82·0	99·58
08HN-1A-12	39·78	44·53	13·86	0·11	0·33	0·36	85·1	98·97
08HN-1A-13	39·49	45·28	14·19	0·34	0·16	0·35	85·0	99·81
08HN-1A-14	39·04	44·66	14·36	0·24	0·21	0·27	84·7	98·78
08HN-1A-10	40·84	48·74	9·11	0·10	0·23	0·41	90·5	99·43
08HN-2B-23	38·58	34·50	26·65	0·53	0·35	0·06	69·8	100·67
08HN-2B-24C	40·26	48·74	10·21	0·17	0·06	0·41	89·5	99·85
08HN-2B-24R	40·33	41·21	17·76	0·31	0·11	0·30	80·5	100·01
08HN-2B-25	40·45	47·07	10·87	0·15	0·28	0·41	88·5	99·23
08HN-2B-26C	40·62	49·30	9·18	0·14	0·05	0·37	90·5	99·64
08HN-2B-26R	39·40	42·62	16·31	0·33	0·14	0·28	82·3	99·08
08HN-16A-1	39·51	41·87	17·87	0·25	0·45	0·18	80·7	100·13
08HN-16A-2	39·27	40·57	19·78	0·25	0·22	0·22	78·5	100·31
08HN-24B-1	40·64	45·23	13·98	0·19	0·22	0·26	85·2	100·52
08HN-24B-2	40·45	43·49	15·73	0·25	0·25	0·23	83·1	100·40
08HN-24B-3	40·12	42·55	16·60	0·20	0·25	0·30	82·0	100·02
08HN-24B-4	40·84	44·66	13·84	0·22	0·27	0·26	85·2	100·10

(continued)

(continued)

Table 4: Continued

Probe no.	SiO_2	MgO	FeO	MnO	CaO	NiO	Fo	Total
08HN-24B-5	38·56	34·87	25·74	0·38	0·25	0·18	70·7	99·99
08HN-24B-6	41·29	44·82	13·64	0·17	0·24	0·29	85·4	100·45
08HN-24B-7	39·94	44·30	14·29	0·21	0·21	0·24	84·7	99·18
08HN-24B-8	40·02	44·62	14·03	0·20	0·27	0·32	85·0	99·46
08HN-24B-11	38·14	35·22	25·36	0·35	0·39	0·15	71·2	99·62
08HN-24B-12	39·46	46·22	14·03	0·17	0·26	0·25	85·4	100·39
08HN-24B-13	37·78	36·33	24·58	0·34	0·23	0·20	72·5	99·46
08HN-24B-18	39·88	44·59	13·78	0·22	0·23	0·30	85·2	98·99
08HN-24B-19	39·41	38·06	22·75	0·29	0·25	0·18	74·9	100·94
08HN-24B-20	39·79	39·61	20·79	0·27	0·23	0·14	77·3	100·83
08HN-24B-21	38·84	35·84	25·42	0·35	0·30	0·12	71·5	100·87
08HN-24B-22	37·96	33·18	28·54	0·46	0·32	0·15	67·5	100·60
08HN-24B-23	38·06	35·40	26·04	0·37	0·26	0·17	70·8	100·29
08HN-24B-24	38·37	36·22	24·89	0·38	0·29	0·14	72·2	100·29
08HN-24B-26	40·52	44·73	14·00	0·16	0·24	0·27	85·1	99·92
08HN-24B-27	40·47	44·83	14·07	0·21	0·26	0·32	85·0	100·15
08HN-24B-28	39·22	41·39	18·48	0·25	0·27	0·22	80·0	99·83
08HN-14B-11	37·74	31·13	30·82	0·34	0·26	0·17	64·3	100·45
08HN-14B-13	37·59	32·06	29·93	0·32	0·26	0·14	65·6	100·30
08HN-14B-15	38·79	33·15	27·65	0·30	0·27	0·11	68·1	100·29
08HN-14B-16	37·77	32·78	28·77	0·35	0·22	0·17	67·0	100·06
08HN-14B-17	37·83	31·75	29·84	0·34	0·25	0·09	65·5	100·10
08HN-14B-18	37·67	32·40	29·49	0·30	0·25	0·08	66·2	100·18
08HN-14B-19	37·67	32·51	29·51	0·36	0·25	0·10	66·3	100·39
08HN-14B-20	37·39	32·44	29·50	0·36	0·27	0·09	66·2	100·05
08HN-14B-26	36·82	30·55	31·10	0·38	0·27	0·11	63·6	99·23
08HN-14B-33	37·88	32·33	29·16	0·34	0·27	0·13	66·4	100·11
08HN-14B-35	37·93	32·50	28·65	0·33	0·27	0·13	66·9	99·81
08HN-14B-36	37·16	31·71	30·19	0·36	0·23	0·17	65·2	99·82

C, M and R after probe numbers indicate core, mantle and rim of Ol phenocrysts, respectively.

However, high Mg# (>61) alkali basalts have nearly constant Zn/Fe ratios, similar to the tholeiites (Fig. 4h). This implies a negligible effect of clinopyroxenes fractionation on the compositions of high Mg# alkali basalts.

The kinks in the trends of SiO_2, Al_2O_3, Na_2O, and K_2O with Mg# (Fig. 4a, b, f, and i) imply that plagioclase began to crystallize at Mg# = 58, following crystallization of olivine + clinopyroxene. Extensive removal of plagioclase occurred at Mg# < 55, resulting in depletions of SiO_2, Al_2O_3, Na_2O and K_2O.

Figure 11 provides another independent constraint on the assemblage of liquidus phases. The TiO_2 contents in alkali basalt-hosted clinopyroxenes decreases from about 3 wt % to <1 wt % at $Mg\#_{Cpx} \leq 75$ (Fig. 11c), perhaps owing to Fe–Ti oxide crystallization from the melt (e.g. Stone & Niu 2009). This is consistent with increases in SiO_2 with falling Mg# at $Mg\#_{Cpx} \geq 75$ ($Mg\#_{melt} \approx 43$) (Fig. 11g) because crystallization of Fe–Ti oxides can lead to an SiO_2 jump in the residual melt. The FeO^T contents in both the tholeiites and alkali basalt-hosted clinopyroxenes increase sharply at $Mg\#_{Cpx} \geq 77$ but decline gently and eventually flatten out at $Mg\#_{Cpx} < 77$ (Fig. 11h). This suggests that Fe–Ti oxides possibly begin to crystallize at $Mg\#_{Cpx} = 77$ ($Mg\#_{melt} \approx 44$).

The Na_2O contents in the tholeiite-hosted clinopyroxenes decrease slightly with decreasing $Mg\#_{Cpx}$ in the $Mg\#_{Cpx}$ range 83–77, and increase from about 0·1 to 0·4 wt % with decreasing $Mg\#_{Cpx}$ in the $Mg\#_{Cpx}$ range 77–75 (Fig. 11b). In the lower $Mg\#_{Cpx}$ range (<75), Na_2O in clinopyroxenes decreases again with falling $Mg\#_{Cpx}$ (Fig. 11b). This may reflect crystallization of Na-rich plagioclase, which makes Na_2O less available in the melt for clinopyroxene (e.g. Stone & Niu, 2009). Except for one high CaO analysis, CaO increases with falling $Mg\#_{Cpx}$ at $Mg\#_{Cpx}$ >80 and reaches maximum values at $Mg\#_{Cpx} = 80–75$ (Fig. 11f). At low $Mg\#_{Cpx}$ (<75), CaO decreases sharply with falling $Mg\#_{Cpx}$ (Fig. 11f). This indicates that initial fractional crystallization of clinopyroxene occurred at $Mg\#_{Cpx} = 80–75$ ($Mg\#_{melt} \approx 50–43$), because clinopyroxene fractionation can sharply reduce the CaO content in the residual melt, which makes CaO less available for later crystallized clinopyroxene. The Al_2O_3 contents increase with falling $Mg\#_{Cpx}$ at $Mg\#_{Cpx}$ >80 and then decrease at $Mg\#_{Cpx} < 80$ (Fig. 11e), indicating that plagioclase fractionation began at $Mg\#_{Cpx} \approx 80$ ($Mg\#_{melt} \approx 50$).

Crystallization pressure and temperature

The CIPW norms of the Hainan basalts have been plotted on a Ne–Ol–Di–Hy–Qz projection and compared with cotectics for basaltic liquids in equilibrium with olivine, plagioclase and clinopyroxene at different pressures within the crust (Fig. 3a). Figure 3a shows that the majority of the Hainan basalts lie above and along the 9 (±1·5) kbar cotectic, with a few samples plotting significantly below the 9 kbar cotectic, suggesting that the basalts fractionated mainly at high pressure (≥9 kbar). Below we use three independent approaches (bulk-rock composition, clinopyroxene composition only and clinopyroxene–liquid) to constrain the crystallization pressure and temperature.

The crystallization pressure of dry tholeiitic liquids can be estimated using whole-rock compositions and the Ca–Mg barometer of Villiger *et al.* (2007), which reflects CaO–MgO equilibria for dry tholeiitic melts co-saturated in clinopyroxene and plagioclase. The results show a crystallization pressures range of 1–24 kbar (mostly between 7 and 14 kbar) with a peak at 10–14 kbar (Fig. 12a).

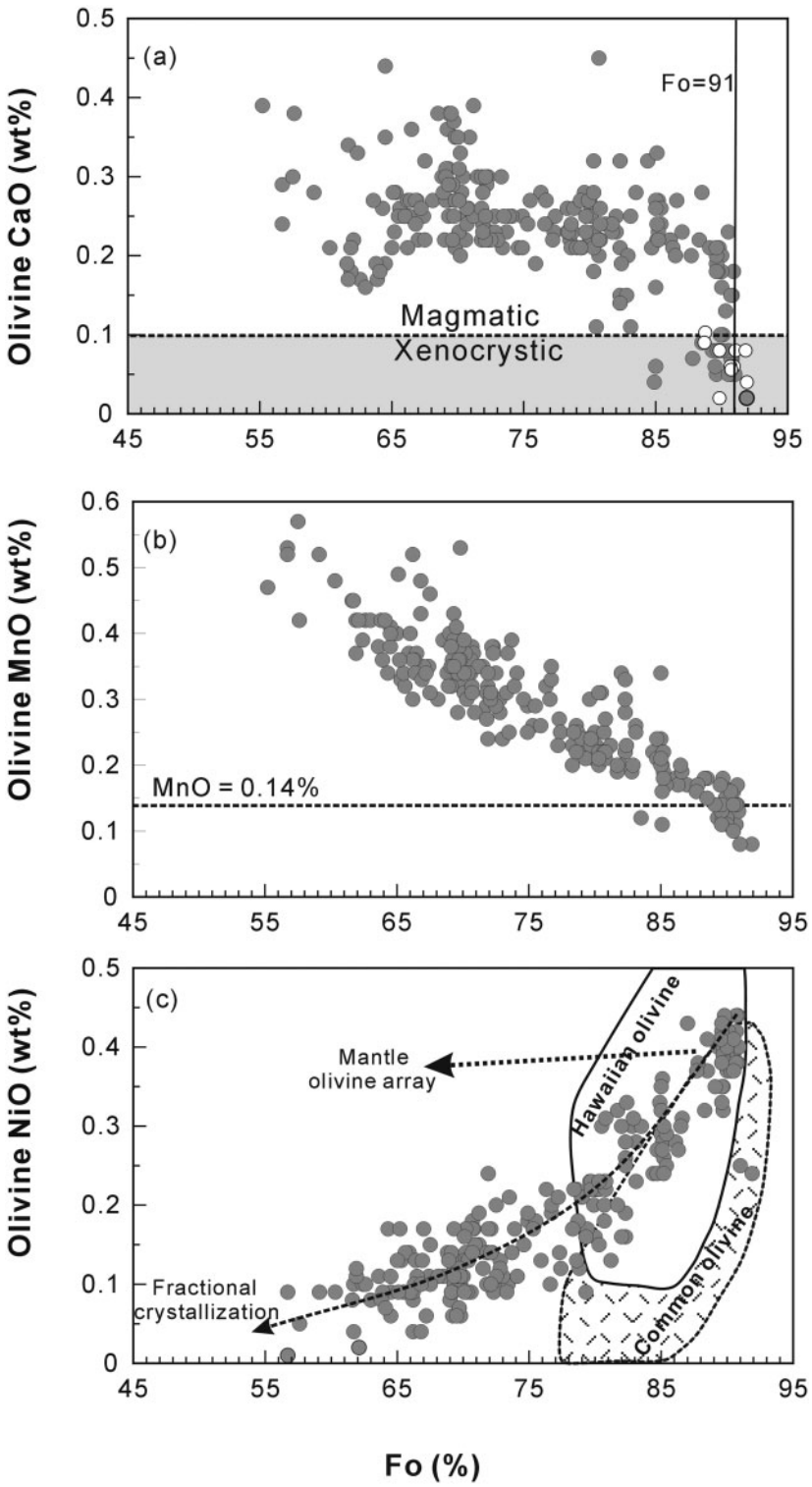

Fig. 8. (a–c) Variations in the composition of olivine phenocrysts. The mantle olivine array and fractional crystallization trend in (c) are from Sato (1977). The dashed line that separates magmatic and xenocrystic olivines on the basis of CaO in (a) is from Thompson & Gibson (2000). The 'common olivine' field outlines the compositional range for olivines from peridotites, mantle xenoliths, orogenic massifs and ophiolites, oceanic abyssal basalts and MORB (Sobolev *et al.*, 2005), whereas the Hawaiian olivine field denotes the range for olivine from Hawaiian basalts, which have been interpreted to have been derived from a hybridized pyroxenitic source formed by reaction of mantle peridotite with melts derived from recycled eclogitic oceanic crust (Sobolev *et al.*, 2005).

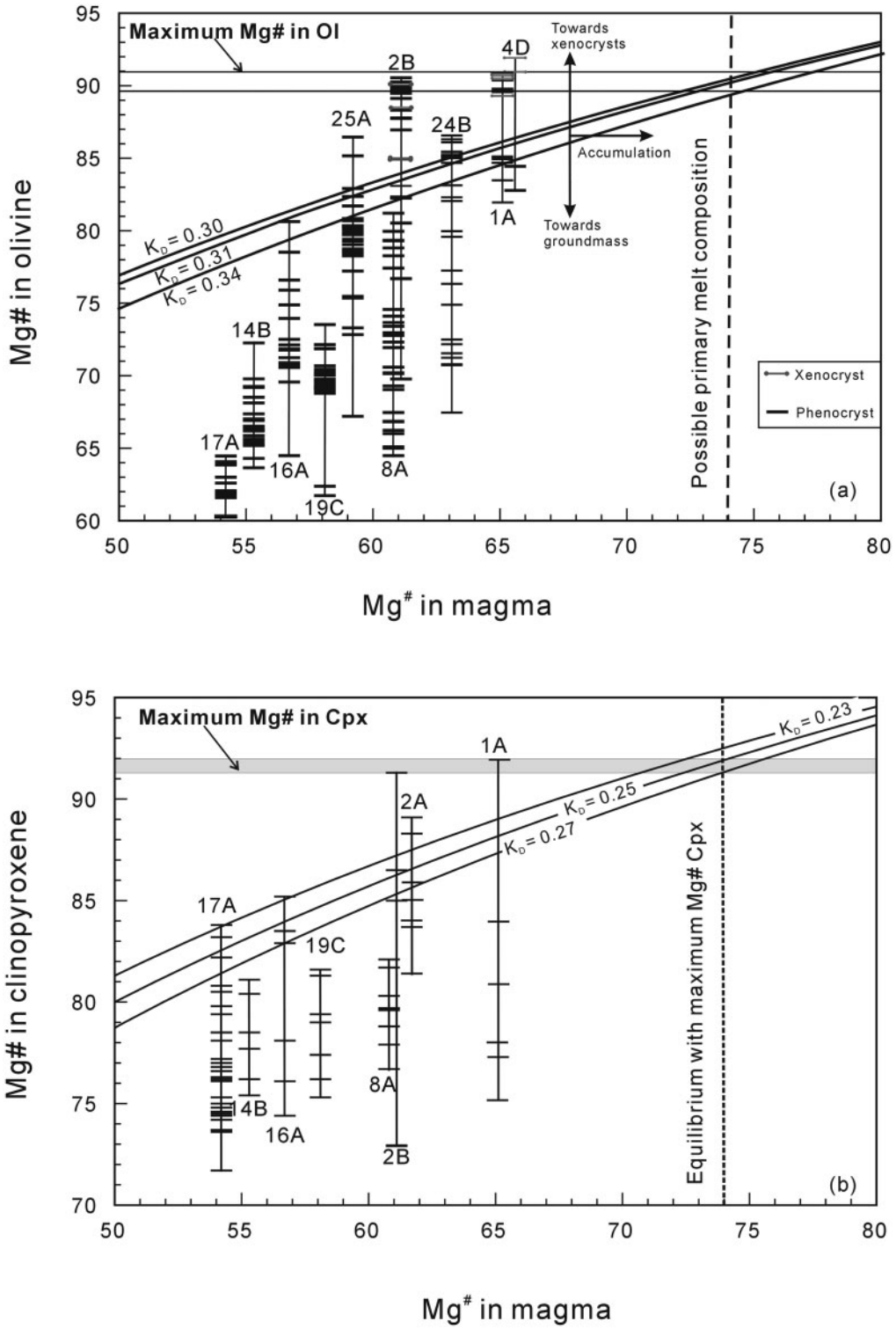

Fig. 9. Mineral–melt Fe/Mg equilibrium diagrams for olivine and clinopyroxene. (a) Whole-rock mg-number (Mg#) vs Fo content (Mg#) of olivine, where mg-number $= Mg^{2+}/(Mg^{2+} + Fe^{2+})$ calculated assuming $Fe^{2+}/Fe_{total} = 0{\cdot}9$ for whole rock and total Fe as Fe^{2+} in olivine. The Fe/Mg exchange partition coefficient between olivine and basaltic liquid is well constrained by experiments to vary from 0·3 at 1 atm equilibrium for a basaltic melt with about 8 wt % MgO (Roeder & Emslie, 1970), to 0·31–0·34 at 5–15 kbar (Ulmer, 1989). Arrows indicate the relative effects of olivine accumulation, high-Mg xenocryst addition, and groundmass crystallization on Fe/Mg equilibrium. (b) Whole-rock Mg# vs clinopyroxene Mg#. The Fe–Mg K_D is slightly dependent on pressure, and probably falls between $0{\cdot}27 \pm 0{\cdot}05$ (Putirka, 1999) and $0{\cdot}23 \pm 0{\cdot}05$ (Toplis & Carroll, 1995).

Table 5: Representative electron probe analyses of clinopyroxene from the Hainan basalts

Host rock:	08HN-1A						08HN-2A							08HN-2B	08HN-2B				08HN-8A			
Probe no.:	1A-1R	1A-1M	1A-1C	1A-2R	1A-2M	1A-2C	2A-1M	2A-1C	2A-2M	2A-2R	2A-3R	2A-3C	2A-3M	2B-1M	2B-1R	2B-2R	2B-2M	2B-2C	8A-1M	8A-1R	8A-1C	8A-2C
SiO_2	50·9	49·35	52·18	49·89	53·15	51·83	49·53	51·53	52·28	49·81	50·42	53·2	51·78	51·7	53·5	53·3	51·1	53·2	52·18	49·21	50·39	51·35
TiO_2	1·35	1·97	0·92	1·78	0·72	0·03	2·09	0·54	0·51	0·65	1·04	0·72	1·23	0·73	0·69	0·38	0·78	0·4	1·28	1·89	1·47	1·18
Al_2O_3	2·41	4·31	2·08	3·59	6·81	3·37	4·85	7·35	7·42	10·74	2·2	6·81	2·52	2·02	0·14	0·11	6·19	6·2	2·69	4·49	2·98	4·11
Cr_2O_3		0·24	0·46	0·13	0·27	0·77	0·7	0·64	0·66	0·25	0·32	0·27	0·11	0·79	0	0·04	0·89	0·91	0·25	0·26	0·2	0·77
FeO^T	8·08	7·43	6·95	8·39	4·59	4·87	6·08	3·51	3·5	5·45	7·05	4·59	8·8	7·36	9·02	9·26	5·37	2·57	7·32	7·59	7·51	5·93
MnO	0·19	0·29	0·15	0·24	0·05	0	0·14	0·1	0·13	0·08	0·14	0·05	0·14	0·15	0·2	0·2	0·11	0·1	0·2	0·12	0·15	0·1
MgO	15·5	14·82	16·46	14·33	13·53	18·79	13·99	14·87	14·81	14·28	15·91	13·5	14·38	16·4	13·4	12·9	14·9	15·2	15·13	13·72	14·64	15·29
CaO	20·5	20·79	20·84	21·14	19·32	18·74	21·12	19·18	18·52	17·48	21·73	19·3	19·88	20·1	21·6	22	18·8	19·4	20·92	21·29	21·34	20·37
Na_2O	0·3	0·42	0·27	0·36	1·52	0·54	0·74	1·68	1·72	1·54	0·49	1·52	0·58	0·71	0·7	0·69	1·64	1·64	0·51	0·45	0·37	0·57
Total	99·2	99·62	100·3	99·85	99·96	98·94	99·23	99·4	99·54	100·3	99·3	100	99·43	99·9	99·2	98·9	99·7	99·6	100·5	99·02	99·06	99·66
Cations based on 6 oxygens per formula unit																						
Si	1·900	1·835	1·916	1·859	1·922	1·875	1·844	1·873	1·891	1·794	1·922	1·88	1·862	1·91	2·01	2·01	1·87	1·92	1·919	1·846	1·886	1·892
Ti	0·040	0·055	0·025	0·05	0·02	0·001	0·058	0·015	0·014	0·018	0·02	0·03	0·029	0·02	0·02	0·01	0·02	0·01	0·035	0·053	0·041	0·033
Al	0·110	0·189	0·09	0·158	0·29	0·186	0·213	0·315	0·316	0·456	0·29	0·1	0·096	0·09	0·01	0·01	0·27	0·26	0·116	0·199	0·131	0·178
Al^{IV}	0·100	0·165	0·084	0·141	0·078	0·125	0·156	0·127	0·109	0·206	0·078	0·1	0·096	0·09	0	0	0·14	0·08	0·081	0·154	0·114	0·108
Al^{VI}	0·010	0·024	0·006	0·017	0·212	0·062	0·057	0·187	0·208	0·25	0·212	0	0	0	0·01	0·01	0·13	0·18	0·036	0·045	0·017	0·07
Cr	0·000	0·007	0·013	0·004	0·008	0·022	0·021	0·019	0·019	0·007	0·008	0·01	0·009	0·02	0	0	0·03	0·03	0·007	0·008	0·006	0·022
Fe^{3+}	0·030	0·04	0·025	0·035	0	0·058	0·012	0·008	0	0·015	0	0·06	0·064	0·07	0·01	0·02	0·04	0	0·003	0·021	0·026	0
Fe^{2+}	0·220	0·191	0·188	0·226	0·139	0·09	0·178	0·099	0·106	0·149	0·139	0·16	0·154	0·16	0·28	0·27	0·13	0·08	0·223	0·217	0·209	0·183
Mn	0·010	0·009	0·005	0·008	0	0	0·004	0·003	0·004	0·003	0	0	0·004	0·01	0·01	0·01	0	0	0·006	0·004	0·005	0·003
Mg	0·860	0·821	0·901	0·796	0·729	1·013	0·776	0·805	0·799	0·767	0·729	0·88	0·93	0·9	0·75	0·72	0·81	0·82	0·829	0·767	0·817	0·839
Ca	0·820	0·828	0·82	0·844	0·749	0·727	0·842	0·747	0·718	0·674	0·749	0·87	0·86	0·79	0·87	0·89	0·73	0·75	0·824	0·856	0·856	0·804
Na	0·020	0·03	0·019	0·026	0·107	0·038	0·054	0·119	0·121	0·107	0·107	0·04	0·035	0·05	0·05	0·05	0·12	0·12	0·036	0·033	0·027	0·041
Sum	4·010	4·007	4·007	4·007	3·963	4·01	4·003	4·002	3·988	4·015	3·963	4·03	4·043	4·01	3·99	3·99	4·01	3·98	4·001	4·004	4·004	3·996
End-member (%)																						
Wo	43·5	45·5	43·4	45·7	46·3	40·4	47·1	45·4	44·2	43·7	47·3	46·3	42·5	43·7	45·8	46·7	44·5	45·7	48·5	46·8	45·8	44
En	45·5	45·1	47·7	43·1	45·1	56·3	43·4	48·9	49·2	49·6	48·2	45·1	42·8	49·5	39·3	37·9	49·2	49·6	40·1	42	43·7	46
Fs	11	9·4	8·9	11·2	8·6	3·4	9·5	5·7	6·5	6·7	4·5	8·6	14·7	6·8	14·9	15·3	6·3	4·7	11·3	11·2	10·5	10
Mg#	79·4	81·1	82·7	77·9	84	91·9	81·4	89·1	88·3	83·7	84	85	85·8	85	72·9	72·9	86·5	91·3	78·8	77·9	79·6	82·1

(continued)

Table 5: Continued

Host rock:	08HN-8A					08HN-14B	08HN-14B							08HN-16A						
Probe no.:	8A-2M	8A-2R	8A-3R	8A-3C	8A-3M	14B-1R	14B-1M	14B-1C	14B-2C	14B-2R	14B-3R	14B-4C	14B-5C	16A-1R	16A-1M	16A-2C	16A-2R	16A-3R	16A-3C	16A-4C
SiO_2	49·9	50·59	51·24	51·8	50·38	50·23	52·7	51·86	52·03	52·63	50·61	52·12	51·97	50·22	50·44	49·29	51·44	51·78	50·98	50·1
TiO_2	1·88	1·86	1·43	0·94	1·66	1·92	0·75	0·96	0·9	0·87	2·27	1·05	0·99	1·69	1·23	0·85	1·13	1·23	0·7	1·16
Al_2O_3	5·02	4·62	3·27	3·57	4·56	1·99	1·83	2·91	2·22	0·87	2·89	1·97	1·77	4·02	2·6	2·48	3·24	2·52	2·32	3·46
Cr_2O_3	0·81	0·61	0·15	0·44	0·36	0	0·52	0·53	0·58	0·01	0	0·28	0·22	0·2	0·2	0·5	0·73	0·11	0·18	0·28
FeO^T	6·33	6·52	7·97	6·34	6·53	9·1	8·25	7·73	7·71	14·32	10·69	8·28	8·37	7·7	7·51	8·58	7·49	8·8	9·16	7·85
MnO	0·15	0·13	0·16	0·13	0·12	0·2	0·16	0·21	0·12	0·36	0·19	0·14	0·18	0·09	0·14	0·2	0·16	0·14	0·19	0·14
MgO	14·3	14·34	14·68	15·8	14·4	14·79	16·1	16·29	16·79	12·69	12·54	14·9	15·92	13·76	15·48	17·78	14·95	14·38	17·85	16·65
CaO	21·1	21·31	20·21	19·6	21·07	20·71	18·8	19·32	19·2	17·25	20·12	19·89	19·84	20·96	20·97	19·94	19·75	19·88	19·08	19·22
Na_2O	0·51	0·42	0·41	0·58	0·42	0·49	0·42	0·45	0·38	0·64	0·63	0·4	0·35	0·47	0·44	0·37	0·45	0·58	0·46	0·58
Total	100	100·4	99·53	99·2	99·5	99·43	99·5	100·3	99·93	99·63	99·94	99·04	99·61	99·11	99·01	99·98	99·32	99·43	100·9	99·43
Cations based on 6 oxygens per formula unit																				
Si	1·84	1·862	1·906	1·91	1·869	1·889	1·95	1·906	1·917	1·993	1·901	1·947	1·93	1·88	1·883	1·832	1·912	1·932	1·867	1·854
Ti	0·05	0·051	0·04	0·03	0·046	0·054	0·02	0·027	0·025	0·025	0·064	0·03	0·028	0·048	0·034	0·024	0·031	0·034	0·019	0·032
Al	0·22	0·2	0·144	0·16	0·2	0·088	0·08	0·126	0·096	0·039	0·128	0·087	0·077	0·177	0·115	0·109	0·142	0·111	0·1	0·151
Al^{IV}	0·16	0·138	0·094	0·09	0·131	0·088	0·05	0·094	0·083	0·007	0·099	0·053	0·07	0·12	0·115	0·109	0·088	0·068	0·1	0·146
Al^{VI}	0·06	0·062	0·049	0·07	0·068	0	0·03	0·032	0·013	0·031	0·029	0·034	0·007	0·057	0	0	0·054	0·043	0	0·005
Cr	0·02	0·018	0·004	0·01	0·011	0	0·02	0·015	0·017	0	0	0·008	0·006	0·006	0·006	0·015	0·021	0·003	0·005	0·008
Fe^{3+}	0	0	0	0	0	0·015	0	0·02	0·023	0	0	0	0·019	0	0·057	0·073	0	0	0·089	0·083
Fe^{2+}	0·19	0·201	0·248	0·2	0·203	0·271	0·26	0·218	0·215	0·454	0·336	0·259	0·241	0·241	0·177	0·194	0·233	0·275	0·192	0·16
Mn	0·01	0·004	0·005	0	0·004	0·006	0·01	0·006	0·004	0·012	0·006	0·005	0·006	0·003	0·005	0·006	0·005	0·004	0·006	0·004
Mg	0·79	0·786	0·814	0·87	0·796	0·829	0·89	0·892	0·922	0·716	0·702	0·83	0·881	0·768	0·861	0·985	0·828	0·8	0·974	0·918
Ca	0·84	0·84	0·805	0·78	0·837	0·835	0·75	0·761	0·758	0·7	0·81	0·796	0·79	0·841	0·839	0·794	0·787	0·795	0·749	0·762
Na	0·04	0·03	0·03	0·04	0·03	0·036	0·03	0·032	0·027	0·047	0·046	0·029	0·025	0·034	0·032	0·026	0·032	0·042	0·033	0·042
Sum	4	3·993	3·995	4	3·995	4·024	4	4·004	4·004	3·989	3·994	3·991	4·003	3·998	4·01	4·061	3·991	3·997	4·033	4·014
End-member (%)																				
Wo	46	46	43·1	42·1	45·6	44·8	39·5	40·9	40·3	37·4	43·8	42·2	41·5	45·4	45·4	44·3	42·6	42·5	41·2	42·4
En	43·4	43	43·6	47·3	43·4	44·5	47	48	49	38·3	38	44	46·3	41·5	46·6	55	44·8	42·8	53·7	51·1
Fs	10·6	11	13·3	10·6	11	10·7	13·5	11·1	10·8	24·3	18·2	13·7	12·1	13	8	0·7	12·6	14·7	5·1	6·6
Mg#	80·3	79·7	76·7	81·7	79·7	75·4	77·7	80·4	81·1	61·2	67·7	76·2	78·5	76·1	82·9	83·5	78·1	74·4	83·5	85·2

Cations were calculated on six-oxygen basis following the procedure of Lindsley (1983). Fe^{2+} and Fe^{3+} were calculated based on charge-balance considerations using clinopyroxene formula spreadsheet Cpx__formula.V2 (http://serc.carleton.edu/files/research__education/equilibria/cpx__formula.v2.xls). C, M and R after probe numbers indicate core, mantle and rim of Cpx phenocrysts, respectively. FeO^T total iron as FeO.

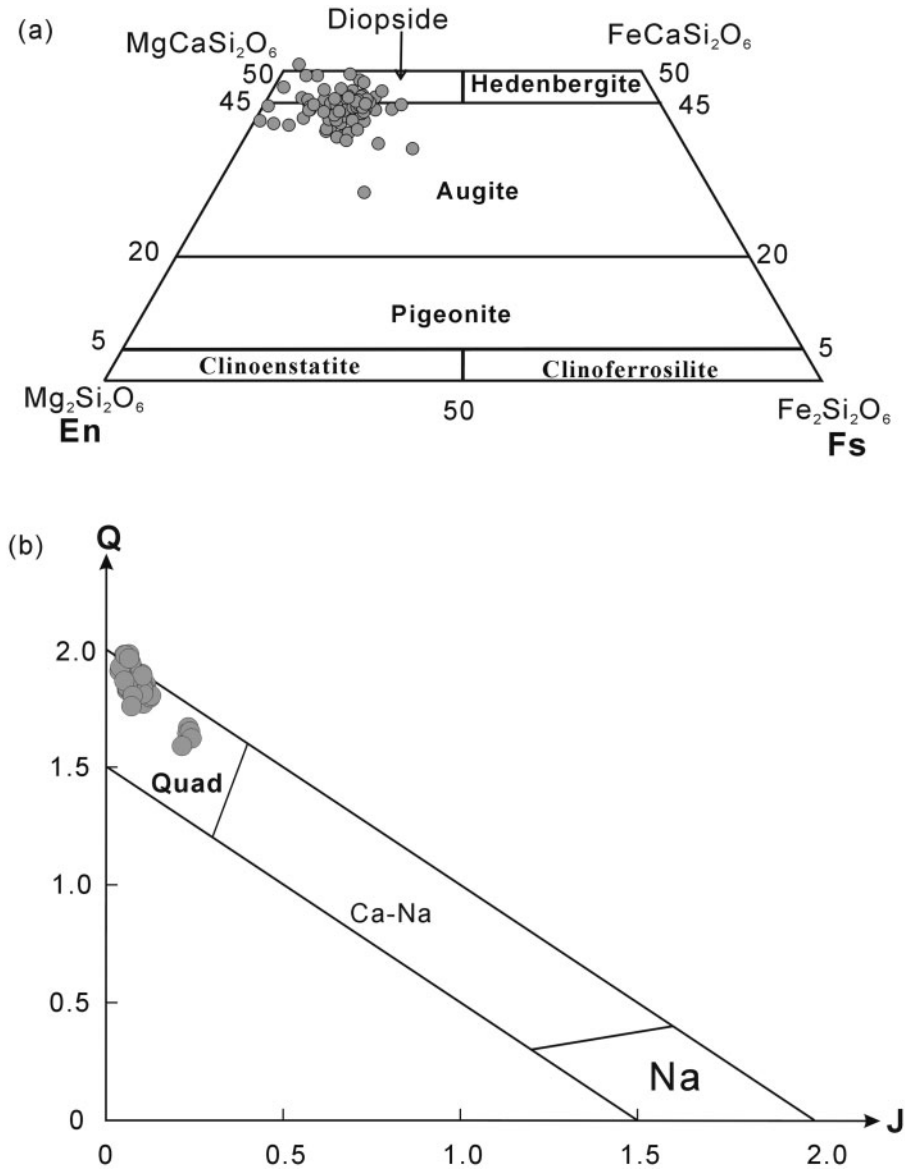

Fig. 10. Compositional variations in clinopyroxenes in the Hainan basalts. (a) The pyroxene quadrilateral; (b) Q–J diagram. Abbreviations and compositions of the end-members are after Morimoto (1988).

The empirical approach of Soesoo (1997) uses principal component analysis of the major-element composition of clinopyroxenes crystallized from melting experiments to construct eigenvector grids for *P* and *T*. On Soesso's plots (Fig. 12b), clinopyroxenes predict a large range of pressure (2–15 kbar) and temperature conditions (1100–1300°C).

Putirka *et al.* (1996, 2003) and Putirka (1999, 2008) established a series of thermodynamic equations based on experimental work that relate temperature and pressure to equilibrium constants and allow for the construction of clinopyroxene–liquid thermobarometers. We carried out two calculations using these equations. First, we used only clinopyroxene compositions that fell well within the Fe–Mg equilibrium field in Fig. 9b. In this case, the whole-rock compositions of the host-rocks were regarded as liquid compositions. The thermobarometers from Putirka *et al.* (2003) were used to constrain the crystallization pressure and temperature (Fig. 12c and d). The calculated temperatures range from 1062 to 1322°C and have two main populations of 1120–1150°C and 1240–1350°C (Fig. 12c). The calculated pressures range from 2 to 25 kbar with three populations of 1–7, 10–19 and 22–25 kbar (Fig. 12d). Second, we employed the equations T1 and P1 from Putirka *et al.* (1996), equations 31, 32c and 33

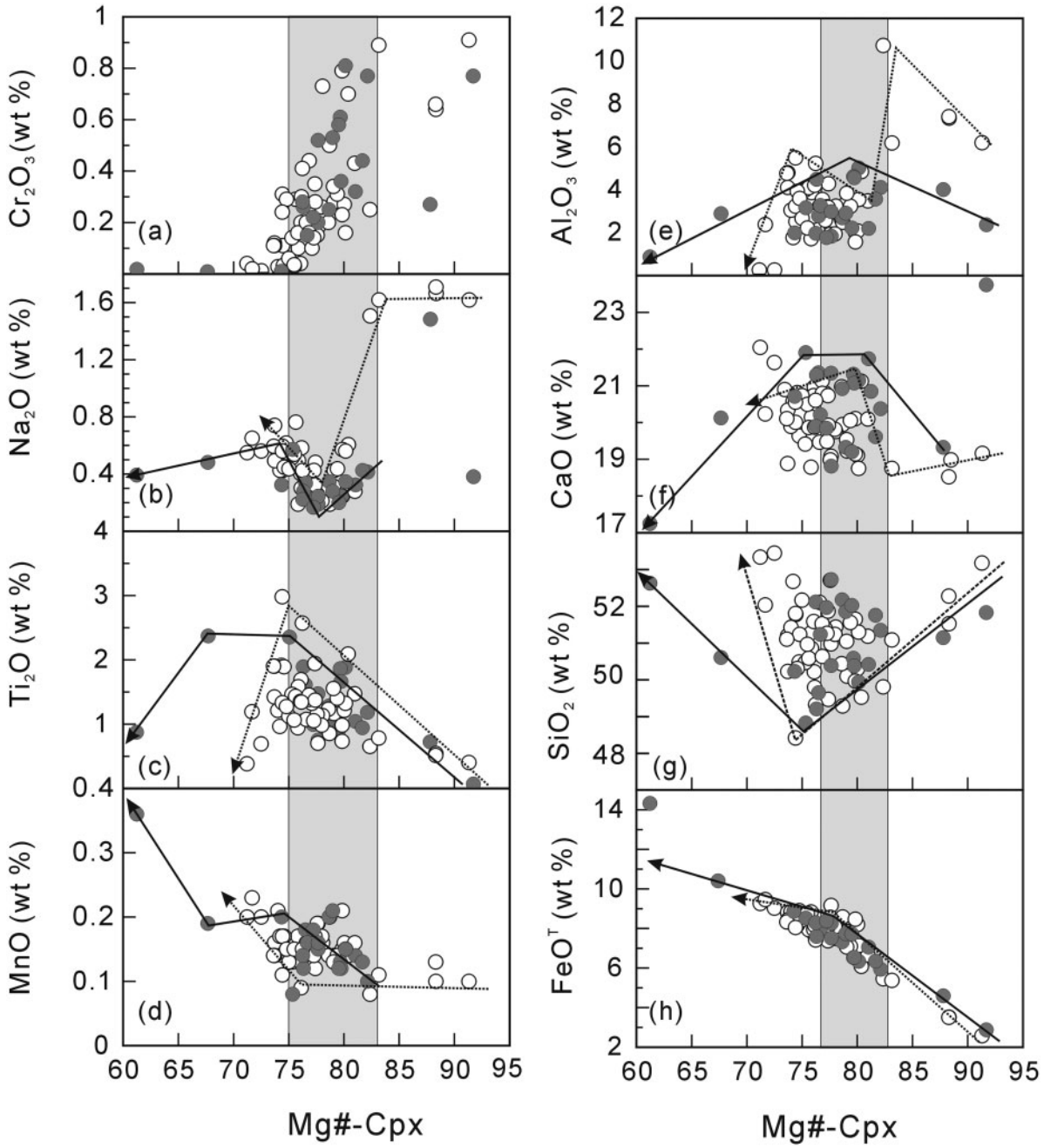

Fig. 11. Chemical variations of clinopyroxene phenocrysts. The grey bands highlight the kinks in the trends of the major elements vs Mg# in clinopyroxene. The continuous-line and dotted-line arrows indicate the trends of clinopyroxenes hosted by tholeiites and alkali basalts, respectively.

from Putirka (2008), and thermobarometers from Putirka *et al.* (2003) to calculate the crystallization pressures and temperatures of all analysed clinopyroxene compositions. The host whole-rock compositions were adjusted to be in equilibrium with clinopyroxenes using an Fe–Mg partition coefficient of 0·25 for clinopyroxene/melt, by adding or subtracting clinopyroxene. The results are presented in Fig. 12e and f. The majority of the calculated temperatures range from 1100 to 1250°C with two populations of 1100–1180°C and 1200–1280°C. A few temperatures fell within the field >1300°C. The majority of the calculated pressures fall in the range of 7–15 kbar with a peak of 10–14 kbar. A few clinopyroxenes predict pressures of 2–4 and 22–24 kbar. Overall, the two model calculations gave similar

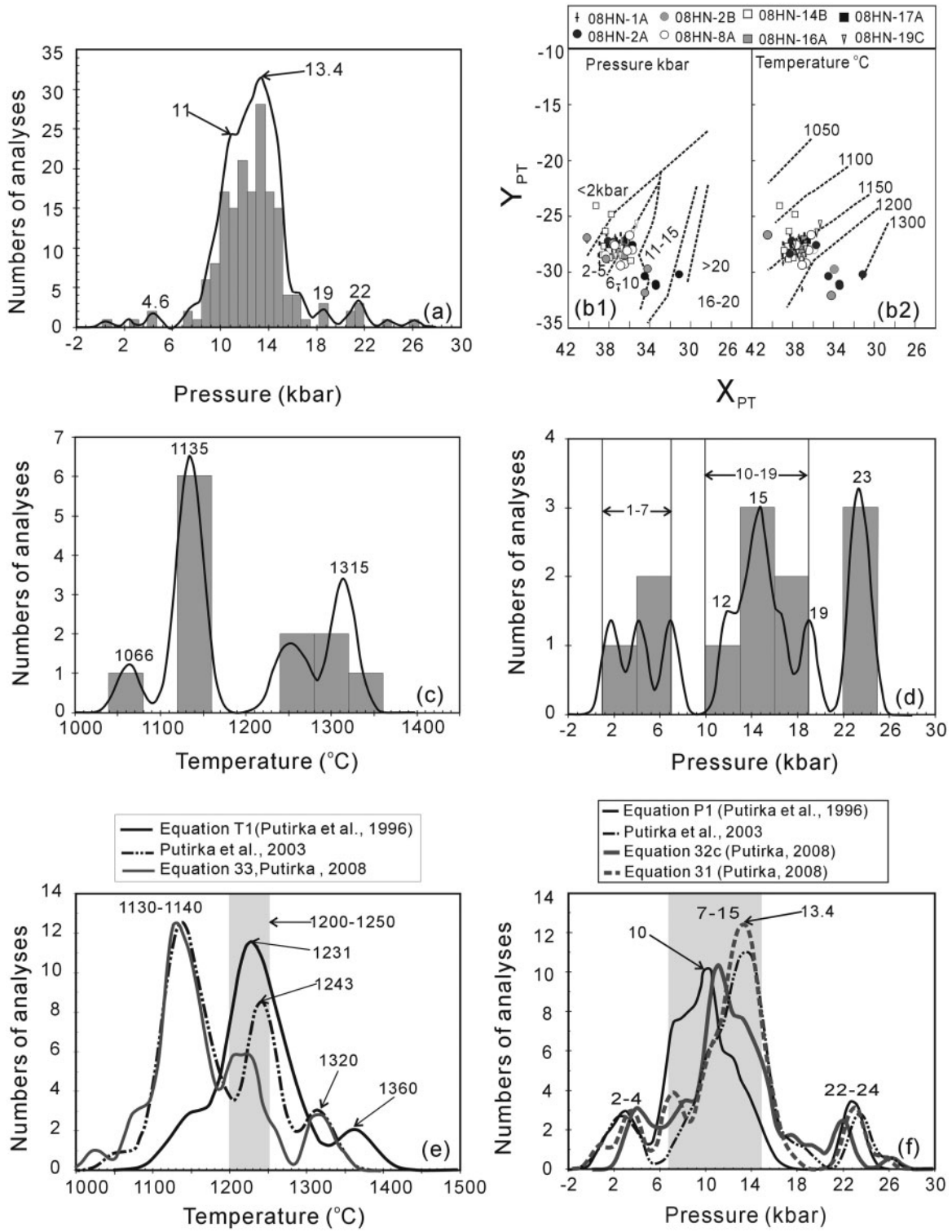

Fig. 12. Crystallization pressure and temperature estimates for the Hainan basalts based on (a) tholeiitic whole-rock data; (b) clinopyroxene only; (c, d) equilibrium clinopyroxene–liquid; (e, f) all clinopyroxene–host rock.

crystallization T–P ranges: the magma initially crystallized at high pressure (20–25 kbar) and high temperature (1300–1350°C) and then mainly fractionated at 10–15 kbar and moderate temperatures of 1100–1250°C. The results also indicate that the parental magma cooled from at least 1350°C to 1100°C.

Primary melt compositions

Primary melt compositions have been widely used as probes of the thermal state of their mantle sources (e.g. McKenzie & Bickle, 1988; Albarède, 1992; Langmuir *et al.*, 1992; Putirka, 2005; Herzberg *et al.*, 2007; Putirka *et al.*, 2007). The discussion above shows that clinopyroxene fractionation has little effect on high Mg# (>61) alkali basalts and most tholeiites. Furthermore, the trend of CaO–$Mg\#_{Cpx}$ indicates that clinopyroxene in the tholeiites most probably began to crystallize at Mg# < 50. Available data for the Hainan basalts allow us to produce a regression equation of $MgO = 0{\cdot}0051 \times (Mg\#)^2 - 0{\cdot}2669 \times Mg\# + 5{\cdot}805$ ($R^2 = 0{\cdot}88$, $n = 146$). Using this equation, Mg# = 61 corresponds to MgO ≈ 8·5 wt %. Thus, the effect of clinopyroxene fractionation on samples with MgO > 8·5 wt % is negligible, if any.

To minimize the effect of clinopyroxene fractionation, only samples with MgO ≥ 9 wt % and CaO > 8 wt % were chosen as starting compositions. A series of olivine and basalt compositions were then calculated from these starting materials as follows: (1) the composition of equilibrium olivine was obtained using $K_D(Fe/Mg)^{oliv/liq} = 0{\cdot}31$ (Putirka, 2005) and $D_{Ni}{}^{oliv/liq}$ (Beattie *et al.*, 1991), assuming that $Fe^{2+}/(Fe^{2+} + Fe^{3+}) = 0{\cdot}90$ in the melt; (2) a more primitive basalt composition was calculated as a mixture of the basalt and equilibrium olivine in a weight ratio of 99·9:0·1; (3) steps (1) and (2) were repeated using the calculated primitive basalt to obtain a more primitive basalt. For the Hainan basalts, the most high-magnesian phenocrystic olivines have values of $Fo_{90{\cdot}7}$ and 0·38 wt % NiO. Therefore, the calculations of olivine and basalt compositions were repeated until the calculated equilibrium olivines had a value of $Fo_{90{\cdot}7}$. The amount of olivine addition required to achieve liquid Mg# values consistent with a $Fo_{90{\cdot}7}$ source is typically between 17 and 25% for the Hainan basalts (Table 6).

An independent constraint on the extent of olivine addition can be obtained by comparing the compositions of calculated olivines and real phenocrystic olivines (e.g. Tamura *et al.*, 2000; Leeman *et al.*, 2005). As shown in Fig. 13, the NiO contents in calculated olivines are similar to those of real phenocrystic olivines, suggesting that the calculated primary magmas represent the primary melt composition.

Twenty-eight samples (Table 6) were selected as starting materials to calculate the primary melts for the Hainan basalts. The tholeiites and alkali basalts have similar estimated primary melt compositions except for their SiO_2 contents. The tholeiites are characterized by highly variable SiO_2 contents of 50–45 wt %, whereas the alkali basalts show relatively low SiO_2 contents of 47–45 wt %. Compared with ocean island basalts (OIB), the calculated primary melt compositions are similar to those of fractionation-corrected EM-1 and EM-2 type OIB (Fig. 14). The estimated primary melt compositions plot within the overlap of experimental fields defined by partial melting of silica-deficient eclogite and peridotite (Fig. 14).

Melting conditions and mantle thermal state

Melting conditions and mantle potential temperatures can be estimated using primary melt compositions (e.g. McKenzie & Bickle, 1988; Langmuir *et al.*, 1992; Putirka, 2005, 2008; Herzberg *et al.*, 2007; Putirka *et al.*, 2007; Lee *et al.*, 2009). The calculated results are presented in Table 6.

The estimated melting temperature (T) at which melts separate from the melting column varies from 1420 to 1520°C for the tholeiites and from 1480 to 1530°C for the alkali basalts (Table 6). Effective melting pressure (P_f), an average equilibration pressure, is 25–32 kbar (with a weighted average of 28·3 ± 1·4 kbar) for the alkali basalts, and 18–32 kbar (with a weighted average of 23·8 ± 1·8 kbar) for the tholeiites. This is consistent with the presence of significant (18–32%) ^{230}Th excess in the Holocene Hainan basalts that requires a melting depth >75 km (~25 kbar) (Zou & Fan, 2010). The initial melting pressure (P_i), at the bottom of the melting column, is calculated by the intersection of convective geotherms with the mantle solidus (Putirka *et al.*, 2007). Estimated P_i values for the tholeiites and alkali basalts are similar, typically between 30 and 38 kbar (Table 6). As the mantle source ascends above the solidus, the total melt fraction F increases until the pressure at which the mantle source ceases to ascend adiabatically (P_f) and therefore ceases to melt. The degree of melting is proportional to the length of the melting column, except at relatively shallow depth (e.g. Asimow *et al.*, 1997). F may also be a function of melting pressure, temperature and melt composition (e.g. McKenzie, 1984; Putirka *et al.*, 2007). In this study, F was estimated using an experimental regression equation [equation A2 in the appendix of Putirka *et al.* (2007)]. The estimated F values are presented in Table 6.

Mantle potential temperature (T_p) is a key parameter for describing the thermal state of the upper mantle (e.g. McKenzie & Bickle, 1988; Albarède, 1992; Langmuir *et al.*, 1992; Thompson & Gibson, 2000; Putirka, 2005, 2008; Campbell, 2007; Herzberg *et al.*, 2007; Wang *et al.*, 2007, 2009). There are two main approaches for modeling T_p: (1) calculating T_p using melt composition, as FeO, Na_2O (e.g. Kelley *et al.*, 2006) and MgO contents (e.g. Herzberg *et al.*, 2007, and references therein), based on the pooled, accumulated fractional melting model; (2) using the equation $T_p = T + F(H_{fus}/C_p) - \partial T/\partial P$ (e.g. Putirka *et al.*, 2007).

Table 6: Estimated primary melt compositions, mantle potential temperatures and melting conditions for late Cenozoic Hainan basalts

Starting sample:	08HN-1A	08HN-2A	08HN-2B	08HN-3	08HN-8A	08HN-22D	08HN-24A	08HN-24B	08HN-24D	HN9907
Reference:	T	T	T	T	T	T	T	T	T	Z10
Rock type:	QT	AB	AB	QT	QT	AB	AB	AB	QT	QT
Olivine add (%):	18	23	25	21	24	25	20	20	19	17
NiO (wt %):	0·39	0·4	0·4	0·39	0·28	0·27	0·31	0·3	0·3	
wt %										
SiO_2	47·25	46·65	46·92	46·58	48·21	45·84	47·18	47·01	47·3	48·46
TiO_2	2	2·38	2·26	2·19	1·78	2·07	2	1·98	1·94	1·98
Al_2O_3	10·41	10·39	10·49	10·34	10·13	10·16	10·74	10·71	10·99	11·51
FeO	10·42	11·05	10·95	11·18	10·72	11·11	10·38	10·53	10·33	9·54
MnO	0·11	0·11	0·11	0·12	0·14	0·13	0·12	0·12	0·12	0·23
MgO	16·8	18·11	17·92	18·29	17·64	18·17	16·95	17·3	16·86	15·64
CaO	7·08	6·29	6·35	7·67	7·58	7·74	7·83	7·68	7·88	8·15
Na_2O	2	1·8	2·64	2·18	2·57	2·39	2·45	2·34	2·27	2·2
K_2O	1·06	1·09	1·08	0·78	1·07	1·18	1	0·76	0·87	1·19
Fe_2O_3	1·03	1·06	1·03	1·1	1·01	1·04	1·02	1·03	1·02	0·97
P_2O_5	0·53	0·46	0·48	0·51	0·35	0·31	0·48	0·36	0·35	0·39
H_2O^1	1·28	1·19	1·18	0·83	0·73	1·37	1·07	0·92	0·9	1·07
H_2O^2	1·38	1·42	1·4	1·02	1·39	1·54	1·3	0·99	1·13	1·54
F%	14	16	16	17	19	14	15	16	15	15
P_f^1	31·2	32·3	31·1	32	27·1	34·7	27·9	28·8	26·8	21·6
P_f^2	22·7	26·6	25·3	27·1	20·8	29·9	23·1	24·1	22·6	17·9
P_f^3	27·6	27·8	26·6	28·1	20·9	31·3	25·5	26·2	24·9	19·9
P_f^4	27·3	27·6	26·9	27	24·2	28·2	24·2	24·7	23·3	19·4
P_f^5	27·2	28·6	27·5	28·5	23·3	31	25·2	26	24·4	19·7
SD	3·5	2·5	2·5	2·3	3	2·7	2	2·1	1·9	1·5
P_i	32·4	36·3	35·8	37·5	35·9	36	33·1	34·4	37·6	29·3
T^1	1466	1498	1506	1514	1498	1509	1474	1484	1469	1429
T^2	1494	1528	1522	1533	1505	1537	1498	1507	1495	1457
T^3	1526	1527	1519	1533	1500	1543	1492	1502	1487	1441
T^4	1495	1518	1516	1527	1501	1529	1488	1498	1483	1442
SD	30	17	8	11	3	18	12	12	13	14
T_p^1	1503	1532	1528	1536	1522	1534	1506	1514	1504	1475
T_p^2	1555	1600	1594	1606	1584	1602	1560	1572	1557	1512
T_p^3	1534	1586	1579	1594	1568	1589	1540	1554	1537	1490
T_p^4	1505	1555	1546	1565	1529	1559	1502	1514	1498	1441
T_p^5	1570	1597	1600	1611	1625	1556	1578	1589	1413	
T_p^6	1534	1574	1569	1582	1566	1568	1538	1549	1502	1480
SD	30	30	31	31	42	27	33	34	55	30

(continued)

The calculated T_p values using the two approaches are comparable, and we take the average T_p as the final result (Table 6). The tholeiites and alkali basalts have similar T_p ranging from about 1500 to 1580°C with a weighted average of 1541 ±10°C.

To evaluate the significance of this result, it is important to consider the uncertainties involved in obtaining melting conditions and mantle potential temperatures. These mainly concern the value of K_D, redox state (Fe^{3+}/total Fe), mantle Mg#, and water content. Variations in Fe^{3+}/

Table 6: Continued

Starting sample:	HN9910	HN9911	HN9912	HN9914	HN9908	HN9910	220B-3	220B-4	219BI	219B4
Reference:	Z10	Z10	Z10	Z10	Z10	F04	F04	F04	F04	F04
Rock type:	AB	AB	AB	QT	AB	AB	QT	QT	QT	QT
Olivine add (%):	20	19	21	17	20	24	18	19	19	18
NiO (wt %):						0·26				
wt %										
SiO_2	45·45	45·97	45·27	49·06	45·22	45·39	47·34	47·4	46·87	46·9
TiO_2	2·31	2·39	2·31	1·88	2·35	2·19	1·97	1·99	2·03	2·02
Al_2O_3	10·88	11·23	10·74	12·02	10·72	10·31	11·04	11·05	11·64	11·07
FeO	10·52	9·97	10·47	9·03	10·58	11·06	10·18	10·22	10·29	10·24
MnO	0·26	0·16	0·17	0·13	0·17	0·25	0·13	0·12	0·11	0·12
MgO	17·25	16·3	17·19	14·8	17·32	18·1	16·71	16·8	16·86	16·85
CaO	9·05	9·02	8·8	8·12	8·83	8·57	8·38	8·2	8·28	8·48
Na_2O	2·03	2·55	2·63	2·7	2·38	1·92	2	1·95	1·82	1·97
K_2O	1·08	1·25	1·23	0·8	1·23	1·22	1·09	1·13	0·96	1·17
Fe_2O_3	1·05	1·01	1·05	0·92	1·06	1·07	1·04	1·02	1·03	1·04
P_2O_5	0·64	0·61	0·62	0·35	0·67	0·6	0·38	0·4	0·4	0·46
H_2O^1	1·96	1·86	1·84	0·72	1·96	1·84				
H_2O^2	1·4	1·63	1·6	1·04	1·6	1·59	1·41	1·47	1·25	1·53
F%	12	11	11	15	11	13	15	16	14	14
P_f^1	31·9	29·5	34·1	19·8	34	34	25·7	25·7	26·3	27·1
P_f^2	30	26·4	30·7	15·6	31·1	31·8	22·3	22·2	24	23·9
P_f^3	33	30·8	33·8	17·2	34·1	33·3	24·8	24·5	26·8	26·7
P_f^4	25·7	24·8	27·6	18·6	27·3	27·1	22·2	22·3	22·5	23·2
P_f^5	30·2	27·9	31·6	17·8	31·6	31·6	23·7	23·7	24·9	25·2
SD	3·2	2·8	3·1	1·8	3·2	3·1	1·8	1·7	2	2
P_i	32·5	30·1	32·4	27·3	32·6	35	32·6	32·9	33	33
T^1	1467	1449	1478	1414	1477	1492	1459	1462	1459	1464
T^2	1519	1493	1520	1433	1523	1539	1491	1492	1498	1498
T^3	1520	1488	1524	1414	1527	1547	1482	1483	1489	1490
T^4	1502	1476	1507	1420	1509	1526	1477	1479	1482	1484
SD	30	24	25	11	28	30	17	16	20	18
T_p^1	1513	1491	1512	1454	1515	1532	1501	1503	1504	1504
T_p^2	1570	1537	1569	1481	1573	1600	1552	1555	1557	1556
T_p^3	1552	1515	1550	1459	1555	1586	1531	1535	1537	1536
T_p^4	1513	1472	1509	1407	1517	1555	1487	1490	1495	1492
T_p^5	1483	1478	1466	1540	1463	1508	1577	1582	1570	1570
T_p^6	1526	1504	1521	1468	1525	1556	1530	1533	1533	1532
SD	35	28	40	49	42	38	36	37	32	33

(continued)

$\sum$Fe can introduce significant differences in the estimated compositions of the parental liquids, notably Mg#. For a given lava, increasing $Fe^{3+}/\sum Fe$ from 0·1 to 0·2 would result in a decrease of about 1·5 wt % MgO for the primary melts, ~60°C for the melting temperature and mantle potential temperature, and ~4 kbar for the melting pressure. K_D values increase slightly with increasing pressure (e.g. Putirka, 2005, 2008) and melt composition (Tamura *et al.*, 2000; Herzberg & O'Hara, 2002) (typically within the range of 0·30–0·35). For the given original basalts, increasing K_D from 0·30 to 0·33 would result in an increase of about 2 wt % MgO for the primary magma,

Table 6: Continued

Starting sample:	212B2	QB013	QB012	QB014	II2B-2	HN9907	HN27	HN64	HN97
Reference:	F04	F04	F04	F04	F04	F04	F92	F92	F92
Rock type:	QT	QT	QT	AB	AB	QT	QT	QT	QT
Olivine add (%):	19	25	25	24	24	19	24	24	22
NiO (wt %):		0·28	0·25				0·3	0·3	0·36
wt %									
SiO_2	48·51	46·88	45·3	46·17	46·61	47·96	46·23	45·58	47·06
TiO_2	1·76	2·02	2·07	2·04	2	1·91	2·07	2·2	2·16
Al_2O_3	11·45	10·85	10·93	10·47	10·74	11·1	10·91	10·67	10·55
FeO	9·81	10·83	11·01	10·85	10·6	10·04	10·6	10·78	10·62
MnO	0·12	0·11	0·11	0·12	0·12	0·23	0·14	0·14	0·13
MgO	16·17	17·73	17·97	17·81	17·42	16·52	17·36	17·66	17·49
CaO	7·62	7·88	9·22	8·14	8·16	7·86	8·01	7·67	7·15
Na_2O	2·3	1·61	1·63	2·03	2·01	2·11	2·28	2·59	2·63
K_2O	1·15	0·96	1·12	1·2	1·19	1·14	1·23	1·04	0·74
Fe_2O_3	0·98	1·03	1·05	1·04	1·02	1	1	1·02	1·01
P_2O_5	0·33	0·47	0·46	0·5	0·47	0·38	0·46	0·52	0·44
H_2O^1		1·42	1·42	1·45			1·51	1·22	0·49
H_2O^2	1·5	1·24	1·46	1·56	1·54	1·49	1·6	1·35	0·96
F (%)	17	16	13	15	15	16	16	15	18
P_f^1	22·7	28	32·2	31·8	29·5	24·3	31	35	29·5
P_f^2	18·3	25·2	31·9	28	25·7	20·2	27	30·2	24·2
P_f^3	19·7	26·8	33·7	29·9	28	22·1	29·6	32·5	26
P_f^4	20·6	23·6	25·6	26·2	24·8	21·4	26	28·8	25·5
P_f^5	20·3	25·9	30·9	29	27	22	28·4	31·6	26·3
SD	1·8	1·9	3·6	2·4	2·1	1·7	2·3	2·7	2·3
P_i	31	34·9	35·1	34·9	34·8	32·1	33·6	34·6	35·9
T^1	1447	1479	1482	1491	1484	1456	1481	1502	1496
T^2	1469	1518	1537	1526	1513	1481	1515	1528	1511
T^3	1455	1514	1543	1527	1510	1470	1513	1531	1507
T^4	1457	1504	1521	1515	1502	1469	1503	1520	1505
SD	11	21	34	20	16	13	19	16	8
T_p^1	1488	1524	1529	1526	1517	1497	1516	1522	1519
T_p^2	1532	1587	1595	1590	1577	1545	1574	1585	1579
T_p^3	1510	1571	1581	1574	1559	1524	1556	1568	1562
T_p^4	1460	1537	1551	1538	1519	1477	1519	1533	1521
T_p^5	1575	1588	1503	1562	1582	1581	1548	1522	1611
T_p^6	1513	1561	1552	1558	1551	1525	1543	1546	1558
SD	44	29	37	26	31	41	25	29	40

H_2O^1 and H_2O^2 water contents in primary melts were estimated by fractionation correction of Ce and K_2O (equilibrium with $Fo_{90·7}$ olivines), respectively. F, degree of melting, estimated by equation A2 of Putirka *et al*. (2007). P_f^1 to P_f^5 are effective melting pressures in kbar. P_f^1 is as defined by Lee *et al*. (2009); P_f^2 as defined by Albarède (1992); P_f^3 as defined by Haase (1996); P_f^4 as defined by equation 42 of Putirka (2008); P_f^5 is the average of P_f^1 to P_f^4. SD, standard deviation. P_i is the initial melting pressure by Putirka *et al*. (2007) in kbar. T^1 to T^4 are the melting temperatures (°C) of the melt segregation: T^1 is according to equation 14 of Putirka (2008); T^2 according to Albarède (1992); T^3 according to Lee *et al*. (2009). T_p^1 to T_p^6 are the mantle potential temperatures in °C: T_p^1 to T_p^3 were estimated using the MgO contents in the primary melts following Herzberg *et al*. (2007), McKenzie & Bickle (1988) and Langmuir *et al*. (1992), respectively; T_p^4 is defined by FeO contents in the primary melt according to equation 12 of Kelley *et al*. (2006); T_p^5 is estimated following Putirka (2005); T_p^6 is the average of T_p^1 to T_p^5. Sources for the starting samples: T, this study; Z10, Zou *et al*. (2010); F04, Fan *et al*. (2004); F92, Flower *et al*. (1992).

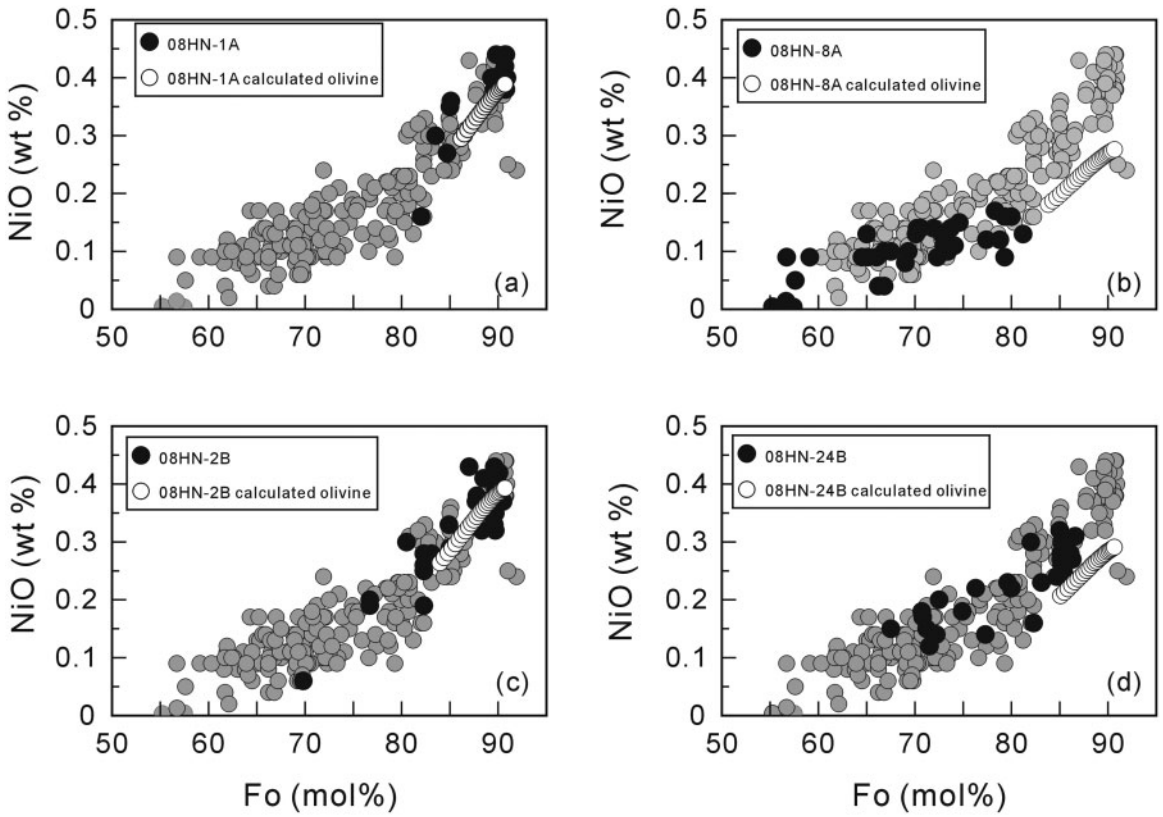

Fig. 13. Variation of NiO vs Fo [100Mg/(Fe^{2+} + Mg)] for measured olivines (black filled circles) and calculated equilibrium olivines (open circles) for four basalt lavas. The calculated olivines were determined from the bulk composition of each lava, as described in the text. Grey symbols show all the measured olivine compositions from the Hainan basalts. Measured olivine compositions overlap those of the calculated equilibrium olivines (e.g. 08HN-1A, 08HN-2B and 08HN-24B). Although the measured olivine compositions are more iron-rich than calculated equilibrium olivines (e.g. 08HN-8A), the trends of NiO vs Fo defined by measured olivines extend towards or pass through the calculated equilibrium olivines. The calculated equilibrium olivine compositions fall within the distribution of all measured olivines from the Hainan basalts.

~5 kbar for melting pressures, ~40°C for melting temperature, and ~100°C for mantle potential temperature. Thus, the net effect of variations in $Fe^{3+}/\sum Fe$ and K_D are negligible. Typical mantle Mg# [Mg# = Mg/(Mg + Fe^{2+}) molar ratio] values are 89–90, but the values vary. The maximum Mg# value for the residual mantle of the Hainan basalts can be constrained by the maximum Fo values in phenocrystic olivines. Decreasing mantle Mg# values from 90·7 to 90 would reduce in decreases of about 1·4 wt % for the MgO content of the calculated primary magma, <20°C for melting temperature and mantle potential temperature, and 3 kbar for melting pressure for a given original basalt. Considering the compounded effects of the uncertainties in $Fe^{3+}/\sum Fe$ ratios, K_D values, and mantle Mg#, the final uncertainties are about ±4 kbar for pressure and ±50°C for melting temperature and potential temperatures. This is on a par with calibration errors associated with the thermobarometers used (i.e. ±50–70°C, ±3–5 kbar).

Water (H_2O) content is another factor controlling the melting temperatures and pressure. The H_2O concentrations in the melts were estimated using their primary Ce or K_2O contents (olivine fraction correction), assuming that the Hainan basalts have the same H_2O/Ce ratios of ~200 as oceanic basalts (Herzberg *et al.*, 2007) or H_2O/K_2O ratios of 1·3 like typical Hawaiian tholeiitic magmas (e.g. Wallace & Anderson, 1998). The two methods predict similar H_2O contents for the primary melts of the Hainan basalts, varying in the range of 1·28–1·42 wt %, which is slightly higher than that for typical Hawaiian tholeiitic magmas (0·5–1·0 wt %; Ren *et al.*, 2004). The calculated temperatures listed in Table 6 have the effect of H_2O contents taken into account.

Figure 15 is a plot of the effective melting pressure vs temperature. We find that the temperatures (1420–1530°C) and pressures (18–32 kbar) for the primary melts of the Hainan basalts plot systematically above the dry lherzolite solidus but below the spinel garnet transition (~50–60 km

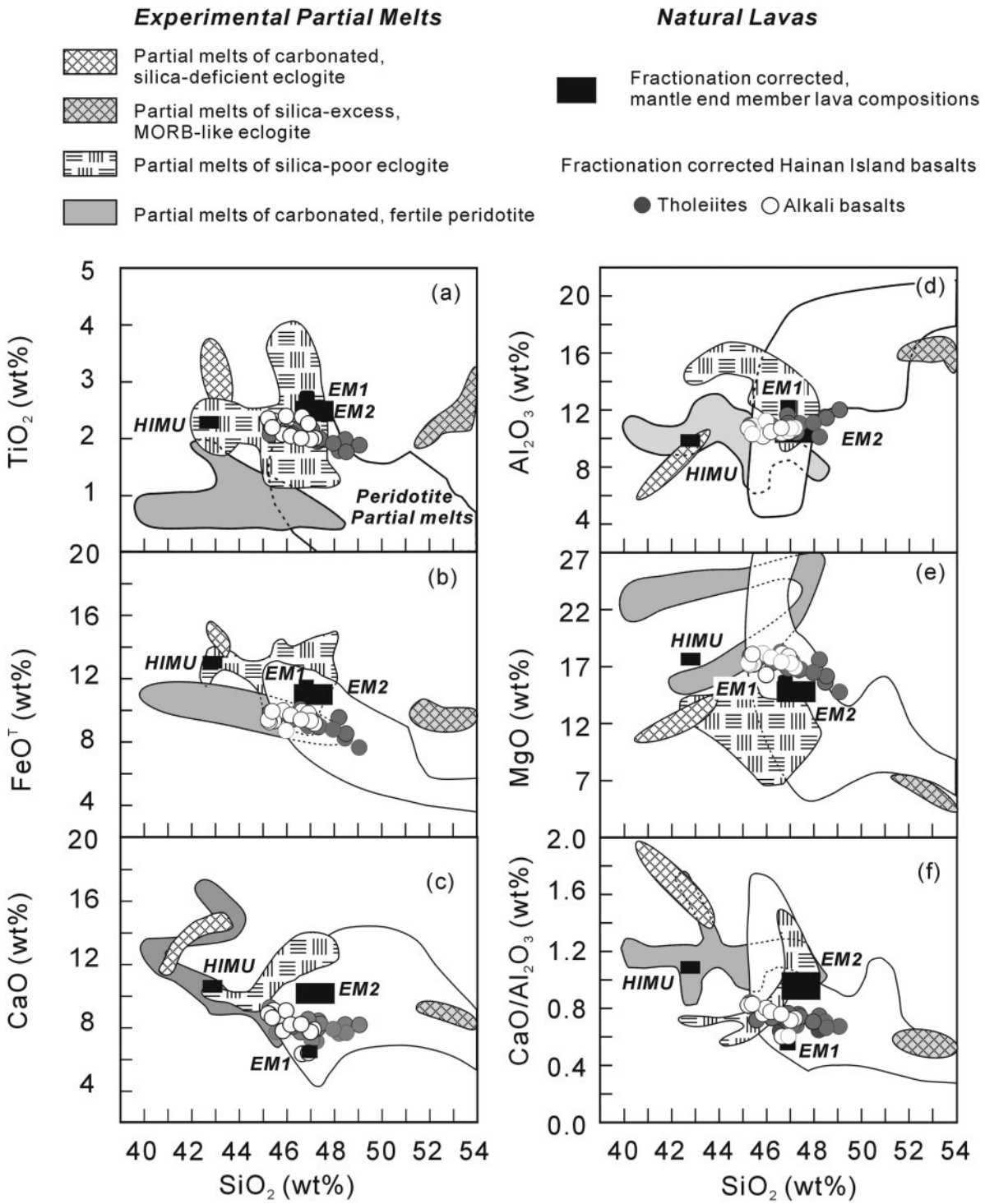

Fig. 14. Comparison of fractionation-corrected Hainan basalts (compositions in equilibrium with $Fo_{90\text{-}7}$, corrected by olivine addition; Table 6), with experimental partial melts. Also shown for reference are the estimated compositions of primary melts of HIMU, EMl, and EM2 mantle end-members. The fields of experiment partial melts and the primary melt compositions for the HIMU, EMl, and EM2 mantle end-members are modified from Dasgupta *et al.* (2010).

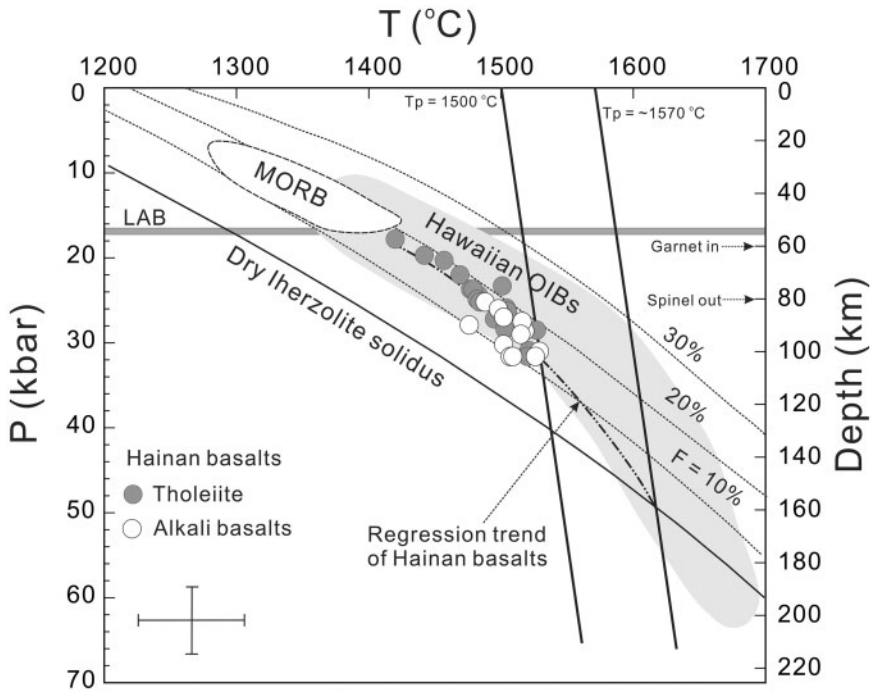

Fig. 15. Temperatures and pressures calculated for the Hainan basalts. The lherzolite solidus and melt fraction isopleths are from Katz *et al.* (2003). Curved lines represent melting adiabats where $F(\%)$ represents the fraction of melting. Near-vertical lines represent solid mantle adiabats. Fields for MORB and Hawaiian OIB are from Lee *et al.* (2009). The lithosphere–asthenosphere boundary (LAB) for Hainan Island is at about 55 km depth as constrained by geophysical data (Wu *et al.*, 2004). Garnet-in and spinel-out occur at ~60 and 80 km in peridotite for a steady-state geotherm (McKenzie & O'Nions, 1991). The pressure (P) is the average of the effective melting pressure (P_f[5] from Table 6), and melting temperature (T) is the average value of T^4 (Table 6).

depth) and the base of the lithosphere (~55 km; Wu *et al.*, 2004). The P_f–T data form an array ($P_f = 0{\cdot}0105 \times e^{0{\cdot}0052T}$, $R^2 = 0{\cdot}81$) that begins at about 18 kbar (~60 km) and intersects the dry peridotite solidus at ~50 kbar or ~160 km. This intersection translates into a mantle potential temperature beneath Hainan Island of ~1500–1600°C, which is ~200°C hotter than average MORB mantle (e.g. Herzberg *et al.*, 2007; Lee *et al.*, 2009) but typical of thermal mantle plumes such as the Hawaiian and Iceland plumes (Putirka, 2005; Herzberg *et al.*, 2007; Lee *et al.*, 2009).

The olivine fractionational correction element contents (SiO_2, TiO_2, MgO, Al_2O_3, and FeO) and ratios (Al_2O_3/TiO_2, Sm/Nd, Zr/Y, and Nb/Y) correlate well with the effective melting pressure (P_f) (Fig. 16). This suggests that melting pressure is one of the controlling factors for the compositions of the primary melts.

Magma source mineralogy

The correlation trends in Fig. 17 could have been affected by post-solidification alteration, assimilation–fractionation–crystallization processes, residual mineral assemblages (source composition), and melting processes. The following lines of evidence show that these trends are mainly controlled by the melting degree and the residual mineral assemblage. First, it has been demonstrated that the effect of crustal contamination on the compositions of the Hainan basalts is insignificant (e.g. Tu *et al.*, 1991; Fan *et al.*, 2004; Zou & Fan, 2010). Second, the contribution of post-magmatic alteration is also negligible, because most of the studied samples are fresh. Third, fractionation crystallization processes could not explain the variations in trends in Fig. 17. After stripping off the effect of olivine fractionation, the Hainan basalts still have large variations in Th content, which would require extremely large-scale fractional crystallization of clinopyroxene and plagioclase (≫50%; dashed-line arrows in Fig. 17). This is inconsistent with the major element compositions. The fractional crystallization trends are also inconsistent with the evolutionary trends of the Hainan basalts (Fig. 17). For example, fractional crystallization processes should produce positive correlations of Ti/Eu–Th and Sc/V–Th, but the Hainan basalts show negative correlations (Fig. 17b). Our analysis shows that the fractionating mineral assemblages in the Hainan basalts were controlled by olivine plus clinopyroxene and plagioclase at a late stage. Such crystal fractionation would have increased the silica and incompatible trace element contents of the remaining melts, resulting in positive correlations of SiO_2–Th, whereas the Hainan

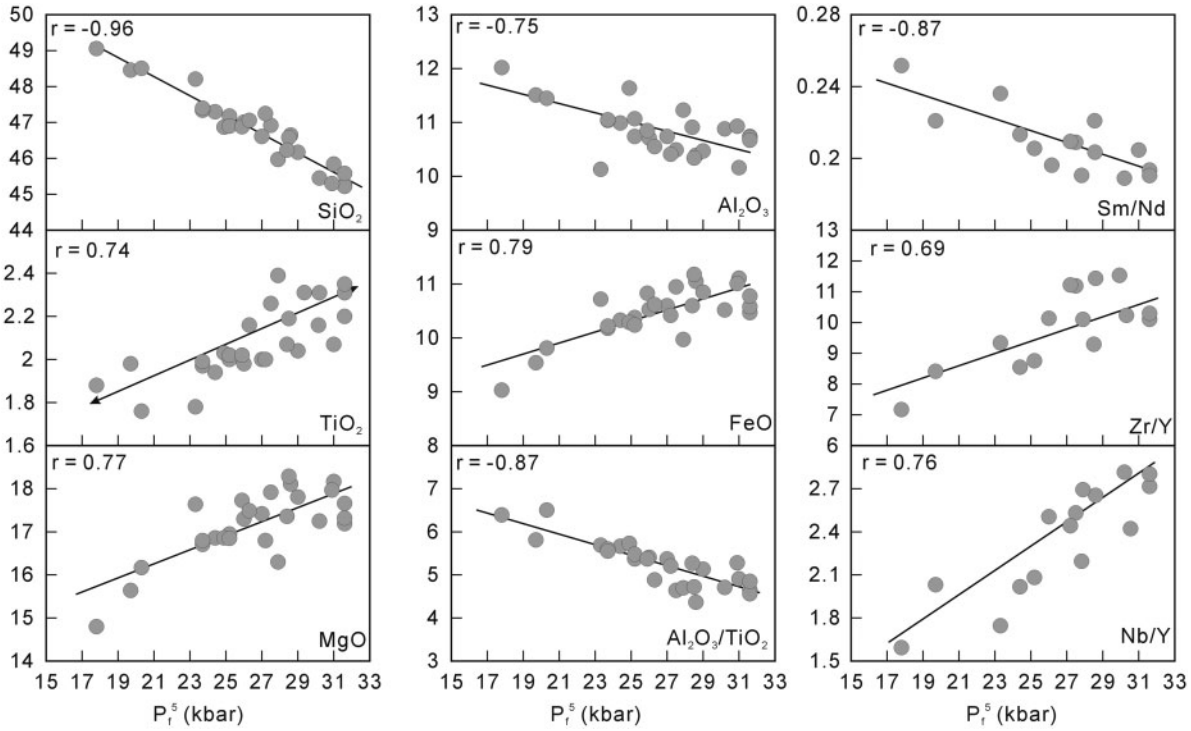

Fig. 16. Plots of major element contents and ratios vs effective melting pressure. The element contents and ratios were adjusted to be in equilibrium with olivine $Fo_{90\cdot7}$. The pressure P_f^5 is from Table 6.

basalts define a negative SiO_2–Th trend. Therefore, the trends shown in Fig. 17 can be used to evaluate the residual source mineralogy.

Garnet and olivine control on compositional variations

Thorium contents (adjusted to be in equilibrium with olivine $Fo_{90\cdot7}$) were employed as an index of the degree of melting (e.g. Frey *et al.*, 2000; Ren *et al.*, 2004). The positive correlations of Tb/Yb–Th and negative correlation of Lu/Yb–Th in tholeiites and low-Th (<4 ppm) alkali basalts (Fig. 17a), require bulk solid/melt $D_{Tb/Yb}<1$ and $D_{Yb/Lu}<1$. Because the experimentally determined $D_{Tb/Yb}$ and $D_{Yb/Lu}$ ratios for clinopyroxene/melt, amphibole/melt and phlogopite/melt partitioning are near unity (e.g. LaTourrette *et al.*, 1995; Dalpé & Baker, 2000; Adam & Green, 2006), these phases cannot effectively fractionate Tb from Yb. In contrast, it is well established that $D_{Tb/Yb}$ ratios for garnet/melt partitioning are as low as 0·23 and $D_{Yb/Lu}$ ratios are <1 (e.g. van Westrenen *et al.*, 2000; Adam & Green, 2006). Therefore, the correlations between Tb/Yb, Lu/Yb and Th reflect the control of residual garnet. None the less, three high-Th (>4 ppm) alkali basalt samples have near constant Tb/Yb and Lu/Yb ratios (Fig. 17a), suggesting the presence of clinopyroxene (and/or amphibole, phlogopite) in their generation.

The high-Th alkali basalts have near constant Sc/V ratios whereas the Sc/V ratios in low-Th alkali basalts and tholeiites correlate negatively with Th (Fig. 17b). This implies that $D_{Sc/V}$ is nearly unity for the high-Th alkali basalts, but $D_{Sc/V}$ is >1 for low-Th alkali basalts and tholeiites. Experimentally determined $D_{Sc/V}$ values for clinopyroxene/melt, garnet/melt, and amphibole/melt are nearly unity, but >2 for olivine/melt (Geochemical Earth Reference Model: http://earthref.org/GERM). Thus, olivine is most probably a predominant phase in the residual mineral assemblage during the generation of the tholeiites and most alkali basalts (low-Th) in Hainan.

The effect of residual K-bearing minerals on K, Rb, Sr and Ba

Amphibole and phlogopite are the major hosts for K, Rb, Sr, and Ba, which could have an effect on the concentrations and related ratios of these elements in equilibrium melts (e.g. Class & Goldstein, 1997; Yang *et al.*, 2003). The following evidence suggests the presence of residual amphibole and phlogopite in the source during the generation of the Hainan basalts.

First, the tholeiites and low-Th alkali basalts exhibit broad negative correlations of Sr/Ce and Sr/Nd with Th (Fig. 17a), suggesting that $D_{Sr/Ce}$ and $D_{Sr/Nd}$ are >1. Experimental work shows that $D_{Sr/Ce}$ and $D_{Sr/Nd}$ for garnet/melt are <1 (e.g. Hauri *et al.*, 1994; Gaetani *et al.*, 2003; Bennett *et al.*, 2004). Although experimentally determined values of $D_{Sr/Nd}$ for clinopyroxene/melt range from

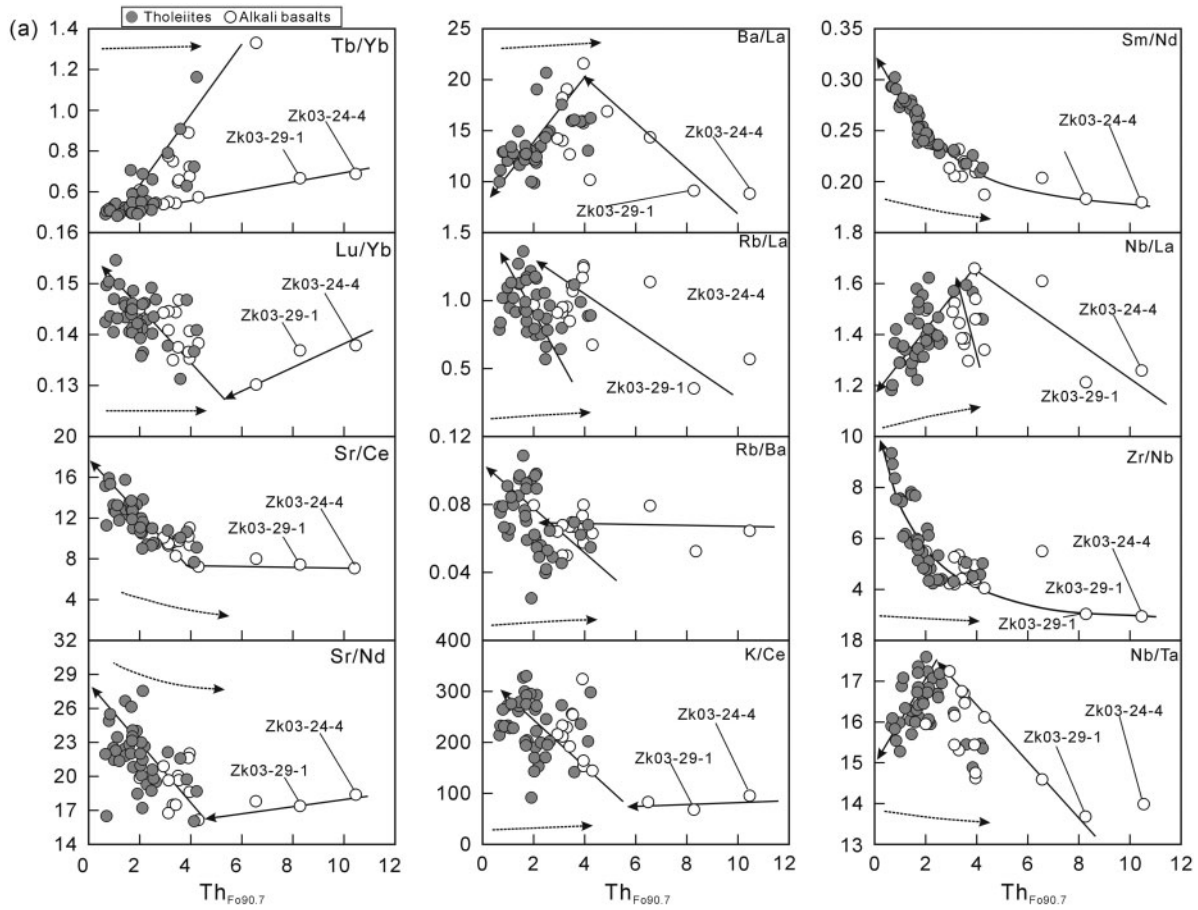

Fig. 17. (a) Abundance ratios of incompatible elements vs concentrations of Th adjusted to be in equilibrium with $Fo_{90\cdot7}$ for the Hainan basalts. (b) Abundance ratios (Zr/Hf, Zr/Sm, Zr/Tb, Ti/Eu and Sc/V) and major and trace element (SiO_2, TiO_2, Al_2O_3, CaO, K_2O, Sc and Zr) contents vs Th content for the Hainan basalts. The element contents (SiO_2, TiO_2, Al_2O_3, CaO, K_2O, Sc, Zr and Th) were adjusted to be in equilibrium with $Fo_{90\cdot7}$. The continuous-line arrows indicate the trends of element contents and ratios with respect to Th. The dashed-line arrows indicate the effect of 50 wt % fractionation of 70% clinopyroxene + 30% plagioclase on the melt compositions. The partition coefficients are from Supplementary Data Appendix Table R2.

<1 ($0{\cdot}4 \pm 0{\cdot}2$; Blundy *et al.*, 1998) to ≥1 (Bennett *et al.*, 2004; Adam & Green, 2006), all available experimental data show $D_{Sr/Ce}$ <1 for clinopyroxene/melt (http://earthref.org/GERM). Thus, residual garnet and/or clinopyroxene could not have produced these trends. On the other hand, Yang *et al.* (2003) showed that the relatively high compatibility of Sr relative to Ce and Nd signifies the presence of residual K-bearing minerals such as phlogopite and/or amphibole in Hawaiian basalts.

Second, the tholeiites define a broad positive correlation of Ba/La vs Th and negative correlations of Rb/La, Rb/Ba and K/Ce with Th (Fig. 17a), indicating $D_{Ba} < D_{La} < D_{Rb}$ and $D_K > D_{Ce}$. The alkali basalts define broad negative correlations of Ba/La and Rb/La with Th and nearly constant ratios of Rb/Ba, indicating $D_{Ba} \approx D_{Rb} > D_{La}$. The K/Ce ratios in the high-Th alkali basalts are nearly constant and in most alkali basalts (low-Th alkali basalts) correlate negatively with Th. These trends suggest $D_K \geq D_{Ce}$ for the alkali basalts, a diagnostic indicator of the presence of residual amphibole and/or phlogopite in the mantle source (e.g. Class & Goldstein, 1997; Yang *et al.*, 2003).

Rb usually shows incompatible behavior in calcic amphibole but Dalpé & Baker (2000) found that it might be also slightly compatible ($D_{Rb} = 1{\cdot}04$), whereas Ba is highly incompatible in amphibole (Tiepolo *et al.*, 2007). The experimentally determined $D_{Rb/Ba}$ for amphibole/melt in some cases is >1 (e.g. Brenan *et al.*, 1995; LaTourrette *et al.*, 1995; Dalpé & Baker, 2000; Adam & Green, 2006). However, both Ba and Rb usually are strongly compatible in phlogopite with $D_{Ba} = 3{\cdot}3$–$3{\cdot}7$ and $D_{Rb} = 2{\cdot}5$–6 (e.g. LaTourrette *et al.*, 1995; Foley *et al.*, 1996). Thus, a bulk $D_{Ba} < D_{Rb}$ indicates that the residual K-bearing mineral for the tholeiites is amphibole. A bulk $D_{Ba} \approx D_{Rb} > D_{La}$ implies that the K-bearing residual phase for the alkali basalts is most probably phlogopite.

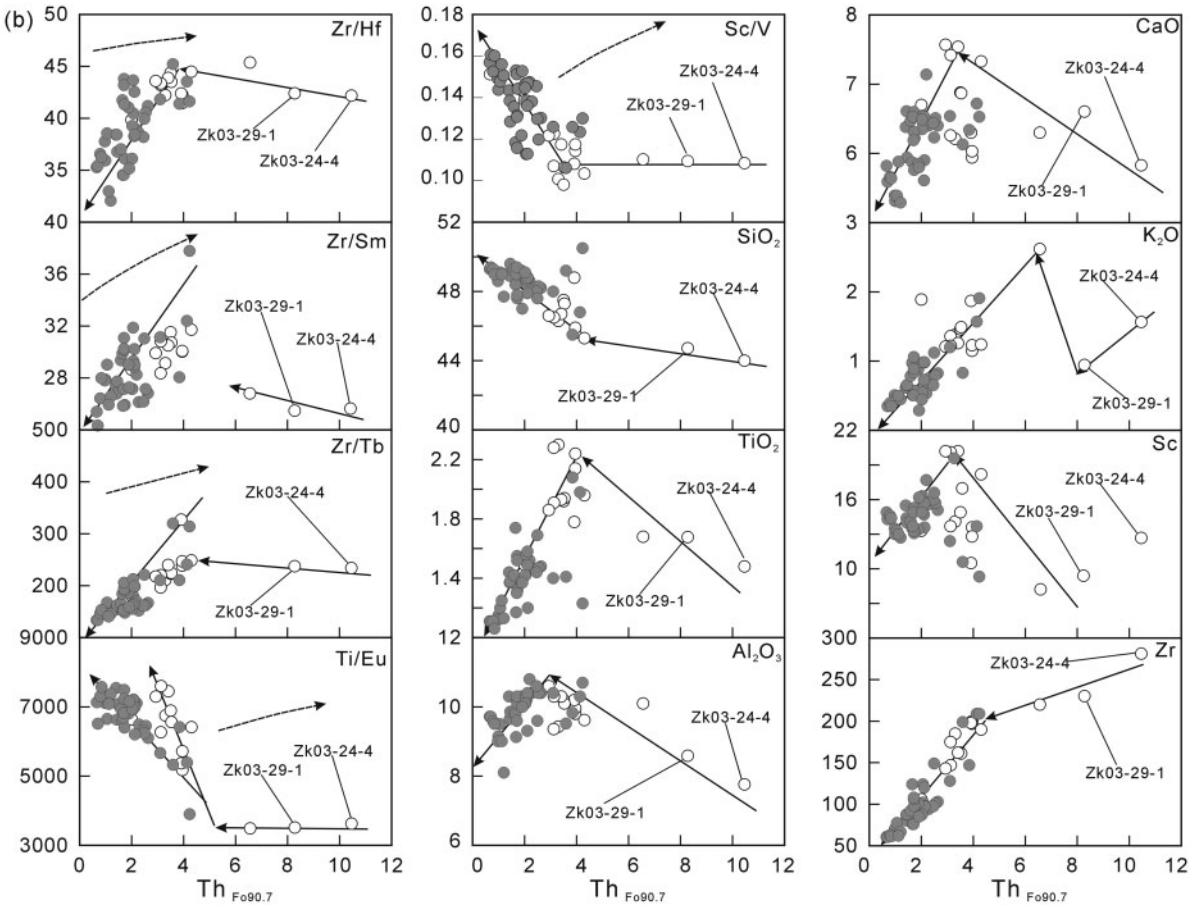

Fig. 17. Continued.

Variations of HFSE: implications for source characteristics

Nb/La, Zr/Hf, Zr/Sm and Zr/Tb ratios in the tholeiites are positively correlated with Th contents, whereas Zr/Nb and Ti/Eu ratios are inversely correlated with Th content (Fig. 17). In addition, Hf/Sm ratios remain constant with falling Th (not shown). These trends imply $D_{Nb} < D_{La}$, $D_{Nb} < D_{Zr} < D_{Hf} \sim D_{sm} < D_{Tb}$ and $D_{Ti} > D_{Eu}$, similar to the pattern for typical OIB (e.g. David *et al.*, 2000).

The positive correlations of Zr/Hf vs Th and Nb/Ta vs Th in the tholeiites (Fig. 17b) indicate a bulk $D_{Zr/Hf} < 1$ and $D_{Nb/Ta} < 1$. This is a typical characteristic of partial melts derived from predomintly peridotitic sources (e.g. David *et al.*, 2000; Pfänder *et al.*, 2007).

The increasing evidence suggests the presence of residual garnet during the generation of the alkali basalts. First, the alkali basalts have nearly constant Zr/Hf ratios (42–45) with falling Th from about 11 to 4 ppm (Fig. 17b), implying a bulk $D_{Zr/Hf} \approx 1$. In the experiments of Hauri *et al.* (1994) and Van Westrenen *et al.* (1999), Zr and Hf are compatible in eclogitic garnet with $D_{Zr/Hf} \geq 1{\cdot}5$. On the other hand, the calculated bulk $D_{Zr/Hf}$ values are about 0·3–0·4 for peridotitic sources using the partition coefficients of Horn *et al.* (1994), Salters & Longhi (1999), Salters *et al.* (2002) and McDade *et al.* (2003), and typical modal proportions of the mantle phases (in the garnet and spinel stability fields) after Kelemen *et al.* (2004). Therefore, the nearly unity value of $D_{Zr/Hf}$ suggests the likely presence of residual eclogitic garnet in the source of Hainan basalts that elevated the $D_{Zr/Hf}$ value from that of a peridotitic source. Second, the alkali basalts define a negative correlation of Nb/Ta vs Th (Fig. 17a), implying a bulk $D_{Nb/Ta} > 1$. This is a typical characteristic of an eclogitic source because $D_{Nb/Ta}$ for eclogitic garnet (grossular-rich garnet) is >1, with $D_{Nb/Ta}$ values ranging between about 1·2 and 2·0 (e.g. Stalder *et al.*, 1998; van Westrenen *et al.*, 1999; Klemme *et al.*, 2002; Pertermann *et al.*, 2004). Third, the alkali basalts also exhibit negative correlations of Nb/La vs Th (Fig. 17a), indicating a bulk $D_{Nb/La} > 1$. Experimental data show that eclogitic garnet has $D_{Nb/La} > 1$, with $D_{Nb/La}$ values ranging from 1·3 to 7·5 (e.g. Van Westrenen *et al.*, 1999; Pertermann *et al.*, 2004). HFSE are also compatible in rutile, whereas the

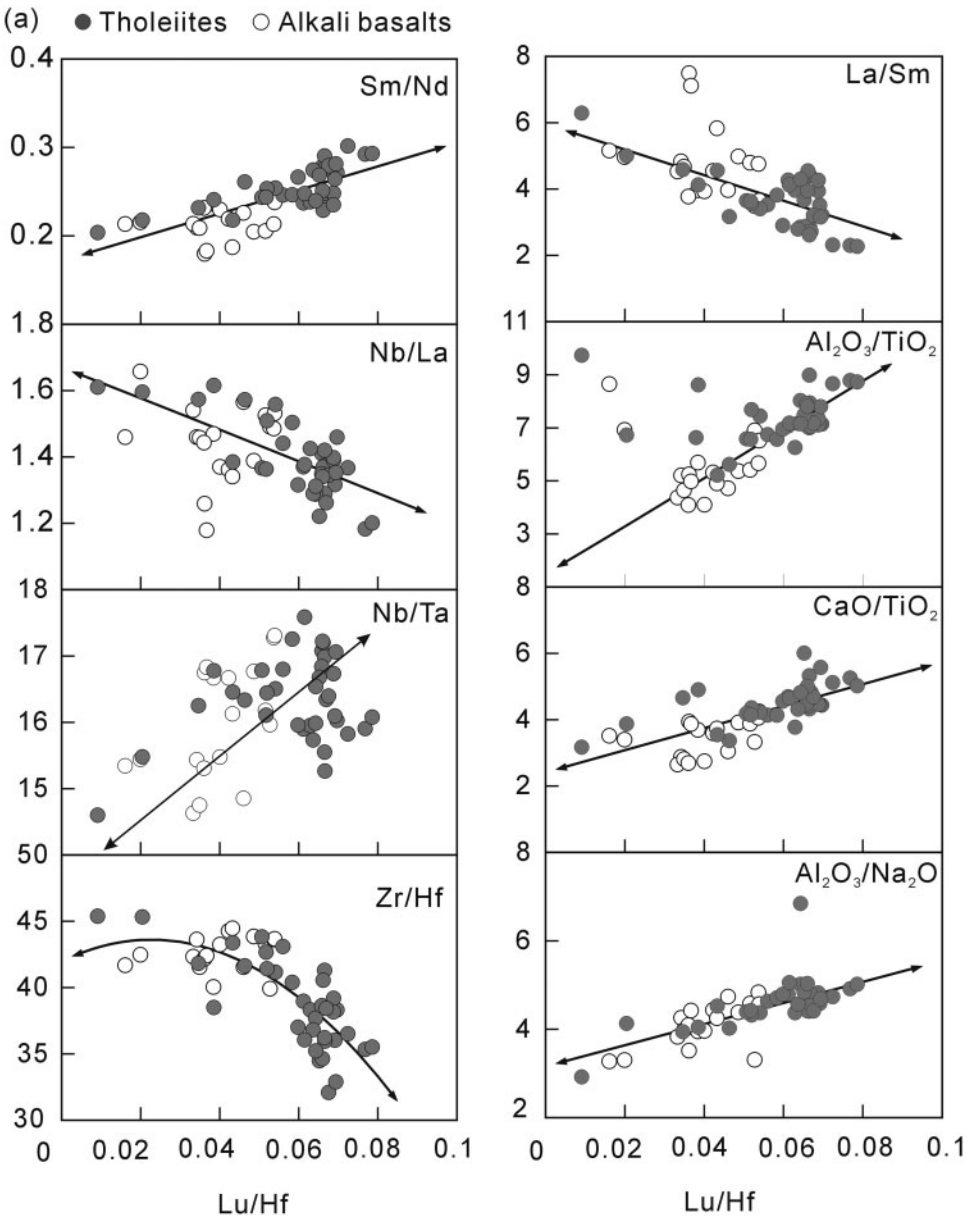

Fig. 18. Major and trace element ratios vs (a) Lu/Hf and (b) Sm/Nd for the Hainan basalts.

LREE are highly incompatible (e.g. Schmidt *et al.*, 2004; Klemme *et al.*, 2005; Xiong *et al.*, 2005). A small amount of rutile could cause strong fractionation of Nb from La. A bulk $D_{Nb/La}$ >1 thus suggests the presence of residual eclogitic garnet and possibly rutile in the generation of alkali basalts.

In summary, the residual source region for the Hainan tholeiites was dominated by olivine with the involvement of garnet and possibly amphibole, whereas the source region for the alkali basalts was dominated by clinopyroxene, phlogopite, and eclogitic garnet, with the possible involvement of rutile (i.e. a typical garnet-pyroxenite or eclogite lithology).

Characterizing the source region

Excluding crustal contamination, the Lu/Hf–*X* and Sm/Nd–*X* trends (Figs 18 and 19) indicate that generation of the Hainan basalts may have involved two end-member melts. The correlations of silica contents (corrected for olivine fractionation) with element ratios further suggest that the two end-members are high- and low-silica melts (Fig. 20a). The trends shown in Figs 17–20 were employed

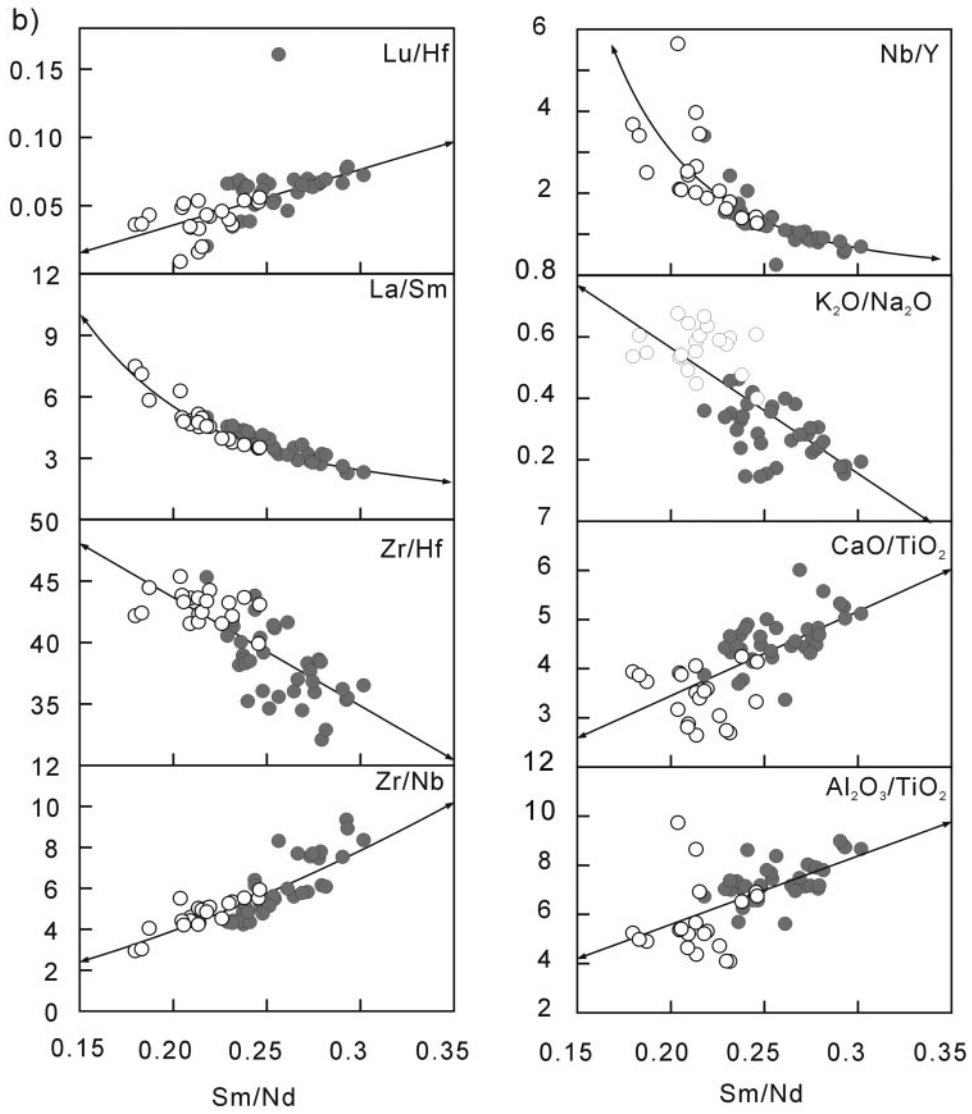

Fig. 18. Continued.

to estimate the composition of the high- and low-silica melts (Table 7). The low- and high-silica melts probably represent the end-members of the alkali basalts and tholeiites in the Hainan province, respectively. The plots of effective P_f versus estimated primary major element and trace element ratios from samples with MgO > 9·0 wt % and CaO > 8·0 wt % also indicate two end-members (Fig. 16). One end-member is characterized by low P_f with high SiO_2, Al_2O_3, Al_2O_3/TiO_2 and Sm/Nd, and low TiO_2, FeO, Zr/Y and Nb/Y, which is similar to the high-silica melt (Table 7 and Figs 18–20). The other is characterized by high P_f with low SiO_2, Al_2O_3, Al_2O_3/TiO_2 and Sm/Nd, and high TiO_2, FeO, Zr/Y and Nb/Y, which is similar to the low-silica melt (Table 7 and Figs 18–20).

The low- and high-silica end-member melts can be produced by partial melting of (1) peridotite at different degrees of partial melting (e.g. McKenzie & O'Nions, 1991) or (2) mixture of a mafic component and a normal mantle peridotite (e.g. Kogiso *et al.*, 2004). Partial melting of a uniform mantle source cannot generate the kinks in the trends of K/Ce, Zr/Hf, Nb/Ta, Al_2O_3, Zr, Sc, CaO, TiO_2 and SiO_2 vs Th (Fig. 17) and Sm/Nd–*X* and Lu/Hf–*X* (Figs 18 and 19). Thus, generation of the Hainan basalts requires partial melting of a heterogeneous mantle source. The most pronounced characteristics of the Hainan tholeiites are the significant positive Sr anomalies (Sr/Sr* = 1·0–1·6, mostly >1·1), whereas the alkali basalts display insignificant Sr anomalies (Sr/Sr* = 0·8–1·1).

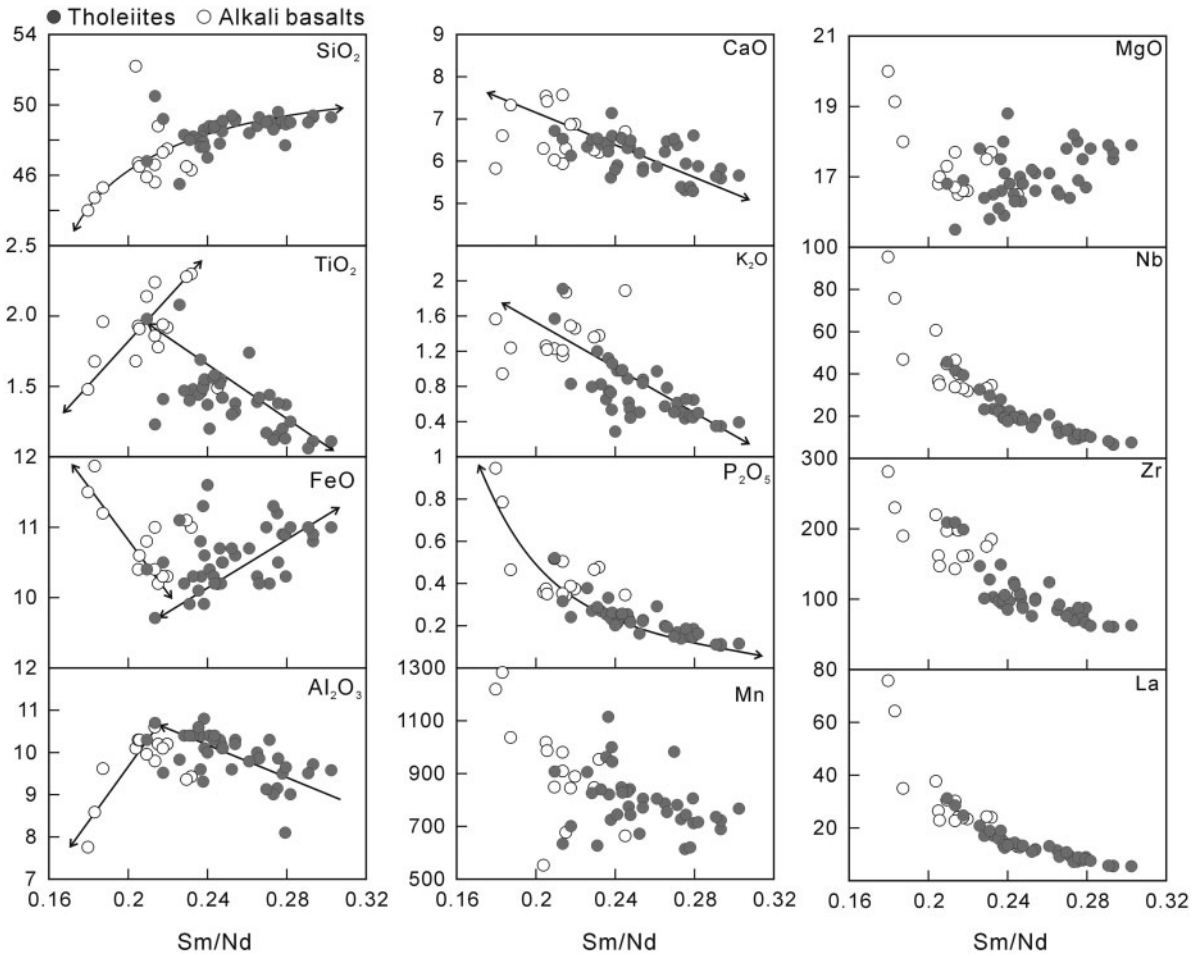

Fig. 19. Olivine fractionation-corrected major and trace element contents (in equilibrium with $Fo_{90\cdot7}$) vs Sm/Nd.

The tholeiites and alkali basalts exhibit correlations of Sr/Sr* with SiO_2 (adjusted to equilibrium olivine $Fo_{90\cdot7}$), Lu/Hf, La/Sm, Sm/Nd, Sr/Ce, Sr/Nd, Al_2O_3/TiO_2, and CaO/TiO_2 (Fig. 20a). The trends suggest that the significant positive Sr anomalies reflect the characteristics of their source region. Positive Sr anomalies are a typical characteristic of oceanic gabbro, which is a distinctive component in recycled oceanic crust (up to 50%; Stracke *et al.*, 2003). Experimental and olivine-hosted melt inclusion studies have shown that positive Sr anomalies coupled with saturation to oversaturation in silica in the melt is a diagnostic feature of recycled oceanic gabbro in the source of plume-related magmas (e.g. Sobolev *et al.*, 2000; Kogiso *et al.*, 2003; Yaxley & Sobolev, 2007; Stroncik & Devey, 2011). Thus, the significant positive Sr anomalies coupled with silica-saturated to -oversaturated characteristics in the Hainan tholeiites strongly suggests the presence of recycled oceanic gabbro in the source of the tholeiites. However, the experimental study of Yaxley & Sobolev (2007) showed that partial melts of oceanic gabbro and eclogite derived from oceanic gabbro are highly siliceous dacitic melts (up to 61–65 wt % SiO_2), similar to partial melts of MORB-like eclogites (Fig. 14). Therefore, these melts alone cannot satisfy the estimated primary melt composition of the tholeiites (Fig. 14). Furthermore, the inferred residual mineral assemblages indicate that the source of the tholeiites should be dominated by peridotite. Thus, we prefer a mixture of predominantly mantle peridotite with some recycled oceanic crust as the source for the tholeiites. The nature of the estimated primary melt compositions is consistent with such a conclusion. The estimated primary melts are similar to those of EM1- and EM2-type OIB (Fig. 14), which have been demonstrated to be produced by partial melting of a mixture of garnet-bearing mafic rock with normal mantle peridotite (e.g. Hofmann, 1997; Hirschmann *et al.*, 2003; Kogiso *et al.*, 2003, 2004).

The following evidence suggests that the source region of the alkali basalts most probably contains silica-poor eclogites (or garnet pyroxenite). First, by comparison

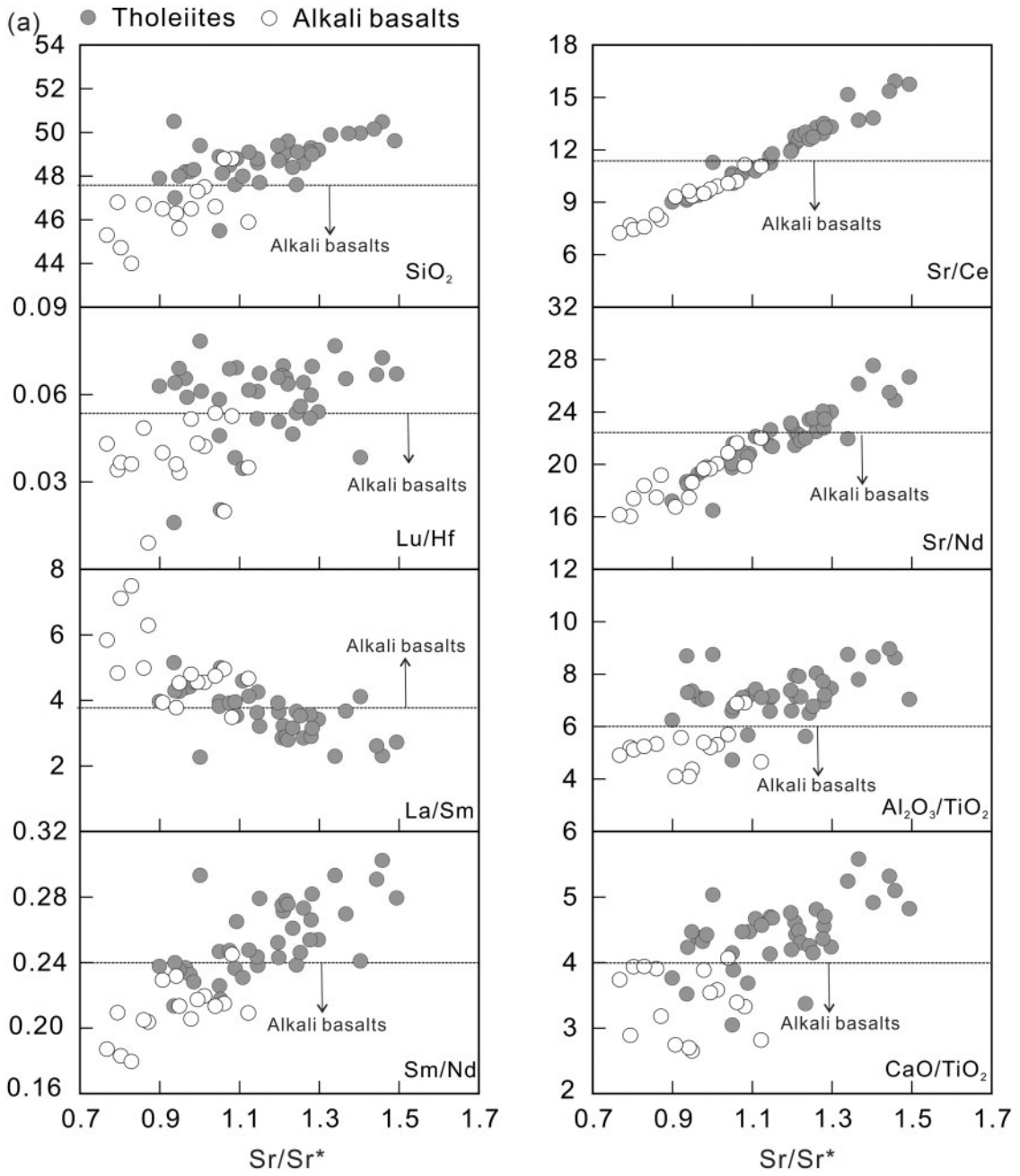

Fig. 20. (a) Abundance ratios and SiO_2 vs Sr/Sr*. $Sr^* = Sr_N/(Ce_N \times Nd_N)^{0.5}$ (primitive mantle normalized values). (b) Abundance ratios vs SiO_2 for the Hainan basalts. The SiO_2 contents were adjusted to be in equilibrium with $Fo_{90.7}$.

with experimental melt compositions, the estimated primary melts for the alkali basalts plot within or close to the field defined by partial melts of silica-poor eclogite (Fig. 14). Second, the residual mineral assemblage of the alkali basalts most probably contains typical eclogite (or garnet pyroxenite) minerals, such as clinopyroxene, phlogopite and eclogitic garnet, and possibly rutile. The predominance of residual olivine, however, suggests that the source for most of the alkali basalts should be dominated by peridotite. Thus, a mixture of peridotite with K-bearing eclogite (or garnet pyroxenite) is proposed to be the source for most of the alkali basalts. Only a few high-Th alkali basalts may have been produced mainly by melting of low-silica eclogite (or garnet pyroxenite).

The presence of recycled garnet-bearing mafic rocks in the source region of the Hainan basalts is further supported by their high Fe/Mn and Zn/Fe ratios. There are

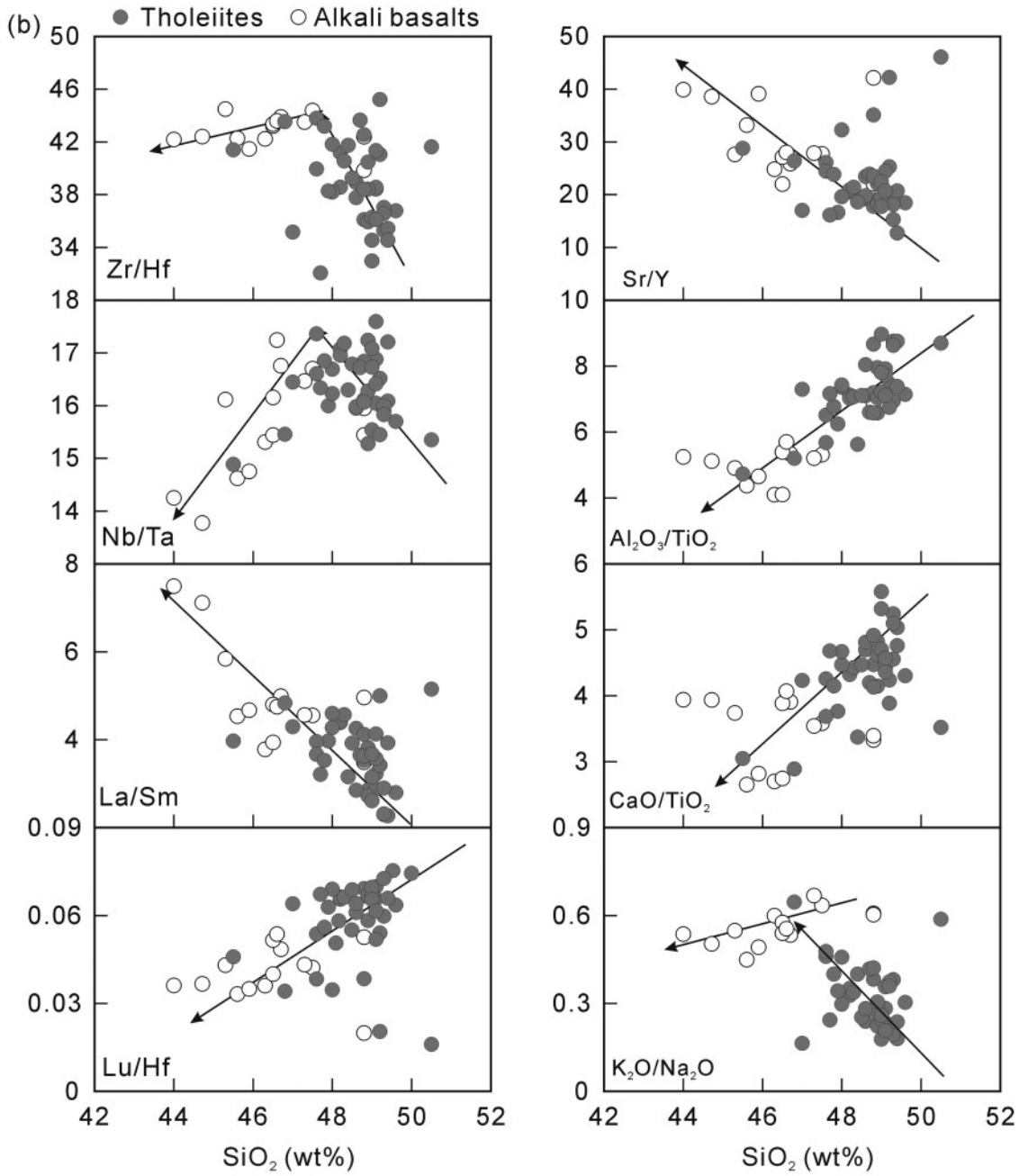

Fig. 20. Continued.

two factors that control the Fe/Mn ratio: crystal fractionation (olivine and clinopyroxene) and source composition. Olivine fractionation reduces the Fe/Mn ratio in the residual melts (Liu *et al.*, 2008, and references therein). Although clinopyroxene fractionation increases the Fe/Mn ratio in the residual melt, as $D_{Fe/Mn}$ between clinopyroxene and basaltic melt is <1, fractional crystallization of clinopyroxene cannot satisfy the observed high Fe/Mn ratios in the Hainan basalts. On the other hand, there is evidence suggesting that the high Fe/Mn ratios record the contribution of source components rather than the effects of magmatic differentiation. First, clinopyroxene fractionation should produce a positive correlation of Fe/Mn vs Yb in the residual melts, whereas a negative trend is

Table 7: Estimated compositions for the low- and high-silica melts

	Low-silica melt	High-silica melt
SiO_2 (wt %)	45	>49
TiO_2 (wt %)	2·5	1·5
FeO (wt %)	11	9·8
Al_2O_3 (wt %)	10·7	11·5
Th (ppm)	>5	<1
Sm/Nd	0·18	0·3
Lu/Hf	0·01	>0·06
Nb/Ta	14	18
Sm/Yb	>7	2
Zr/Hf	>42	32
Zr/Y	30	5
Nb/Y	>4	1
Zr/Nb	4	9
La/Sm	6	2
Al_2O_3/TiO_2	4	8
CaO/TiO_2	3·5	5
Al_2O_3/Na_2O	3	5
K_2O/Na_2O	>0·5	<0·3

The concentrations are adjusted to equilibrate with olivine $Fo_{90·7}$. The compositions of low- and high-silica melts are estimated based on trends in Figs 17–20.

observed in the Hainan basalts (Fig. 6c). Second, clinopyroxene fractionation would result in a negative correlation of Fe/Mn vs Mg#, but the Hainan basalts show no such a correlation (Fig. 6d). Third, 50% clinopyroxene crystal fractionation from MORB-like melts with Fe/Mn ratios of 59 (average of MORB with 11–15 wt % MgO; Liu *et al.*, 2008) would only cause an increase in Fe/Mn ratios from 59 to 70, which is still lower than that in the majority of the Hainan basalt samples (Figs 5 and 6).

Experimental studies have shown that high Fe/Mn ratios (>60) in basaltic melts can be generated by partial melting of garnet pyroxenite or hydrous peridotite at high degrees of melting (Liu *et al.*, 2008, and references therein; Fig. 21). Zou & Fan (2010) demonstrated that it would be impossible to produce the Hainan basalts by partial melting of hydrous peridotite. The Fe/Mn ratios in the Hainan basalts are similar to those of partial melts of pyroxenite, but significantly higher than those of partial melts of hydrous and anhydrous peridotites at given MnO contents (Fig. 21). Thus, the high Fe/Mn ratios may be attributed to partial melting of garnet-pyroxenites (eclogites) in the source of the Hainan basalts.

Zn/Fe ratios are also sensitive to the contribution of eclogite and garnet pyroxenite in the generation of OIB (Le Roux *et al.*, 2010). The less-evolved Hainan basalts (Mg# > 60) display relatively high Zn/Fe ratios, with $Zn/Fe \times 10^4$ of about 12 (Fig. 4h), which are significantly higher than average upper mantle values (~8·5; Le Roux *et al.*, 2010). According to Le Roux *et al.* (2010), this characteristic also signifies the presence of eclogite and/or garnet pyroxenite in the source.

Origin of the garnet-bearing mafic component in the source region

Our geochemical data suggest that the garnet-bearing mafic component in the source region of the tholeiites was recycled oceanic crust, including MORB and oceanic gabbros, trapped by an upwelling mantle flow (e.g. a plume). However, the silica-undersaturated characteristics of the alkali basalts suggest that the garnet-bearing mafic component in their source was not directly derived from recycled oceanic crust because direct partial melting of recycled oceanic crust produces silica-saturated to -oversaturated melts (e.g. Kogiso *et al.*, 2003; Sobolev *et al.*, 2005). Figure 15 shows that partial melting occurred below the asthenosphere–lithosphere boundary. Significant ^{230}Th excesses in the Holocene Hainan basalts indicate that they were produced by melting of a mantle source at >75 km depth (Zou & Fan, 2010). Because the asthenosphere–lithosphere boundary is at about 55 km depth here (Wu *et al.*, 2004), the melting event must have occurred within the asthenosphere. Thus, the inferred garnet-bearing mafic component could not have originated from the subcontinental lithospheric mantle. The lack of continental crust-derived signatures (low Nb/La, Nb/U and negative Nb–Ta–Ti anomalies) and long-term enriched isotope characteristics (Zou & Fan, 2010) is inconsistent with an origin from delaminated ancient lower continental crust. Another possibility is that the recycled mafic component was derived from delaminated mafic rocks that were emplaced at the base of the crust by plume magmatism at an earlier stage. The contribution of such a delaminated mafic component would produce silica-saturated to -oversaturated melts in the later stages of the volcanism. This is inconsistent with the fact that late-stage Hainan volcanism is dominated by alkali basalts and there is no clear correlation between age and geochemical signature.

On the other hand, subduction processes (dehydration and partial melting) and interaction of the subducted slab with the surrounding peridotite in upwelling plumes could convert some silica-excess oceanic crust to silica-poor garnet pyroxenite and/or eclogite (e.g. Kogiso *et al.*, 2003). The presence of residual K-bearing minerals, eclogitic garnet, clinopyroxene and rutile indicates that the low-silica garnet-bearing mafic component in the asthenospheric mantle source of the alkali basalts may have originated from interactions between silica-excess recycled oceanic crust and the ambient peridotite in an upwelling

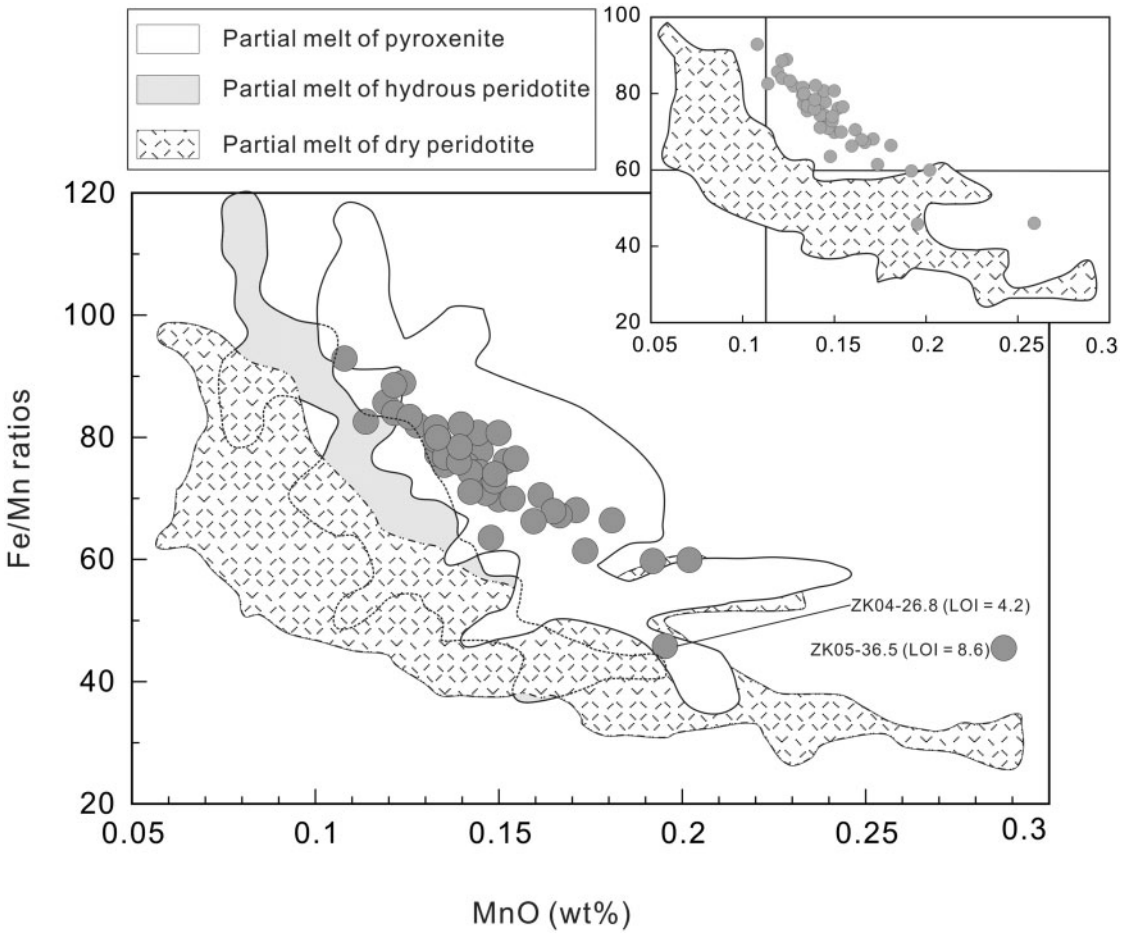

Fig. 21. Variation of Fe/Mn ratios vs MnO contents of the Hainan basalts and basaltic melts formed by partial melting of pyroxenite, dry peridotite and hydrous peridotite. The inset shows that the Hainan basalts have higher Fe/Mn ratios at given MnO contents compared with experimental melts derived by partial melting of dry peridotite, suggesting that such high Fe/Mn ratios in the Hainan basalts could not have been generated only by partial melting of a dry peridotite source. The fields of experimental melts were modified from Liu *et al.* (2008).

mantle plume (e.g. Sobolev *et al.*, 2000, 2005; Yaxley & Sobolev, 2007; Stroncik & Devey, 2011).

Constraints on the Hainan plume model

The high-magnesian olivine phenocrysts ($Fo_{90\text{-}7}$), high mantle potential temperature ($1541 \pm 10^{\circ}C$) and the presence of recycled oceanic crust in the source region consistently argue for a plume-origin model for the Hainan basalts. Zou & Fan (2010) proposed that the enriched Sr–Nd–Pb isotopic signatures of the basalts may have originated from the mantle Transition Zone, or more likely, the lower mantle. The magma supply of the Hainan flood basalt province is $0{\cdot}1$–$0{\cdot}25\,km^3\,a^{-1}$, similar to that of plume-induced continental flood basalt provinces (e.g. Flower *et al.*, 1992). Such an interpreted plume origin for the geochemical and petrological characteristics of the Hainan basalts is consistent with the geophysical observations. The plume model also best explains why the extensive and voluminous late Cenozoic basaltic volcanism in the South China Sea and surrounding regions started after the cessation of the South China Sea opening (e.g. Hoang & Flower, 1998; Ho *et al.*, 2000; Zou & Fan, 2010). It also explains the high mantle potential temperature (~1440°C) estimated for the synchronous Vietnam flood basalt province in the nearby Indochina Block (Hoang & Flower, 1998).

However, the rate of mantle upwelling for the hypothesized Hainan plume, estimated using the ($^{230}Th/^{238}U$) disequilibrium dataset, is $<1\,cm\,a^{-1}$ (Zou & Fan, 2010). This estimated upwelling rate is significantly slower than that for the Hawaiian plume. Thus, if the seismic low-velocity structure indeed represents a mantle plume, it may signify a dying plume (Zou & Fan, 2010). It should be cautioned that the estimated mantle upwelling rate was mainly based on the Holocene alkali basalts. These basalts represent a melting event with a slower rate than the other

events, and consequently may lead to an underestimation of the mantle upwelling rate. Therefore, independent estimates of the mantle upwelling rate, particularly based on the tholeiites, are called for to further test the Hainan plume hypothesis.

The conclusion that the low-velocity structure beneath Hainan Island may indeed represent a thermal mantle plume is provocative because such a plume would potentially provide a rare example of a young mantle plume close to a deep slab subduction zone rather than a lower mantle superplume. Regional and global seismic tomographic studies suggest that the plume-like mantle low-velocity structure beneath Hainan Island sits close to the subduction of the Pacific and Philippine Sea slabs to the east, and the Indian slab to the west (Zhao, 2004, 2007; Huang & Zhao, 2006; Huang *et al.*, 2010; Zhao *et al.*, 2011). This is unusual in that subducting slabs and a potential hotspot occur within about 1000 km of one another (Zhao *et al.*, 2011). Globally, these two geological components are commonly separated by far greater distances (Davaille *et al.*, 2005). Thus, the hypothesized Hainan plume could potentially provide a key insight into the possible interrelation between plumes and slab subduction. The origin of the inferred garnet-bearing mafic component in the source region of the basalts, and the question of whether the source also contains lower mantle materials, will probably bring further insight to this issue. This may be achieved through further in-depth isotopic studies (especially He and Os isotopes)

CONCLUSIONS

New $^{40}Ar/^{39}Ar$ dating indicates that Cenozoic volcanism in Hainan Island started in the late Miocene (about 13 Ma), peaked during the late Pliocene to middle Pleistocene, and terminated in the Holocene.

Geochemical analyses show that crystal fractionation of olivine, clinopyroxene and plagioclase probably occurred during the magmatic evolution of the Hainan basalts. The effect of clinopyroxene fractionation is negligible for samples with MgO >8·5 wt %. Clinopyroxenes are estimated to have crystallized over a wide range of pressures (2–25 kbar) with a dominant pressure range of 10–15 kbar. The clinopyroxene and clinopyroxene–liquid thermometry results reveal that the magma cooled from about 1350°C to 1100°C in the process.

Using the most forsteritic olivine ($Fo_{90·7}$), a constant Fe–Mg exchange partition coefficient $K_D = 0·31$, and the least evolved basaltic samples (MgO > 9·0 wt % and CaO > 8·0 wt %) from Hainan Island, we constrained the primary melt compositions. The estimated melting temperature (T) and effective melting pressure (P_f) are slightly different for the tholeiites and alkali basalts: for the tholeiites, $T = 1420–1520°C$, $P_f = 18–32$ kbar with a weighted average of $23·8 \pm 1·8$ kbar; for the alkali basalts, $T = 1480–1530°C$, $P_f = 25–32$ kbar with a weighted average of $28·3 \pm 1·4$ kbar. The T–P_f array plots systematically above the dry lherzolite solidus and beneath the spinel–garnet transition depth (~50–60 km) and the asthenosphere–lithosphere boundary (~55 km). The P_f–T data form an array that intersects the dry peridotite solidus at about 50 kbar. The mantle potential temperatures for the estimated primary melts range from about 1500 to 1580°C with a weighted average of $1541 \pm 10°C$, which is similar to that of typical thermal mantle plumes.

The geochemical characteristics of the Hainan basalts are hard to reconcile with partial melting of a peridotitic mantle alone. This study suggests that the source for the tholeiites was a mixture of peridotite with a minor recycled oceanic crust component, whereas the source for most of the alkali basalts (Th < 4 ppm) was a mixture of peridotite with a low-silica eclogite (or garnet pyroxenite). Only the minor occurrence of high-Th (>4 pm) alkali basalts may be related to partial melting of low-silica garnet pyroxenite or eclogite.

The high mantle potential temperature and melting pressures, the presence of high-magnesian olivine phenocrysts in the basalts, and the presence of recycled oceanic crust in the source region provide independent support for the Hainan basalts being the manifestation of a thermal mantle plume, a model previously established largely on geophysical observations. The hypothesized Hainan plume could potentially provide a rare example of a young mantle plume closely associated with a deep slab subduction system.

ACKNOWLEDGEMENTS

We thank reviewers Cin-Ty Lee, Zhong-Yuan Ren and Nicholas Schmerr, and editor Gerhard Wörner for their constructive and helpful reviews. We are grateful to Y. H. Ling for help during the field work, G. Q. Hu for assistance in geochemical analyses, L. K. Yang for assistance in $^{40}Ar/^{39}Ar$ dating, and Marion Grange for proofreading.

FUNDING

This work was supported by the National Natural Science foundation of China (grants 40803010 and 40973044) and Australian Research Council (ARC) Discovery Project grant (DP0770228). This is TIGeR (The Institute for Geoscience Research, Curtin University) Publication 265, and contribution 24 from the ARC Centre of Excellence for Core to Crust Fluid Systems.

SUPPLEMENTARY DATA

Supplementary data for this paper are available at *Journal of Petrology* online.

REFERENCES

Adam, J. & Green, T. (2006). Trace element partitioning between mica- and amphibole-bearing garnet lherzolite and hydrous basanitic melt: l. Experimental results and the investigation of controls on partitioning behaviour. *Contributions to Mineralogy and Petrology* **152**, 1–17.

Albarède, F. (1992). How deep do common basaltic magmas form and differentiate? *Journal of Geophysical Research* **97**, 10997–11009.

Asimow, P. D., Hirschmann, M. M. & Stolper, E. M. (1997). An analysis of variations in isentropic melt productivity. *Philosophical Transactions of the Royal Society of London, Series A* **355**, 255–281.

Beattie, P., Ford, C. & Russell, D. (1991). Partition coefficients for olivine–melt and orthopyroxene–melt systems. *Contributions to Mineralogy and Petrology* **109**, 212–224.

Bennett, S. L., Blundy, J. & Elliott, T. (2004). The effect of sodium and titanium on crystal–melt partitioning of trace elements. *Geochimica et Cosmochimica Acta* **68**, 2335–2347.

Blundy, J. D., Robinson, J. A. C. & Wood, B. J. (1998). Heavy REE are compatible in clinopyroxene on the spinel lherzolite solidus. *Earth and Planetary Science Letters* **160**, 493–504.

Brenan, J. M., Shaw, H. F., Ryerson, F. J. & Phinney, D. L. (1995). Experimental determination of trace-element partitioning between pargasite and a synthetic hydrous andesitic melt. *Earth and Planetary Science Letters* **135**, 1–11.

Campbell, I. H. (2007). Testing the plume theory. *Chemical Geology* **241**, 153–176.

Chung, S. L., Cheng, H., Jahn, B. M., O'Reilly, S. Y. & Zhu, B. (1997). Major and trace element, and Sr–Nd isotope constraints on the origin of Paleogene volcanism in South China prior to the South China Sea opening. *Lithos* **40**, 203–220.

Class, C. & Goldstein, S. L. (1997). Plume–lithosphere interactions in the ocean basins: constraints from the source mineralogy. *Earth and Planetary Science Letters* **150**, 245–260.

Cullen, A., Reemst, P., Henstra, G., Gozzard, S. & Ray, A. (2010). Rifting of the South China Sea: new perspectives. *Petroleum Geoscience* **16**, 273–282.

Dalpé, C. & Baker, D. R. (2000). Experimental investigation of large-ion-lithophile-element, high-field-strength-element and rare-earth-element partitioning between calcic amphibole and basaltic melt: the effects of pressure and oxygen fugacity. *Contributions to Mineralogy and Petrology* **140**, 233–250.

Damasceno, D., Scoates, J. S., Weis, D., Frey, F. A. & Giret, A. (2002). Mineral chemistry of mildly alkalic basalts from the 25 Ma Mont Crozier section, Kerguelen Archipelago: constraints on phenocryst crystallization environments. *Journal of Petrology* **43**, 1389–1413.

Dasgupta, R., Jackson, M. G. & Lee, C. T. (2010). Major element chemistry of ocean island basalts—conditions of mantle melting and heterogeneity of mantle source. *Earth and Planetary Science Letters* **289**, 377–392.

Davaille, A., Stutzmann, E., Silveira, G., Besse, J. & Courtillot, V. (2005). Convective patterns under the Indo-Atlantic 'box'. *Earth and Planetary Science Letters* **239**, 233–252.

David, K., Schiano, P. & Allègre, C. J. (2000). Assessment of the Zr/Hf fractionation in oceanic basalts and continental materials during petrogenetic processes. *Earth and Planetary Science Letters* **178**, 285–301.

Fan, Q. C., Sun, Q., Li, N. & Sui, J. L. (2004). Periods of volcanic activity and magma evolution of Holocene in North Hainan Island. *Acta Petrologica Sinica* **20**, 533–544 (in Chinese with English abstract).

Fedorov, P. I. & Koloskov, A. V. (2005). Cenozoic volcanism of southeast Asia. *Petrology* **13**, 352–380.

Flower, M. F. J., Zhang, M., Chen, C. Y., Tu, K. & Xie, G. (1992). Magmatism in the South China Basin: 2. Post-spreading Quaternary basalts from Hainan Island, south China. *Chemical Geology* **97**, 65–87.

Foley, S. F., Jackson, S. E., Fryer, B. J., Greenough, J. D. & Jenner, G. A. (1996). Trace element partition coefficients for clinopyroxene and phlogopite in an alkaline lamprophyre from Newfoundland by LAM-ICP-MS. *Geochimica et Cosmochimica Acta* **60**, 629–638.

Frey, F. A., Clague, D., Mahoney, J. J. & Sinton, J. M. (2000). Volcanism at the edge of the Hawaiian plume: petrogenesis of submarine alkalic lavas from the North Arch Volcanic Field. *Journal of Petrology* **41**, 667–691.

Friederich, W. (2003). The S-velocity structure of the East Asian mantle from inversion of shear and surface waveforms. *Geophysical Journal International* **153**, 88–102.

Gaetani, G. A., Kent, A. J. R., Grove, T. L., Hutcheon, I. D. & Stolper, E. M. (2003). Mineral/melt partitioning of trace elements during hydrous peridotite partial melting. *Contributions to Mineralogy and Petrology* **145**, 391–405.

Garcia, M. O. (1996). Petrography and olivine and glass chemistry of lavas from the Hawaii Scientific Drilling Project. *Journal of Geophysical Research* **101**, 11701–11713.

Haase, K. M. (1996). The relationship between the age of the lithosphere and the composition of oceanic magmas: Constraints on partial melting, mantle sources and the thermal structure of the plates. *Earth and Planetary Science Letters* **144**, 75–92.

Han, J. W. (2009). Geochronology and geochemistry of basalts from Leiqiong, South China and their geodynamic implication. PhD thesis, Guangzhou Institute of Geochemistry (Chinese Academy of Sciences), School of the Chinese Academy of Sciences (in Chinese with English abstract).

Hauri, E. H., Wagner, T. P. & Grove, T. L. (1994). Experimental and natural partitioning of Th, U, Pb and other trace elements between garnet, clinopyroxene and basaltic melts. *Chemical Geology* **117**, 149–166.

Herzberg, C. & O'Hara, M. J. (2002). Plume-associated ultramafic magmas of Phanerozoic age. *Journal of Paleontology* **43**, 1857–1883.

Herzberg, C., Asimow, P. D., Arndt, N., Niu, Y., Lesher, C. M., Fitton, J. G. & Saunders, A. D. (2007). Temperature in ambient mantle and plumes: Constraints from basalts, picrites, and komatiites. *Geochemistry, Geophysics, Geosystems* **8**, doi:10.1029/2006GC001390.

Hirschmann, M. M., Kogiso, T., Baker, M. B. & Stolper, E. M. (2003). Alkalic magmas generated by partial melting of garnet pyroxenite. *Geology* **31**, 481–484.

Ho, K. S., Chen, J. C. & Juang, W. S. (2000). Geochronology and geochemistry of late Cenozoic basalts from the Leiqiong area, southern China. *Journal of Asian Earth Sciences* **18**, 307–324.

Ho, K. S., Chen, J. C., Lo, C. & Zhao, H. I. (2003). ^{40}Ar–^{39}Ar dating and geochemical characteristics of late Cenozoic basaltic rocks from the Zhejiang–Fujian region, SE China: eruption ages, magma evolution and petrogenesis. *Chemical Geology* **197**, 287–318.

Hoang, N. & Flower, M. (1998). Petrogenesis of Cenozoic basalts from Vietnam: implication for origin of a 'diffusive igneous province'. *Journal of Petrology* **39**, 369–395.

Hofmann, A. W. (1997). Mantle geochemistry: the message from oceanic volcanism. *Nature* **385**, 219–229.

Horn, S. F., Foley, S. E., Jackson, G. A. & Jenner, G. A. (1994). Experimentally determined partitioning of high-field strength-elements and selected transition-elements between spinel and basaltic melt. *Chemical Geolology* **117**, 193–218.

Huang, J. & Zhao, D. (2006). High-resolution mantle tomography of China and surrounding regions. *Journal of Geophysical Research* **111**, B09305, doi:10.1029/2005JB004066.

Huang, Z., Wang, L., Zhao, D., Xu, M., Mi, N., Yu, D., Li, H. & Li, C. (2010). Upper mantle structure and dynamics beneath Southeast China. *Physics of the Earth and Planetary Interiors* **182**, 161–169.

Huang, Z. G. & Cai, F. X. (1994). A new approach to the Quaternary volcanicity in the Leiqiong area. *Tropical Geography* **14**, 1–9 (in Chinese with English abstract).

Humayun, M., Qiu, L. & Norman, M. D. (2004). Geochemical evidence for excess iron in the mantle beneath Hawaii. *Science* **306**, 91–94.

Katz, R. F., Spiegelman, M. & Langmuir, C. H. (2003). A new parameterization of hydrous mantle melting. *Geochemistry, Geophysics, Geosyststems* **4**, doi:10.1029/2002GC000433.

Kelley, K. A., Plank, T., Grove, T. L., Stolper, E. M., Newman, S. & Hauri, E. (2006). Mantle melting as a function of water content beneath back-arc basins. *Journal of Geophysical Reseach* **111**, doi:10.1029/2005JB003732.

Kelemen, P. B., Yogodzinski, G. M. & Scholl, D. W. (2004). Alongstrike variation in lavas of the Aleutian island arc: implications for the genesis of high Mg# andesite and the continental crust. In: Eiler, J. (ed.) *Inside the Subduction Factory. American Geophysical Union, Geophysical Monograph* **138**, 223–276.

Klemme, S., Blundy, J. D. & Wood, B. J. (2002). Experimental constraints on major and trace element partitioning during partial melting of eclogite. *Geochimica et Cosmochimica Acta* **66**, 3109–3123.

Klemme, S., Prowatke, S. & Hametner, K. (2005). The partitioning of trace elements between rutile and silicate melts: Implications for subduction zones. *Geochimica et Cosmochimica Acta* **69**, 2361–2371.

Kogiso, T., Hirschmann, M. M. & Frost, D. J. (2003). High-pressure partial melting of garnet pyroxenite: possible mafic lithologies in the source of ocean island basalts. *Earth and Planetary Science Letters* **216**, 603–617.

Kogiso, T., Hirschmann, M. M. & Pertermann, M. (2004). High-pressure partial melting of mafic lithologies in the mantle. *Journal of Petrology* **45**, 2407–2422.

Langmuir, C. H., Klein, E. M. & Plank, T. (1992). Petrological systematics of mid-ocean ridge basalts: Constraints on melt generation beneath ocean ridges. In: Morgan, J. P., Blackman, D. K. & Sinton, J. M. (eds) *Mantle Flow and Melt Generation at Mid-ocean Ridges. American Geophysical Union, Geophysical Monograph* **71**, 183–280.

LaTourrette, T., Hervig, R. L. & Holloway, J. R. (1995). Trace element partitioning between amphibole, phlogopite, and basanite melt. *Earth and Planetary Science Letters* **135**, 13–30.

Lebedev, S. & Nolet, G. (2003). Upper mantle beneath Southeast Asia from S velocity tomography. *Journal of Geophysical Research* **108(B1)**, 2048, doi:10.1029/2000JB000073.

Lee, C. T., Luffi, P., Plank, T., Dalton, H. & Leeman, W. P. (2009). Constraints on the depths and temperatures of basaltic magma generation on Earth and other terrestrial planets using new thermobarometers for mafic magmas. *Earth and Planetary Science Letters* **279**, 20–33.

Leeman, W. P., Lewis, J. F., Evarts, R. C., Conrey, R. M. & Streck, M. J. (2005). Petrologic constraints on the thermal structure of the Cascades arc. *Journal of Volcanology and Geothermal Research* **140**, 67–105.

Lei, J. & Zhao, D. (2006). Global P-wave tomography: On the effect of various mantle and core phases. *Physics of the Earth and Planetary Interiors* **154**, 44–69.

Lei, J., Zhao, D., Steinberger, B., Wu, B., Shen, F. & Li, Z. (2009). New seismic constraints on the upper mantle structure of the Hainan plume. *Physics of the Earth and Planetary Interiors* **173**, 33–50.

Le Roux, V., Lee, C. T. A. & Turner, S. J. (2010). Zn/Fe systematics in mafic and ultramafic systems: Implications for detecting major element heterogeneities in the Earth's mantle. *Geochimica et Cosmochimica Acta* **74**, 2779–2796.

Li, X. H., Liu, Y., Tu, X. L., Hu, G. Q. & Zeng, W. (2002). Precise determination of chemical compositions in silicate rocks using ICP-AES and ICP-MS: a comparative study of sample digestion techniques of alkali fusion and acid dissolution. *Geochimica* **31**, 289–294 (in Chinese with English abstract).

Li, X. H., Qi, C. S., Liu, Y., Liang, X. R., Tu, X. L., Xie, L. W. & Yang, Y. H. (2005). Petrogenesis of the Neoproterozoic bimodal volcanic rocks along the western margin of the Yangtze Block: new constraints from Hf isotopes and Fe/Mn ratios. *Chinese Science Bulletin* **50**, 2481–2486.

Lindsley, D. H. (1983). Pyroxene thermometry. *American Mineralogist* **68**, 477–493.

Liu, Y., Liu, H. C. & Li, X. H. (1996). Simultaneous and precise determination of 40 trace elements in rock samples using ICP-MS. *Geochimica* **25**, 552–558 (in Chinese with English abstract).

Liu, Y., Gao, S., Kelemen, P. B. & Xu, W. (2008). Recycled crust controls contrasting source compositions of Mesozoic and Cenozoic basalts in the North China Craton. *Geochimica et Cosmochimica Acta* **72**, 2349–2376.

Long, W. G., Lin, Y. H., Shi, C., Zhou, J. B. & Lu, C. Y. (2006*a*). Revision of the Pleistocene Daotang Formation in north Hainan Island, China. *Geological Bulletin of China* **25**, 469–474 (in Chinese with English abstract).

Long, W. G., Lin, Y. H., Zhu, Y. H., Shi, C., Zhou, J. B. & Lu, C. Y. (2006*b*). Establishment of the early–mid-Pleistocene Duowen Formation on north Hainan Island, China. *Geological Bulletin of China* **25**, 408–414 (in Chinese with English abstract).

McDade, P., Blundy, J. D. & Wood, B. J. (2003). Trace element partitioning on the Tinaquillo Lherzolite solidus at 1·5 GPa. *Physics of the Earth and Planetary Interiors* **139**, 129–147.

McDonough, W. F. & Sun, S. s. (1995). The composition of the Earth. *Chemical Geology* **120**, 223–253.

McKenzie, D. (1984). The generation and compaction of partial molten rock. *Journal of Petrology* **25**, 713–765.

McKenzie, D. & Bickle, M. J. (1988). The volume and composition of melt generated by extension of the lithosphere. *Journal of Petrology* **29**, 625–679.

McKenzie, D. & O'Nions, R. K. (1991). Partial melt distributions from inversion of rare earth element concentrations. *Journal of Petrology* **32**, 1021–1091.

Middlemost, E. A. K. (1994). Naming materials in the magma/igneous rock system. *Earth-Science Reviews* **37**, 215–224.

Montelli, R., Nolet, G., Dahlen, F. A., Masters, G., Engdahl, E. R. & Hung, S. H. (2004). Finite-frequency tomography reveals a variety of plumes in the mantle. *Science* **303**, 338–343.

Montelli, R., Nolet, G., Dahlen, F. A. & Masters, G. (2006). A catalogue of deep mantle plumes: New results from finite-frequency tomography. *Geochemistry, Geophysics, Geosystems* **7**, Q11007, doi:10.1029/2006GC001248.

Morimoto, N. (1988). Nomenclature of pyroxenes. *Mineralogy and Petrology* **39**, 55–76.

Pertermann, M., Hirschmann, M. M., Hametner, K., Günther, D. & Schmidt, M. W. (2004). Experimental determination of trace element partitioning between garnet and silica-rich liquid during anhydrous partial melting of MORB-like eclogite. *Geochemistry, Geophysics, Geosystems* **5**, Q05A01.

Pfänder, J. A., Munker, C., Stracke, A. & Mezger, K. (2007). Nb/Ta and Zr/Hf in ocean island basalts—Implications for crust–mantle

differentiation and the fate of niobium. *Earth and Planetary Science Letters* **254**, 158–172.

Putirka, K. (1999). Clinopyroxene + liquid equilibria to 100 kbar and 2450 K. *Contributions to Mineralogy and Petrology* **135**, 151–163.

Putirka, K., Johnson, M., Kinzler, R., Longhi, J. & Walker, D. (1996). Thermobarometry of mafic igneous rocks based on clinopyroxene–liquid equilibria, 0–30 kbar. *Contributions to Mineralogy and Petrology* **123**, 92–108.

Putirka, K. D. (2005). Mantle potential temperatures at Hawaii, Iceland, and the mid-ocean ridge system, as inferred from olivine phenocrysts: evidence for thermally driven mantle plume. *Geochemistry, Geophysics, Geosyststems* **6**, Q05L08, doi:10.1029/2005GC000915.

Putirka, K. D. (2008). Thermometers and barometers for volcanic systems. In: Putirka, K. D. & Tepley, F. J., III (eds) *Minerals, Inclusions and Volcanic Processes. Mineralogical Society of America and Geochemical Society, Reviews in Mineralogy and Geochemistry* **69**, 61–120.

Putirka, K. D., Mikaelian, H., Ryerson, F. & Shaw, H. (2003). New clinopyroxene–liquid thermobarometers for mafic, evolved, and volatile-bearing lava compositions, with applications to lavas from Tibet and the Snake River Plain, Idaho. *American Mineralogist* **88**, 1542–1554.

Putirka, K. D., Perfit, M., Ryerson, F. J. & Jackson, M. G. (2007). Ambient and excess mantle temperatures, olivine thermometry, and active vs passive upwelling. *Chemical Geology* **241**, 177–206.

Ren, Z. Y., Takahashi, E., Orihashi, Y. & Johnson, K. T. M. (2004). Petrogenesis of tholeiitic lavas from the submarine Hana Ridge, Haleakala Volcano, Hawaii. *Journal of Petrology* **45**, 2067–2099.

Ritsema, J., Heijst, H. J. V. & Woodhouse, J. H. (1999). Complex shear wave velocity structure imaged beneath Africa and Iceland. *Science* **286**, 1925–1928.

Roeder, P. L. & Emslie, R. F. (1970). Olivine–liquid equilibrium. *Contributions to Mineralogy and Petrology* **29**, 275–289.

Salters, V. J. M. & Longhi, J. (1999). Trace element partitioning during the inital stages of melting beneath mid-ocean ridges. *Earth and Planetary Science Letters* **166**, 15–30.

Salters, V. J. M., Longhi, J. E. & Bizimis, M. (2002). Near mantle solidus trace element partitioning at pressures up to 3·4 GPa. *Geochemistry, Geophysics, Geosystems* **3**, doi:10.1029/2001GC000148.

Sato, H. (1977). Nickel content of basaltic magmas: identification of primary magmas and a measure of the degree of olivine fraction. *Lithos* **10**, 113–120.

Schmerr, N., Garnero, E. & McNamara, A. (2010). Deep mantle plumes and convective upwelling beneath the Pacific Ocean. *Earth and Planetary Science Letters* **294**, 143–151.

Schmidt, M. W., Dardon, A., Chazot, G. & Vannucci, R. (2004). The dependence of Nb and Ta rutile–melt partitioning on melt composition and Nb/Ta fractionation during subduction processes. *Earth and Planetary Science Letters* **226**, 415–432.

Sobolev, A., Hoffman, A. W., Sobolev, S. A. & Nikogosian, I. K. (2005). An olivine-free mantle source of Hawaiian shield basalts. *Nature* **434**, 590–597.

Sobolev, A. V., Hofmann, A. W. & Nikogosian, I. K. (2000). Recycled oceanic crust observed in 'ghost plagioclase' within the source of Mauna Loa lavas. *Nature* **404**, 986–990.

Soesoo, A. (1997). A multivariate statistical analysis of clinopyroxene composition: Empirical coordinates for the crystallisation PT-estimations. *GFF* **119**, 55–60.

Stalder, R., Foley, S. F., Brey, G. P. & Horn, I. (1998). Mineral aqueous fluid partitioning of trace elements at 900–1200°C and 3·0–5·7 GPa: New experimental data for garnet, clinopyroxene, and rutile, and implications for mantle metasomatism. *Geochimica et Cosmochimica Acta* **62**, 1781–1801.

Stone, S. & Niu, Y. (2009). Origin of compositional trends in clinopyroxene of oceanic gabbros and gabbroic rocks: A case study using data from ODP Hole 735B. *Journal of Volcanology and Geothermal Research* **184**, 313–322.

Stracke, A., Bizimis, M. & Salters, V. J. M. (2003). Recycling oceanic crust: Quantitative constraints. *Geochemistry, Geophysics, Geosyststems* **4**, 8003, doi:10.1029/2001GC000223.

Stroncik, N. A. & Devey, C. W. (2011). Recycled gabbro signature in hotspot magmas unveiled by plume–ridge interactions. *Nature Geoscience* **4**, 393–397.

Sun, S. S. & McDonough, W. F. (1989). Chemical and isotopic systematics of oceanic basalts: implications for mantle composition and processes. In: Saunders, A. D. & Norry, M. J. (eds) *Magmatism in the Ocean Basins. Geological Society, London, Special Publications* **42**, 313–345.

Sun, Z., Zhong, Z., Keep, M., Zhou, D., Cai, D., Li, X., Wu, S. & Jiang, J. (2009). 3D analogue modeling of the South China Sea: A discussion on breakup pattern. *Journal of Asian Earth Sciences* **34**, 544–556.

Tamura, Y., Yuhara, M. & Ishii, T. (2000). Primary arc basalts from Daisen Volcano, Japan: equilibrium crystal fractionation versus disequilibrium fractionation during supercooling. *Journal of Petrology* **41**, 431–448.

Taylor, B. & Hayes, D. E. (1980). The tectonic evolution of the South China Sea basin. In: Hayes, D. E. (ed.) *The Tectonic and Geologic Evolution of Southeast Asian Seas and Islands, Geophysical Monograph, American Geophysical Union*, **27**, 23–65.

Thompson, R. N. (1983). Thermal aspects of the origin of Hebridean acid magmas. II. Experimental melting behaviour of granites at 1 kbar pH_2O. *Mineralogical Magazine* **47**, 111–121.

Thompson, R. N. & Gibson, S. A. (2000). Transient high temperatures in mantle plume heads inferred from magnesian olivines in Phanerozoic picrites. *Nature* **28**, 502–506.

Thompson, R. N., Gibson, S. A., Dickin, A. P. & Smith, P. M. (2001). Early Cretaceous basalt and picrite dykes of the southern Etendeka region, NW Namibia: windows into the role of the Tristan mantle plume in Parana–Etendeka magmatism. *Journal of Petrology* **42**, 2049–2081.

Thorne, M. S., Garnero, E. J. & Grand, S. P. (2004). Geographic correlation between hot spots and deep mantle lateral shear-wave velocity gradients. *Physics of the Earth and Planetary Interiors* **146**, 47–63.

Tiepolo, M., Oberti, R., Zanetti, A., Vannucci, R. & Foley, S. F. (2007). Trace-element partitioning between amphibole and silicate melt. In: Hawthorne, F. C., Oberti, R., Della Ventura, G. & Mottana, A. (eds) *Amphiboles: Crystal Chemistry, Occurrence, and Health Issues. Mineralogical Society of America and Geochemical Society. Reviews in Mineralogy and Geochemistry* **67**, 417–452.

Toplis, M. J. & Carroll, M. R. (1995). An experimental study of the influence of oxygen fugacity on Fe–Ti oxide stability, phase relations, and mineral–melt equilibria in ferro-basaltic systems. *Journal of Petrology* **36**, 1137–1170.

Tu, K., Flower, M. F. J., Carlson, R. W., Zhang, M. & Xie, G. (1991). Sr, Nd, and Pb isotopic compositions of Hainan basalts (South China); implications for a subcontinental lithosphere Dupal source. *Geology* **19**, 567–569.

Ulmer, P. (1989). The dependence of Fe^{2+}–Mg cation-partitioning between olivine and basaltic liquid on pressure, temperature and composition. *Contributions to Mineralogy and Petrology* **101**, 261–273.

van Westrenen, W., Blundy, J. D. & Wood, B. J. (2000). Effect of Fe^{2+} on garnet–melt trace element partitioning: experiments in FCMAS and quantification of crystal-chemical controls in natural systems. *Lithos* **53**, 189–201.

van Westrenen, W., Blundy, J., Wood, B. & Mungall, J. E. (1999). Crystal-chemical controls on trace element partitioning between garnet and anhydrous silicate melt. Kinetic controls on the partitioning of trace elements between silicate and sulfide liquids. *American Mineralogist* **84**, 838–847.

Villiger, S., Muntener, O. & Ulmer, P. (2007). Crystallization pressures of mid-ocean ridge basalts derived from major element variations of glasses from equilibrium and fractional crystallization experiments. *Journal of Geophysical Reseach* **112**, B01202, doi:10.1029/2006JB004342.

Wallace, P. J. & Anderson, A. T., Jr (1998). Effects of eruption and lava drainback on the H_2O contents of basaltic magmas at Kilauea Volcano. *Bulletin of Volcanology* **59**, 327–344.

Wang, F., Zhou, X. H., Zhang, L. C., Ying, J. F., Zhang, Y. T., Wu, F. Y. & Zhu, R. X. (2006). Late Mesozoic volcanism in the Great Xing'an Range (NE China): Timing and implications for the dynamic setting of NE Asia. *Earth and Planetary Science Letters* **251**, 179–198.

Wang, X. C., Li, X.-H., Li, W. X. & Li, Z. X. (2007). *Ca.* 825 Ma komatiitic basalts in South China: First evidence for >1500°C mantle melts by a Rodinian mantle plume. *Geology* **35**, 1103–1106.

Wang, X. C., Li, X. H., Li, W. X. & Li, Z. X. (2009). Variable involvements of mantle plumes in the genesis of mid-Neoproterozoic basaltic rocks in South China: A review. *Gondwana Research* **15**, 381–395.

Wu, H. H., Tsai, Y. B., Lee, T. Y., Lo, C. H., Hsieh, C. H. & Toan, D. (2004). 3-D shear wave velocity structure of the crust and upper mantle in South China Sea and its surrounding regions by surface wave dispersion analysis. *Marine Geophysical Researches* **25**, 5–27.

Xiong, X. L., Adam, J. & Green, T. H. (2005). Rutile stability and rutile/melt HFSE partitioning during partial melting of hydrous basalt: Implications for TTG genesis. *Chemical Geology* **218**, 339–359.

Yan, Q., Shi, X., Wang, K., Bu, W. & Xiao, L. (2008). Major element, trace element, and Sr, Nd and Pb isotope studies of Cenozoic basalts from the South China Sea. *Science in China, Series D: Earth Sciences* **51**, 550–566.

Yang, H. J., Frey, F. A. & Clague, D. A. (2003). Constraints on the source components of lavas forming the Hawaiian North Arch and Honolulu Volcanics. *Journal of Petrology* **44**, 603–627.

Yaxley, G. & Sobolev, A. (2007). High-pressure partial melting of gabbro and its role in the Hawaiian magma source. *Contributions to Mineralogy and Petrology* **154**, 371–383.

Yin, A. & Harrison, T. (2000). Geological evolution of the Himalayan–Tibetan orogen. *Annual Review of Earth and Planetary Sciences* **28**, 211–280.

Zhao, D. (2004). Global tomographic images of mantle plumes and subducting slabs: insight into deep Earth dynamics. *Physics of the Earth and Planetary Interiors* **146**, 3–34.

Zhao, D. (2007). Seismic images under 60 hotspots: Search for mantle plumes. *Gondwana Research* **12**, 335–355.

Zhao, D., Yu, S. & Ohtani, E. (2011). East Asia: Seismotectonics, magmatism and mantle dynamics. *Journal of Asian Earth Sciences* **40**, 689–709.

Zhou, P. & Mukasa, S. B. (1997). Nd–Sr–Pb isotopic, and major- and trace-element geochemistry of Cenozoic lavas from the Khorat Plateau, Thailand: sources and petrogenesis. *Chemical Geology* **137**, 175–193.

Zhu, B. Q. & Wang, H. F. (1989). Nd–Sr–Pb isotopic and chemical evidence for the volcanism within MORB–OIB source characteristics in the Leiqiong area, China. *Ceochimica* **3**, 193–201 (in Chinese with English abstract).

Zou, H. & Fan, Q. (2010). U–Th isotopes in Hainan basalts: Implications for sub-asthenospheric origin of EM2 mantle endmember and the dynamics of melting beneath Hainan Island. *Lithos* **116**, 145–152.